Design of a High-Speed Motor-Alternator for Flywheel Energy Storage Systems

by

Marc J. Carlin

S.B., Electrical Science and Engineering,
Massachusetts Institute of Technology (1996)

Submitted to the Department of
Electrical Engineering and Computer Science
in partial fulfillment of the requirements for the degree of

Master of Engineering
in Electrical Engineering and Computer Science

at the

MASSACHUSETTS INSTITUTE OF TECHNOLOGY

June 1997

Author .....
Department of Electrical Engineering and Computer Science
2 June 1997

Certified by .....
James L. Kirtley
Professor of Electrical Engineering and Computer Science
Thesis Supervisor

Certified by .....
Jeffrey H. Lang
Professor of Electrical Engineering and Computer Science
Thesis Supervisor

Accepted by .....
Arthur C. Smith
Chairman, Department Committee on Graduate Theses

Design of a High-Speed Motor-Alternator for Flywheel Energy Storage Systems

by

Marc J. Carlin

Submitted to the Department of

Electrical Engineering and Computer Science

2 June 1997

in partial fulfillment of the requirements for the degree of

Master of Engineering in Electrical Engineering and Computer Science

Abstract

High-speed motor-alternators are required in flywheel energy storage systems for hybrid electric vehicles (HEVs). Recent advances in permanent magnet materials and power electronics have stimulated research into the development of permanent-magnet synchronous machines (PMSMs) for this application. Flywheel systems have the potential to replace chemical batteries as HEV energy storage elements, but there are numerous design requirements that must be met before such systems become viable. The primary electromagnetic design challenge and the key contribution of this thesis is the analysis and characterization of eddy current losses in the permanent magnets arrayed around the rotor of the motor-alternator. Models of the relevant electromagnetic and electromechanical attributes of this type of machine, including power rating and electrical losses, are developed. The Ansoft *Maxwell* finite element software package is used to verify the torque and rotor loss models of the PMSM. A Monte-Carlo based integrated design process is then used to select the frontier of machine designs best suited for this application. The design frontier provides intuition into the design trends and tradeoffs inherent in this system, and investigates the viability of developing high-performance PMSMs with acceptably low rotor eddy current losses.

Thesis Supervisors: James L. Kirtley and Jeffrey H. Lang
Title: Professors of Electrical Engineering and Computer Science

Acknowledgments

Funding for this research was provided through a Small Business Technology Transfer Research Grant from the U.S. Department of Energy, with SatCon Technology Corporation as the prime contractor.

I wish to thank my advisors, James Kirtley and Jeffrey Lang, for their invaluable insight into electromagnetics and their patience in helping me toward completion of this thesis. Their offices were always open when I needed a helping hand. I also wish to thank Dr. Mary Tolikas of SatCon Corporation, who provided not only key data and insights, but also good humor and cheer. I will take with me fonder memories of M.I.T. because of them.

I cannot thank my family enough for the love and support they have shown me during my five-year journey. They were always there to listen and encourage me when I faced challenges and setbacks, and to share in the joy of my successes. My brother Erik has remained my best friend through it all, and to him I am eternally grateful.

My roommate Jeff Roth is indeed a diamond in the rough. Without his companionship, advice, listening ear and gentle spirit I don't know how I could have persevered. "How good and pleasant it is when brothers live together in unity."

Above all I thank the Lord my God, for it is by His grace that I have been saved and am sustained daily. All that I have is a gift from Him, and all that I am is the work of His hands. He has been faithful to His promise

> *So do not fear, for I am with you; do not be dismayed, for I am your God. I will strengthen you and help you; I will uphold you with my righteous right hand.*
>
> Isaiah 41:10

Contents

List of Figures

List of Tables

Chapter 1

Introduction

1.1 Overview

High-speed, high-efficiency motor-alternators are required in flywheel energy storage systems for use in hybrid electric vehicles (HEVs). These systems are referred to as "electromechanical batteries" (EMBs) and can provide power at very high efficiencies and with zero emissions [1]. This thesis presents a design of the motor-alternator that performs electromechanical energy conversion in the EMB system. A permanent-magnet synchronous machine (PMSM) is analyzed and an optimal design for this application is selected by using an integrated design approach.

1.2 Research Background

Flywheels, disks spinning about a fixed axis, have been used as energy-storage elements for hundreds of years. They are used in modern devices such as "wind-up" toy cars and rowing ergometers. These two examples illustrate the use of flywheels as power sources and as "load-levellers," or mechanical low-pass filters.

In recent years, these has been increasing interest in using high-speed (up to 100,000 RPM) flywheels as energy storage systems in electric vehicles. These systems can be used either as the primary source of energy in a vehicle, or to supplement a conventional internal combustion engine or chemical battery. In a hybrid system, the flywheel is designed to provide power levels comparable to an internal combustion engine, and is commonly used in parallel with an internal combustion or gas turbine engine. The flywheel is activated in drive situations requiring large power response, such as peak acceleration or regenerative braking. The latter concept could improve the overall

efficiency of a vehicle by transferring energy normally consumed in braking friction back into the flywheel.

Flywheels hold promise in the development of HEVs because they outperform conventional chemical batteries in a number of important areas. A performance comparison was obtained from SatCon Technology Corp. [2] and is presented in Table 1.1. The flywheel system has the potential of eliminating some of the drawbacks of conventual battery arrays, most notably long recharge time, low driving range, frequent maintenance and low acceleration. The drawback of the flywheel system is its higher cost, but the potential for technological development can be expected to significantly reduce the cost over time. An article by Post [1] outlines recent developments in composite flywheel materials that have increased their potential energy density (stored energy per unit mass) and hold the potential for lower cost flywheel systems.

A number of researchers have investigated EMB systems and constructed feasible prototypes. Post [1], Schaible [3], and Lashley [4] have considered some of the material

Attribute	**Chemical Battery**	**Flywheel System**
Operating Life	2-8 yrs.	20+ yrs.
Reliability	low	high
Recharge Time	10-15 hrs,	3 hrs.
Environmental Issues	Pollution from disposal	none
Maintenance Requirement	6 mos.	7 yrs.
Technological development	mature	promising
Cost	\$0.30/W·hr	\$1.00/W·hr
Power Density (W/kg)	150	5000
Energy Density (W·hr/kg)	10-30	>50

Table 1.1: Chemical battery and flywheel energy storage system comparison

and mechanical challenges presented in this system. Among these are the development of very high tensile strength flywheel materials, lamination of the flywheel to prevent centrifugal forces from tearing the rotor apart, bearing control and stability, and containment in the event of machine failure.

Due to the high speed and high efficiency requirements of the EMB system, the flywheel is housed in a vacuum to greatly reduce windage losses. A key design challenge is that the evacuated environment prohibits conductive and particularly convective heat transfer, limiting heat dissipated in the rotor to radiative transfer and severely constraining rotor power losses. The electric machine that couples energy in and out of the flywheel must be carefully chosen and designed to keep these losses at an acceptable level.

This machine functions as a motor when power is transferred into the flywheel and a generator when power is transferred out of it—a composite motor-alternator. A variety of electric machines are candidates for this application, including induction machines, conventional wound-field synchronous machines, and permanent magnet synchronous machines [5]. Induction machines produce torque by inducing eddy currents on the rotor, producing large eddy current losses during energy transfer and eliminating them from consideration. Conventional synchronous machines require current-carrying rotor field windings that also produce large heating losses, even in the steady state, and are also considered too lossy for this application. Permanent-magnet synchronous machines are more expensive due to the cost of high-performance magnets, but do not require currents to flow in the rotor to convert energy, and are selected for this application.

1.3 Permanent-Magnet Synchronous Motor-Alternator

Recent advances in magnet technologies and power electronics have led to the development of permanent-magnet synchronous motors for EMB applications [6]. These

are rotating machines with wound armatures, and rotors with permanent magnets arrayed around the circumference, eliminating the brushes or slip rings found in wound-rotor machines. PMSMs require extensive power electronics, usually consisting of an inverter and a boost or buck converter, to supply appropriate time-varying armature waveforms. The power electronics are supplied by a DC voltage bus, so these machines are often referred to as "brushless DC" machines. Rotor position sensors, utilizing the Hall effect or sensing back emf, allow the power electronics to place the waveforms in space to produce the required power. For high speed PMSMs, the flywheel is housed in an evacuated chamber to reduce windage losses, and is supported by magnetic frictionless bearings to eliminate friction losses and preclude mechanical bearing failure.

As mentioned in the previous section, the machine uses the permanent magnets rather than currents to produce the rotor field, which tends to greatly reduce rotor losses. High-performance permanent magnet materials can effectively eliminate hysteresis losses, and properly designed and laminated stator cores can greatly reduce core losses. The primary source of rotor losses is the heat created by eddy currents that flow in the magnets on the surface of the rotor. Thermal analysis by engineers at SatCon has determined that these losses cannot exceed a few watts. In this thesis, a conservative upper bound of 1 W is used as a design constraint. Maintaining these losses at an acceptable level is a primary engineering challenge in the design of the motor-alternator, and represents a predominate goal and contribution of this thesis to the research effort.

1.4 Thesis Objectives and Scope

This thesis will focus on the electromechanical and electromagnetic subsystems of a PMSM and will develop a design of a 30 kW, 30,000 RPM machine specified for use in an EMB. The models will be verified by comparing finite element analysis software results to

the theoretical models. The predominate goals of the thesis are to determine whether a high-performance PMSM can be developed with sustainably low eddy current losses, and if so to investigate the design trends that arise in the optimal machine.

Because this is a preliminary investigation into the viability of a PMSM, non-electrical subsystems of the EMB are not explicitly developed. Structural issues such as bearing stability and containment are not addressed in this thesis. Heat transfer is not modeled but, as mentioned above, a limit on rotor heating was obtained and integrated into the design. The design of power electronics is also not within the scope of this thesis, but has been investigated by Srinivasan [7]. For purposes of machine design, a perfectly efficient power system supplying polyphase sinusoidally time-varying waveforms will be assumed.

A thorough design would certainly require an integration of the all of these subsystems, but modeling them would substantially increase the complexity of this thesis and will not be attempted. Insofar as the electrical characteristics of the motor-alternator place important constraints on EMB design, this design process will provide insight into the trends in optimal flywheel motor-alternator design.

1.5 Integrated Design Approach

Once an analytical model of a system has been developed, a process for finding the optimal design must be developed. If the model is nonlinear and involves more than a few variables, it will be difficult or impossible to find the optimal design by solving the model analytically [8]. One solution is to break the system up into smaller, less complex subsystems that can be solved independently of one another. The entire system can be then be reassembled and, by some measure, an optimal design will be produced. This is known as a non-integrated approach, and while it may provide some indication of design trends, it ignores interactions between subsystems that may be of critical importance to optimal

performance.

To better optimize system performance, an integrated design process is employed. In this approach, all system interactions are integrated into a single model and all parameters are optimized concurrently. If the process is properly constructed and executed, it will produce better overall designs than a non-integrated approach. However, improved optimization comes at the expense of an increase in model and design process complexity. Therefore, careful consideration must be given to the depth of analysis to assure the proper balance between model accuracy and mathematical complexity. Because analytical optimization is precluded, finding the optimal designs in an integrated design approach requires searching the design space and using some measure of performance to pick out superior designs. This search can be random or systematic, and may include iterative measures to accelerate design convergence.

This thesis utilizes a design process called the Novice Design Assistant [9, 10, 11, 12], which uses a Monte-Carlo synthesis approach to randomly create designs within specified constraints, and does not use iterative methods to accelerate the design. The results of the design demonstrate that rotor losses for high-performance motor-alternator can indeed be contained to about 100 mW, well below the heat transfer constraint of 1 W.

1.6 Thesis Outline

The design of the motor-alternator proceeds in three stages. First, analytical models of motor-alternator performance, including torque rating, electrical losses, weight, cost, and machine length are developed in Chapter 2. Computational finite element methods are used to verify the analytical models in Chapter 3. A "Monte-Carlo" based integrated design approach is presented in Chapter 4 and a frontier of superior designs is created. Chapter 5 summarizes and concludes the thesis, and offers suggestions for future research.

Chapter 2

Development of Analytical Models

2.1 Introduction

This chapter describes the modeling of the various subsystems of the permanent-magnet synchronous motor-alternator. First, design requirements and objectives are outlined, and then an appropriate machine configuration is chosen and analytical models of its performance are developed. In all aspects of design formulation, careful consideration is given to the appropriate balance between accuracy of performance evaluation and simplicity of analytical models.

The analysis of a permanent-magnet synchronous machine very closely follows that of a conventional synchronous machine with a wound field on the rotor. Classical methods for analyzing the steady-state behavior of synchronous electric machines have been thoroughly developed and are well understood [5]. Expressions for machine rating and armature losses are first derived using these common models. Rotor eddy current losses are negligible in the analysis of wound field machines, because Ohmic losses in the field windings are typically much larger. In PMSMs, however, they are the critical constraint on machine losses and the development of accurate eddy current models is vital. A model that builds upon current research and introduces three-dimensional analysis is developed and represents the key contribution of this thesis. Finally, models of weight, cost, and machine length are developed to complete the analysis of motor performance.

2.2 Design Specification and Objectives

The objective of this design process is to find the machine (or set of machines) that meets performance specifications while demonstrating superior attributes. The design

specifications for the permanent-magnet synchronous machine are given below.

• **Power (P_{mech})** The motor must deliver a fixed amount of mechanical power, reflecting the machine's capacity for energy transfer from the electrical system to the flywheel. In this design the power requirement is 30 kW.

• **Rotor speed (ω_m)** The speed of the flywheel will change as it is discharged and recharged. The model analyzes machine performance as a typical operating point. Note that this specification, in conjunction with the power requirement, determines the amount of torque that the machine must produce. A typical operating point for this design was chosen to be 3142 rad/sec (30,000 RPM).

• **Terminal voltage (V)** The motor-alternator will be powered from the vehicle's DC bus and the RMS value of the line-to-neutral terminal voltage must exceed than this voltage. In this design, the terminal voltage will be fixed at the bus voltage. Choosing a specific voltage may appear to constrain the design, but as the models will demonstrate, this does not place any restrictions on optimal machine selection. The terminal voltage of a motor can be changed to any arbitrary value without changing the relevant design attributes. A terminal voltage of 155 V was used in this thesis.

The objective of the design is to find a machine that meets these performance requirements, and also exhibits the most desirable performance in the following attributes.

• **Rotor eddy current loss (P_r)** Eddy current will flow in the permanent magnets because of armature space harmonics, causing power loss. This dissipation must be contained or heat buildup will cause the flywheel system to fail.

• **Material cost (C_t)** This includes the cost of the copper and magnets in the machine. Other machine costs such as manufacturing will add to the total machine cost,

but they are not likely to depend significantly on design parameters and are neglected.

• **Material weight (w_t)**

• **Electrical efficiency (*Eff*)** The predominate electrical losses in the machine are Ohmic and eddy current losses in the armature wires. Rotor losses, though an important attribute, are negligible in the efficiency calculation.

• **Total machine length (l_o)** This dimension includes the length of the armature as well as the end turn height.

2.3 Scope of Design Consideration

In order to avoid an unnecessarily complex and time-consuming design process, several reasonable restrictions were placed on the scope of this design framework.

2.3.1 Selection of Machine Configuration

There are several feasible geometric configurations for a PMSM. Analytical comparison of these configurations would require the integration of the various machine models into a larger design process. This would increase the degrees of freedom in design and would be time-consuming. Consequently, engineering intuition led to the *a priori* selection of a machine configuration judged to be best suited for high-speed, low rotor loss performance: a three-phase, "inside-out," ironless machine with air-gap windings and surface mounted Neodynium Iron Boron magnets in a Halbach array configuration. This machine configuration is illustrated in Fig. 2.1.

• **Three-phase power** The drive for this machine was chosen to provide three-phase balanced armature currents. Such systems are almost universally applied in commercial synchronous machines because they produce output torque that is nearly constant in time. In contrast, single-phase systems produce torques varying sinusoidally in time that can

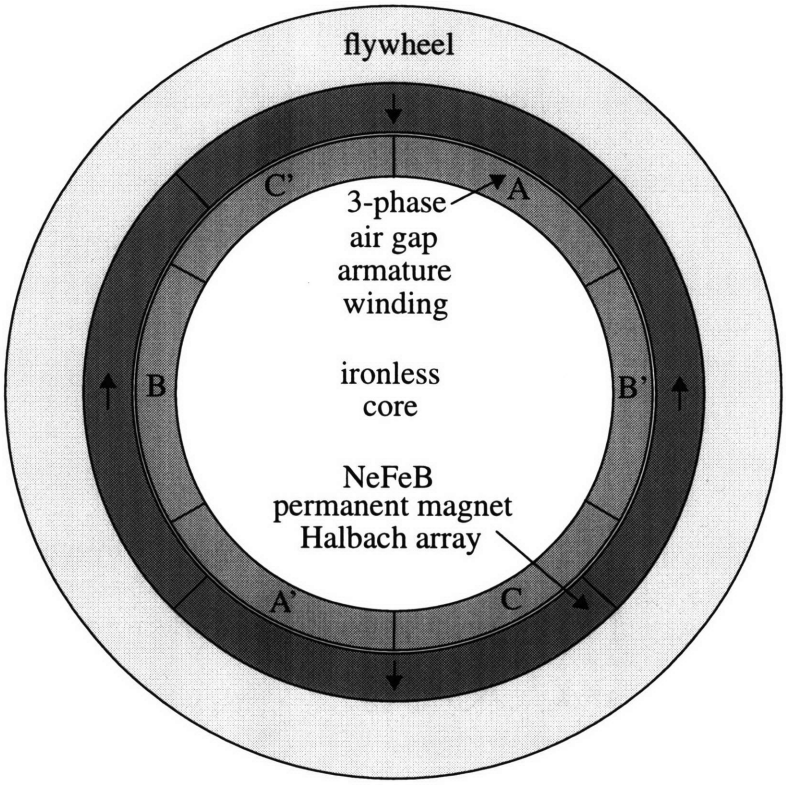

Figure 2.1: Selected machine configuration

produce destructive mechanical vibrations. In addition, polyphase systems produce armature fields that are more sinusoidal in space and which will tend to reduce space harmonics and associated rotor losses. In this design framework, reducing rotor losses will tend to indicate using the maximum number of phases possible to reduce space harmonics. In a broader design framework, the number of phases will be limited by the cost of the associated power electronics. The power electronics model is outside the scope of this thesis, however, so standard three-phase power was chosen to provide a framework for machine design.

- **NeFeB magnets** Because of the large power requirement of the motor-alternator,

high performance magnets with strong magnetization are required. The strongest magnet material on the market is Samarium Cobalt (SmCo), but because cobalt is a rare earth element mined in politically sensitive countries, SmCo will not be considered in this application. Neodynium Iron Boron (NeFeB) magnets [13] were selected because they have a relatively strong residual flux density and are magnetically hard. However, a drawback to the high-performance magnets is that they have relatively high conductivity, which will contribute to rotor eddy current losses. One option is to use plastic bonded NeFeB magnets, in which the magnetic material is suspended in a plastic matrix rather than sintered, with no increase in cost. This reduces conductivity by more than an order of magnitude, but the residual flux density is reduced by half. Because rotor losses are a key design constraint, the NeFeB magnets will be considered with both bonded and sintered fabrication. Table 2.1 summarizes the relevant characteristics of each material.

Fabrication Class	Residual Flux Density (T)	Conductivity (S/m)	Relative Permeability	Density	Cost
Sintered	1.2	7.0×10^5	1.05	7500 kg/m^3	\$72/kg
Bonded	0.6	2.5×10^4	1.05	5950 kg/m^3	\$72/kg

Table 2.1: Characteristics of Neodynium Iron Boron permanent magnets

• **Surface-mounted magnets** The permanent magnets must be arrayed in such a way as to produce roughly sinusoidally varying flux that crosses the air gap. Typically, they are placed in a ring around the outside of the rotor. However, in high-speed applications, centrifugal forces act to pull the magnets away from the rotor, possibly resulting in catastrophic machine failure. One way of addressing this is to "bury" the magnets in the interior of the rotor to provide structural support. However, this configuration is very difficult to manufacture and is avoided. The surface-mounted magnet array was chosen

and the problem of structural support was addressed by the choice of stator/rotor geometry described next.

• **Inside-out stator/rotor** Synchronous machines are commonly constructed with the rotor in the interior of the stator, as illustrated in Fig. 2.2(a). The reversed or "inside-out" configuration shown in Fig. 2.2(b) has essentially identical energy conversion mechanisms, but is typically avoided because of the need to construct a hub connecting the rotor to the shaft. In high-speed PMSM applications, however, placing the magnet array on the inside of the rotor can provide structural support against centrifugal forces and prevent the magnets from tearing off of the rotor. This eliminates the added cost and complexity of installing a retaining ring.

• **Halbach magnet array** Conventionally, surface-mounted magnets are arrayed in a ring with their magnetization alternating between radially inward and radially outward, as

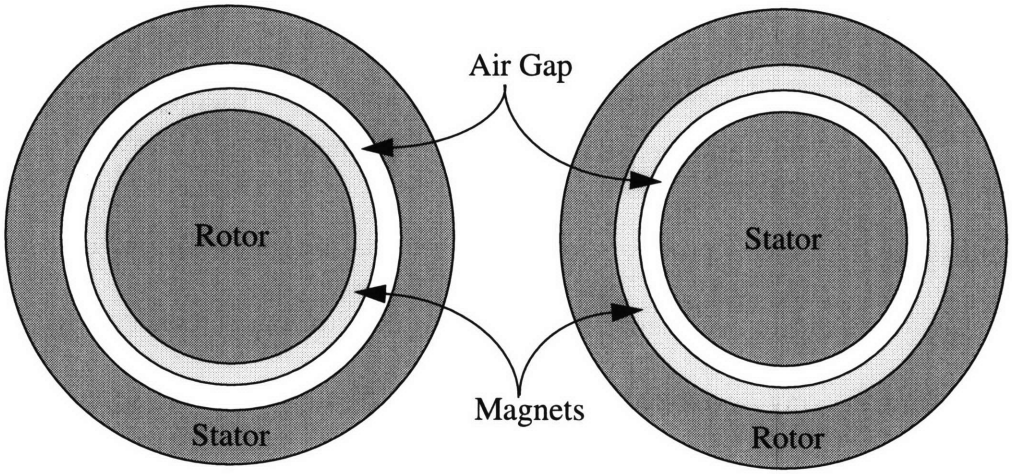

Figure 2.2: Comparison of (a) conventional and (b) "inside-out" stator/rotor configurations

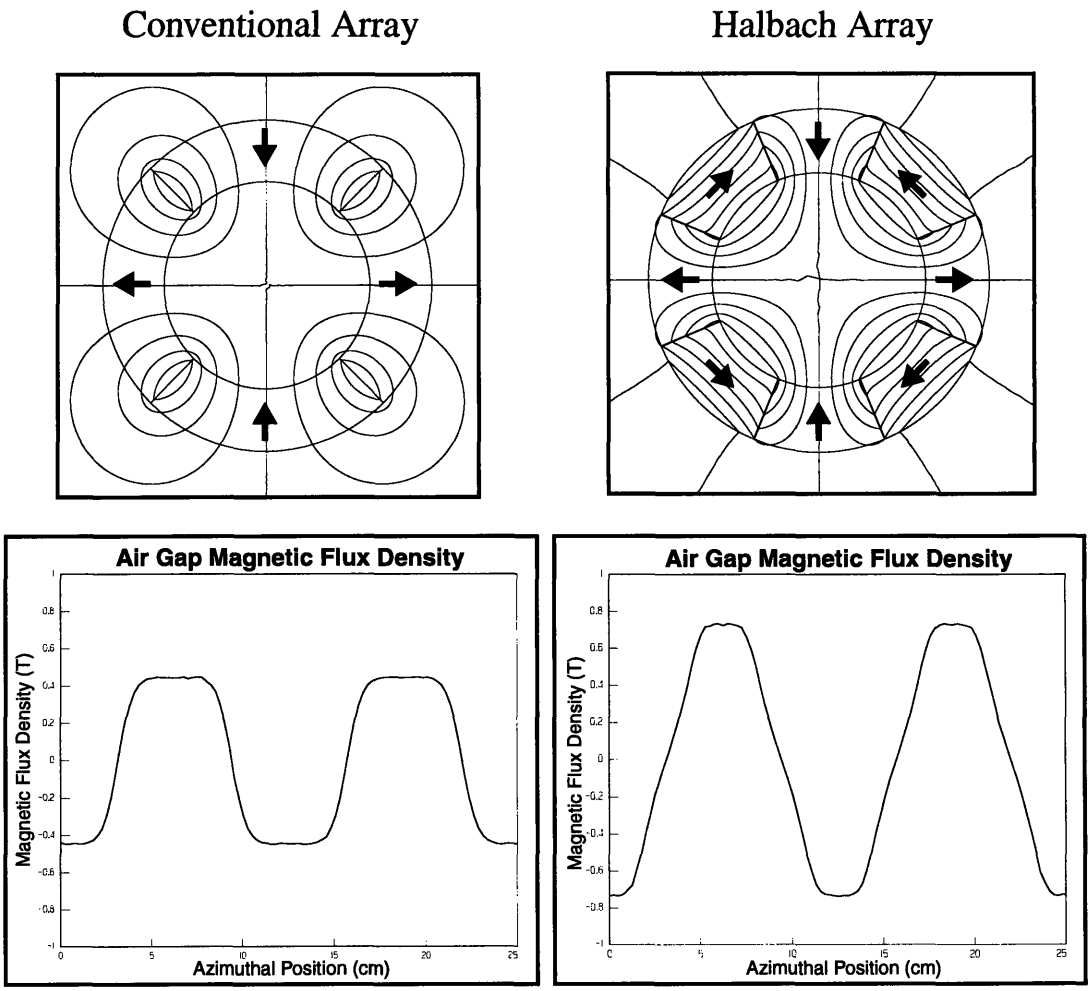

Figure 2.3: Finite element analysis of magnetic field and radial air gap flux for (a) conventional and (b) Halbach permanent magnet arrays

shown in Fig. 2.3(a). This produces magnetic flux that is equally distributed between the interior and the exterior of the ring. Alternatively, the flux can be concentrated inside the ring by using an array developed by Halbach [14, 15] and illustrated in Fig. 2.3(b). The field produced by the azimuthal magnets tends to cancel the field produced by the radial magnets outside of the array, but reinforces it inside the array. This places nearly all of the magnetic flux in the interior of the magnets and produces a field that is roughly $\sqrt{2}$ times as strong at the interior edge of the array. A plot of the radial magnetic flux inside each

magnet array is pictured in Fig. 2.3.

• **Ironless machine** Magnetic steel is commonly placed behind the field and armature windings as "back iron" to serve as a high-permeability channel for magnetic flux, increasing air gap flux and the torque rating of the machine. However, if steel is exposed to time-varying magnetic fields, heat is produced by eddy current and hysteresis losses. In this application, these losses are eliminated by replacing the iron in the stator and rotor with a non-conducting material like plastic. This will reduce air gap flux, but the use of a Halbach array can restore some of it. A further advantage of the ironless configuration is that the machine weight will be significantly reduced, which is beneficial in automotive applications.

• **Air-gap windings** The armature can be wound either with or without slots. The chief advantage of steel slots is that they reduce the effective air gap by providing a high permeability path directly to the physical air gap. However, this PMSM is ironless so a slotless winding was chosen. Air-gap windings tend to be more difficult to construct, but the increase in cost is modest and is accepted in this application. Another important benefit is that air-gap windings have smaller higher-order field harmonics due to the absence of slot harmonics. As outlined in Sec. 2.5.3.2, higher-order harmonics give rise to eddy currents that drive the critical loss mechanism in the rotor.

This choice of machine configuration was based on design intuition rather than mathematical analysis, so a more broad integrated design is necessary to verify the validity of this selection. However, the *a priori* choice reasonably limits the scope of design consideration and model complexity, allowing for a simpler design process but

producing insight into important design issues and trends in optimized machine characteristics.

2.3.2 Depth of Analysis

In order to further simplify the models, several assumptions were adopted. These assumptions must be relaxed before a thorough design process is developed, but they are necessary to create models of necessary simplicity at this stage of machine design.

• **Power electronics** This thesis does not address the design of the power electronics that provide the drive for the motor-alternator. Models of machine drives such as inverters introduce a host of associated constraints, as demonstrated by Srinivasan [7]. It is assumed that the drive functions as an infinite voltage bus, with a power factor of unity and current and voltage waveforms that are perfectly sinusoidal in time.

• **Dynamic analysis** The models developed in this thesis are for steady state synchronous operation only. Dynamic situations like the charging and discharging of the rotor will have significant effects particularly on rotor losses, because the fundamental armature field will vary in time in the stationary frame of the rotor and produce eddy currents.

• **Material properties** In this model all materials have linear and anisotropic conductivity, magnetization, and permeability. A more thorough analysis would consider the effect of temperature on magnet conductivity and magnetization, and explore the possibility of demagnetizing fields under terminal fault conditions. In addition, the nonlinearity of the magnet *B-H* curve will cause hysteresis losses that might become significant for strong, high frequency field excitation. However, high performance NeFeB magnets are very hard magnets, meaning that the demagnitizing force is very large and

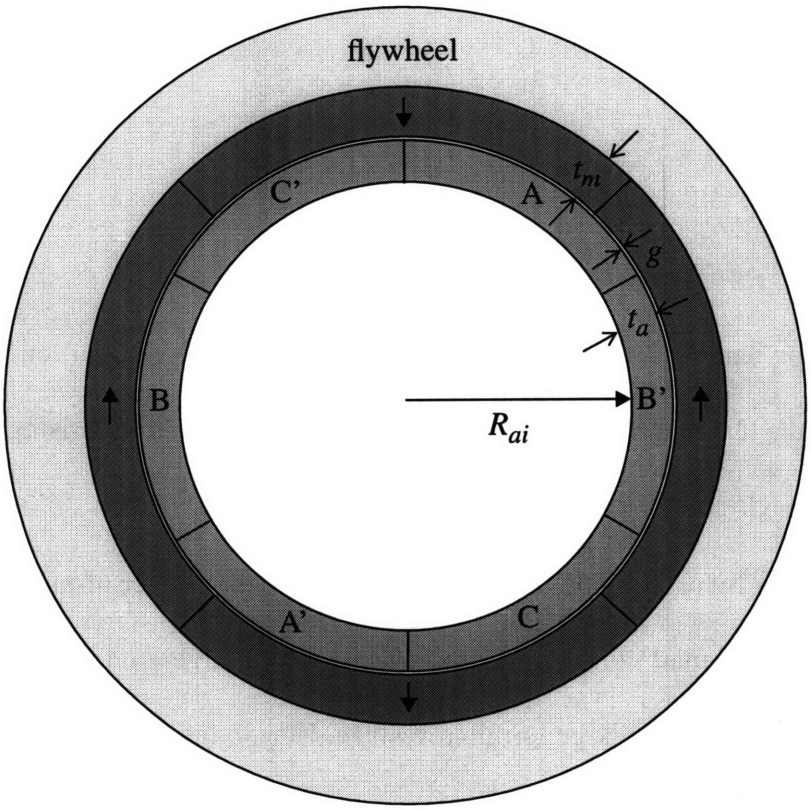

Figure 2.4: Motor geometry for a two-pole machine

that the *B-H* curve is nearly linear in the operating range. To a first approximation, all of these nonlinearities can be ignored, but a more thorough design process should consider them.

These *a priori* parameter selections and assumptions simplify the model to within reasonable scope, yet provide enough accuracy that insight into the feasibility and design trends of a flywheel PMSM is maintained.

2.4 Motor Parameters

A diagram of the selected motor configuration illustrating its physical dimensions is presented in Fig. 2.4. The parameters in the machine are as follows.

• **Machine Dimensions (R_{ai}, t_a, g, and t_m)** These dimensions will establish the machine radii

$$\begin{aligned} R_{ao} &= R_{ai} + t_a \\ R_m &= R_{ao} + g_o \\ R_s &= R_m + t_m \end{aligned} \tag{2.1}$$

• **Machine length (L)** This refers to the length of the axial portion of the armature, i.e., excluding the length of the end turns. Field perturbations arising from end turn currents are negligible in this analysis.

• **Armature turns per phase (N_a)** This is the total number of turns in all poles of a phase winding. A small number of turns will require a large amount of terminal current, while many turns create a large terminal voltage. Hence, the number of turns tends to fall at an intermediate value.

• **Parallel strands per turn (N_{par})** The armature is exposed to a time-changing magnetic field produced by the rotor, causing eddy current losses in the armature wires. To reduce this effect the armature turns are divided into smaller insulated strands, producing lower losses.

• **Terminal current (I)** This is the RMS value of the current into each armature phase.

• **Wire strand diameter (d_w)** As outlined above, smaller strands in the armature turns will reduce eddy current losses.

• **Magnet material properties (B_r, σ_m, μ_m, ρ_m, and C_m)**

The requirements, attributes, constants, and parameters in the PMSM model are summarized in Table 2.2.

2.5 Analytical Machine Models

In the following sections, models of the electrical and electromechanical behavior, loss mechanisms, and geometry of a permanent-magnet synchronous machine will be developed. Models for rating the output torque and terminal electrical behavior of the machine are based on classical synchronous machine theory. Models of armature eddy current and Ohmic losses are also well understood, along with techniques for analyzing end turn geometry. Rotor eddy current models contain some original methods and are developed in more detail.

2.5.1 Machine Terminal Characteristics

The terminal behavior of one phase of a synchronous electric machine can be summarized by the equivalent circuit of Fig. 2.5. V is the line-to-neutral terminal voltage, I is the terminal current, E_{af} is the back emf (the time derivative of flux linked by the armature winding), X_d is the synchronous reactance of the armature winding, and R_a is the resistance of the armature winding. The armature is wound in a wye-connected

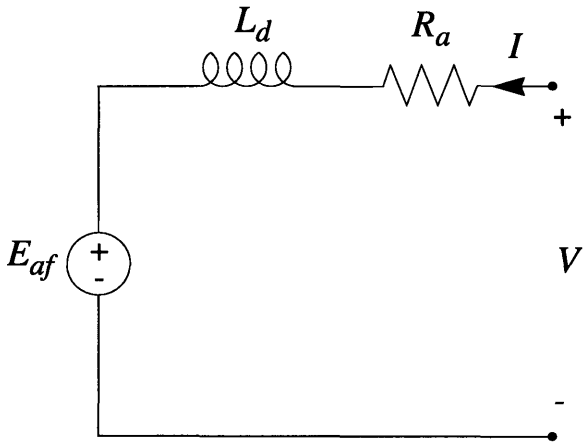

Figure 2.5: Synchronous motor equivalent circuit for one phase

	Symbol	Description	Units
Requirements	P_{mech}	Mechanical power	W
	ω_m	Mechanical rotational speed	rad/sec
	V	Terminal Voltage	V
Parameters	R_{ai}	Armature inner radius	cm
	t_a	Armature thickness	cm
	g	Physical air gap	cm
	t_m	Magnet thickness	cm
	p	Number of pole pairs	unitless
	L	Machine length (excluding end turns)	cm
	N_a	Armature turns per phase	unitless
	N_{par}	Parallel strands per turn	unitless
	I	Armature current per turn	A
	d_w	Wire strand diameter	cm
	B_r	Magnet residual flux density	T
	σ_m	Magnet conductivity	S/m
	μ_r	Magnet relative permeability	unitless
	ρ_m	Magnet density	kg/m^3
	C_m	Magnet cost	US$/kg
Constants	μ_0	Permeability of free space	H/m
	σ_c	Copper conductivity	S/m
	μ_c	Copper permeability	H/m
	ρ_c	Copper density	kg/m^3
	C_c	Copper cost	US$/kg
Attributes	P_r	Rotor eddy current losses	W
	Eff	Electrical Efficiency	%
	C_t	Material cost	US$
	w_t	Material weight	kg
	l_o	Machine length (including end turns)	cm

Table 2.2: Model variables

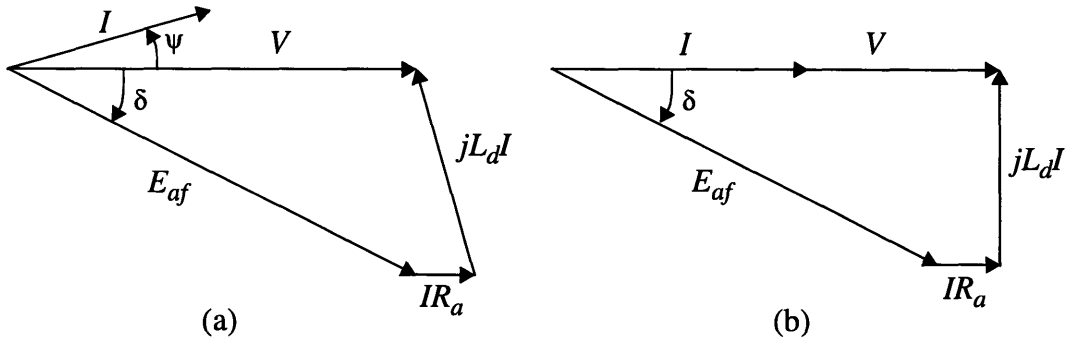

Figure 2.6: Synchronous motor phasor diagrams for (a) arbitrary ψ and (b) ψ = 0

configuration in this machine. Because the machine is operating synchronously, voltage, current, and back emf will have the same frequency ω_e, the *electrical* frequency of excitation. Assigning arbitrary phase differences, these quantities can be expressed as

$$\begin{aligned} V(t) &= \sqrt{2}V\cos(\omega_e t) \\ I(t) &= \sqrt{2}I\cos(\omega_e t - \psi) \\ E_{af}(t) &= \sqrt{2}E_{af}\cos(\omega_e t + \delta) \end{aligned} \tag{2.2}$$

where the magnitudes are RMS values.

In motor operation, current flows into the terminals and the machine can be described by the phasor diagram of Fig. 2.6(a). In this thesis, the motor drive is an infinite bus that supplies current and voltage in phase, so that ψ is 0° and cos ψ, the *power factor*, is unity. Under these operating conditions, the machine can be described by the phasor diagram in Fig. 2.6(b), and the electrical power into the machine is given by

$$P_{elec} = 3VI \tag{2.3}$$

To determine the terminal behavior of the machine, then, the synchronous armature reactance, back emf, and armature resistance must be calculated. The synchronous reactance is

$$X_d = \omega_e L_d \tag{2.4}$$

where the armature self-inductance, derived in Appendix A, is given by

$$L_d = \frac{3}{2}\frac{4}{\pi}\frac{\mu_0 (N_a)^2 (k_w)^2 L}{p} k_s \tag{2.5}$$

The coefficient k_w is a winding factor related to the number of machine phases and k_s is a coefficient incorporating the armature geometry.

Lastly, back emf is given by

$$E_{af} = \omega_e \lambda_a \tag{2.6}$$

The armature flux λ_a, derived in Appendix B, has RMS value

$$\lambda_a = \frac{4}{\pi}\frac{2 B_r N_a R_{ai} L k_w k_m k_t}{p} \tag{2.7}$$

where k_t is a coefficient that includes the effect of the radial thickness of the winding, and k_m is a coefficient that represents the relationship of the radial field produced by the magnets to machine geometry.

Armature resistance is given by

$$R_a = \frac{2N_a(L + l_t)}{\sigma_c A_t} \tag{2.8}$$

where A_t is the cross sectional area of the copper in one armature turn:

$$A_t = N_{par}\pi\left(\frac{d_w}{2}\right)^2 \tag{2.9}$$

The turn length l_t depends on the end turn configuration and is derived in Appendix C.

2.5.2 Electromagnetic Torque Model

PMSMs operate just like conventional synchronous machines, except that the field windings are replaced by permanent magnets. The magnets are mounted on the rotor and the stator has a conventional armature winding. In motor operation, the magnetic fields produced by the magnets interact with the fields produced by current in the armature windings to produce torque on the shaft, and associated mechanical power, which can be expressed as

$$P_{mech} = T\omega_m = T\frac{\omega_e}{p} \tag{2.10}$$

where ω_m is the *mechanical* rotational speed.

Alternatively, torque applied to the shaft will cause an induced voltage in the armature winding, and create electrical power. Hence the PMSM, like any electric machine, can serve as either a motor or a generator. The analysis presented in this section will consider motor operation, though generator operation can be analyzed using identical concepts and models.

• **Torque rating** Instantaneous electromagnetic torque results from $\boldsymbol{J} \times \boldsymbol{B}$ forces and can be derived from conservation of power:

$$P_{elec} = P_{mech} + P_{loss} \tag{2.11}$$

In this model P_{loss} encompasses only Ohmic armature loss, while system losses such as windage loss and rotor eddy current loss are comparatively small and have been neglected.

Using Eqs. 2.3 and 2.10, along with the definition of Ohmic loss gives

$$3VI = T\omega_m + 3I^2R_a \tag{2.12}$$

which can be solved for torque to give

$$T = \frac{3(VI - I^2R_a)}{\omega_m} \tag{2.13}$$

From the phasor diagram in Fig. 2.6(b) it is evident that

$$V - IR_a = E_{af}\cos\delta \tag{2.14}$$

Using this relation along with the definition of back emf

$$E_{af} = \frac{d}{dt}\lambda_a = \omega_e\lambda_a = p\omega_m\lambda_a \tag{2.15}$$

gives

$$T = 3p\lambda_a I\cos\delta \tag{2.16}$$

Because of its relationship to machine torque, δ is called the *torque angle*.

• **Calculation of armature amp-turns** In this design, the torque is specified and the machine must be rated for current and torque angle. A useful intermediate quantity in this calculation is the total cross sectional current flowing in each phase of the armature. This quantity is referred to as the number of amp-turns *NI*, where

$$NI = N_aI \tag{2.17}$$

The amp-turn rating can be determined by starting with the relationship between voltage, current, and back emf indicated by the phasor diagram in Fig. 2.6,

$$(V - R_a I)^2 + (IX_d)^2 = (E_{af})^2 \tag{2.18}$$

From conservation of power it is evident that

$$V - R_a I = \frac{P_{mech}}{3I} \tag{2.19}$$

so that Eq. 2.18 can be rewritten

$$\left(\frac{P_{mech}}{3I}\right)^2 + (IX_d)^2 = (E_{af})^2 \tag{2.20}$$

This equation can be solved for I to yield

$$I = \frac{1}{X_d}\sqrt{\frac{(E_{af})^2 - \sqrt{(E_{af})^4 - \left(\frac{2P_{mech}X_d}{3}\right)^2}}{2}} \tag{2.21}$$

Now consider that E_{af}, given by Eq. 2.6, is proportional to N_a, while X_d, given by Eq. 2.4, is proportional to $(N_a)^2$. This will cause I to be proportional to $1/N_a$, geometric parameters, and the power rating. Hence the product $I{\cdot}N_a$, the number of amp-turns necessary to produce the rated power, can be calculated. This is given by

$$NI = \pi\frac{\sqrt{2(R_{ai}LB_1k_w\omega_m)^2 - 2\sqrt{(R_{ai}LB_1k_w\omega_m)^4 - \left(\frac{P_{mech}\mu_0(k_w)^2k_sL\omega_m}{\pi}\right)^2}}}{6\omega_m\mu_0(k_w)^2k_sL} \tag{2.22}$$

where B_1 is a shorthand quantity that represents the RMS fundamental flux averaged over the winding thickness

$$B_1 = \frac{4}{\pi}B_r k_m k_t \tag{2.23}$$

- **Calculation of terminal current and torque angle** To solve for the number of

armature turns and terminal current, a further constraint must be placed on the system. A straightforward approach is to choose the number of turns and solve for current directly with Eq. 2.17.

The alternative method used in this design is to choose the terminal voltage. Note that *NI* is independent of *V*, so that for a given power rating and machine geometry, production of a desired torque will require a given number of amp-turns *for any terminal voltage*. This is because flux linkage (and hence terminal voltage) is proportional to armature turns according to Eq. 2.7, so that *power* is independent of armature turns. Hence, any number of armature turns can be chosen to produce the required power at a specified voltage, provided that the required number of amp-turns is supplied. To illustrate, a machine with large current and a few armature turns can produce the same torque as a machine with a small current and many armature turns, but at a lower terminal voltage.

To find I and N_a, start with Eq. 2.12, which can be rearranged to find

$$V = \frac{T\omega_m}{3I} + IR_a = \frac{P_{mech}}{3I} + IR_a \tag{2.24}$$

Substituting for R_a and I by using Eqs. 2.8 and 2.17 gives

$$V = \frac{P_{mech}N_a}{3(NI)} + \frac{(NI)}{N_a}\frac{N_a l_t}{N_{par}\pi\left(\frac{d_w}{2}\right)^2} = \frac{P_{mech}N_a}{3(NI)} + \frac{(NI)l_t}{N_{par}\pi\left(\frac{d_w}{2}\right)^2} \tag{2.25}$$

Now, noting that the total number of conductors in each armature belt, N_{ac}, is

$$N_{ac} = N_a N_{par} \tag{2.26}$$

Eq. 2.25 can be rewritten and solved for N_a to give

$$N_a = \frac{V}{\frac{P_{mech}}{3(NI)} + \frac{(NI)l_t}{N_{ac}\pi\left(\frac{d_w}{2}\right)^2}} \tag{2.27}$$

This represents the unique number of armature turns that will both link enough flux to create the appropriate terminal voltage and supply enough amp-turns to produce the rated mechanical power.

The armature current per turn and the torque angle can now be found from, the number of parallel wire strands and the torque angle will then be given exogenously by

$$I = \frac{(NI)}{N_a} \tag{2.28}$$

and

$$\delta = \text{acos}\left(\frac{T}{3p\lambda_a I}\right) \tag{2.29}$$

The number of parallel strands is given exogenously by

$$N_{par} = \frac{N_{ac}}{N_a} \tag{2.30}$$

Hence the current rating and torque angle can be determined, for a given power and terminal voltage, with only N_{ac} as an input to the machine model. The armature current will then give rise to the electrical losses in the machine.

2.5.3 Loss Models

The primary loss mechanisms in the permanent-magnet synchronous machine will be armature and rotor heating. The armature losses arise from Ohmic heating in the current-carrying wires as well as eddy current losses in these wires. There are no rotor source

currents so the rotor losses will be entirely due to eddy current losses. The magnet material of choice, NeFeB, is magnetically hard so hysteresis losses can be neglected. The are no core losses in the machine because of the absence of iron.

The rotor losses will tend to be such smaller than the stator losses, but because the rotor is in an evacuated chamber, heat transfer is limited to radiation and is estimated to be limited to only 1 watt. The armature is not necessarily relegated to the vacuum, and can be outside of it if the evacuated chamber runs through the air gap. Even if the stator is in the vacuum, active armature cooling schemes such as water circulation are available. Consequently, minimizing rotor losses is the critical issue in machine viability and models of these losses are accordingly detailed. Armature losses must still be modeled and contained, however, because they will decrease electrical efficiency, increase terminal voltage, and add to the cost of armature cooling.

2.5.3.1 Armature Loss

Losses in the armature winding will be caused by Ohmic heating arising from both terminal current and induced eddy current in the wires.

• **Terminal current Ohmic loss** Current flowing in the armature winding will give rise to losses

$$P_{ohm} = 3I^2R_a \tag{2.31}$$

I is the current in each phase, and R_a is the resistance of each armature phase, as given by Eq. 2.8. Note that this expression can be rewritten using Eqs. 2.8, 2.9 and 2.17 to give

$$P_{ohm} = 3\left(\frac{NI}{N_a}\right)^2 \frac{(N_a)^2(L+l_t)}{\sigma_c(AC)\pi\left(\frac{d_w}{2}\right)^2} = \frac{3(NI)^2(L+l_t)}{\sigma_c(AC)\pi\left(\frac{d_w}{2}\right)^2} \tag{2.32}$$

This indicates that for a machine with a given torque rating, the Ohmic losses are

independent of the terminal voltage for a given number of armature conductors.

• **Armature eddy current loss** Losses will also occur in the armature because it is immersed in the rotating field produced by the rotor magnets. These time changing fields will produce eddy currents in the armature wires and associated heat loss. A reasonable approximation of these losses is derived in Appendix D as

$$P_{ec} = \frac{6\pi N_{ac} L(\omega_e)^2 (B_1)^2 \sigma_c (d_w)^4}{128} \tag{2.33}$$

B_1 is the space average RMS value of the fundamental radial magnetic flux density in the armature winding,

$$B_1 = \frac{4}{\pi} B_r k_m k_t \tag{2.34}$$

which provides a good measure of the average flux density seen by an armature wire. P_{ec} is also independent of the terminal voltage because it is determined only by the magnet fields and the number of armature conductors.

• **Electrical efficiency** The total loss of electrical origin in the armature is

$$P_a = P_{ohm} + P_{ec} \tag{2.35}$$

The overall electrical efficiency is then given by

$$Eff = 1 - \frac{P_a}{P_e} = 1 - \frac{P_a}{3VI} \tag{2.36}$$

2.5.3.2 Rotor Eddy Current Losses

This section presents a detailed three-dimensional model of the losses in the rotor, which are entirely due to eddy currents induced by the armature magnetic field. The

machine is analyzed in synchronous operation, so that the fundamental component of armature field as seen by the rotor is stationary. Hence, only higher order-harmonics will produce these losses. The loss analysis will proceed in three stages: (1) derivation of the magnitude of the armature space harmonics; (2) derivation of a 2D model of power losses due to these harmonics; and (3) addition of a "correction factor" for losses in machines with short axial length. These will together form a 3D model of losses on the rotor.

• **Armature space harmonics** Several assumptions are made about the currents flowing in the armature winding. First, the current density is constant over space in each phase belt. Second, the currents are three-phase, balanced in time, and have no time harmonics. Lastly, the currents are assumed to flow only in the z-direction for now, but this assumption will be relaxed when the 3D model is developed. The current distribution can then be expressed as

$$J(t,\theta)\hat{z} = J_A(t,\theta)\hat{z} + J_B(t,\theta)\hat{z} + J_C(t,\theta)\hat{z} \tag{2.37}$$

where

$$\begin{aligned} J_A(t,\theta) &= J\cos(np\theta)\cos(\omega_e t) \\ J_B(t,\theta) &= J\cos(np\theta)\cos(\omega_e t - 120°) \\ J_C(t,\theta) &= J\cos(np\theta)\cos(\omega_e t + 120°) \end{aligned} \tag{2.38}$$

These expressions apply to the unprimed phase belts in Fig. 2.4. The primed belts are the return paths of the unprimed belts, so their current densities will have equal magnitude and opposite sign. When combined, the belts will produce an approximation to a travelling sinusoidal wave, as the "snapshots" in Fig. 2.7 illustrate.

The magnitude J of the current density in each phase belt can be found by taking the ratio of the total cross sectional armature current to the armature area:

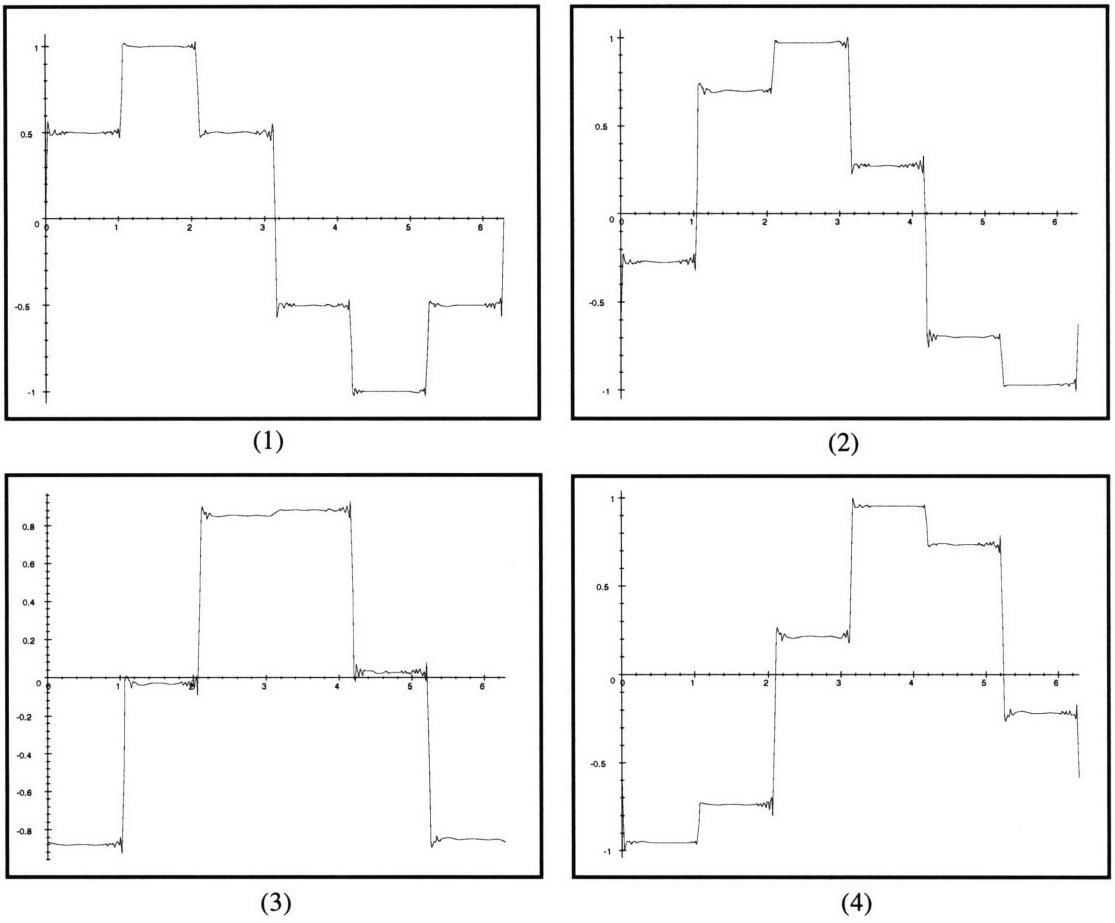

Figure 2.7: "Snapshots" of three-phase air gap armature current

$$J = \frac{2q(NI)}{\pi((R_{ao})^2 - (R_{ai})^2)} \tag{2.39}$$

Note that this voltage is dependent only on the number of amp-turns and not terminal voltage, so as with armature losses in Sec. 2.5.3.1, the terminal voltage does not affect this machine attribute.

This current waveform can be Fourier analyzed to produce a series of positive and negative travelling waves of the form

$$J(t,\theta) = \sum_n J_n^+ \sin(np\theta - \omega_e t) + \sum_n J_n^- \sin(np\theta + \omega_e t) \tag{2.40}$$

where

$$\left.\begin{aligned} J_n^+ &= J\frac{q}{2}\frac{4}{n\pi}\cos\left(\frac{q-1}{q}\frac{\pi n}{2}\right) \\ J_n^- &= J\frac{q}{2}\frac{4}{n\pi}\cos\left(\frac{q-1}{q}\frac{\pi n}{2}\right) \end{aligned}\right\} \equiv J_n \qquad \begin{aligned} n &= 1, 2q+1, 4q+1, \ldots \\ n &= 2q-1, 4q-1, \ldots \end{aligned} \tag{2.41}$$

A given armature harmonic can then be expressed as

$$J_{an} = J_n \sin(np\theta \mp \omega_e t) = J_n \sin(np\theta \mp p\omega_m t) \tag{2.42}$$

The total eddy current losses will be the superposition of the losses produced by each harmonic term. For the purposes of design, only the first two higher order harmonics will be considered. This approximation is valid because, as Eq. 2.41 shows, current density is inversely proportion to n, and eddy current losses are proportional to J^2 and hence $1/n^2$. Furthermore, losses for a given current density fall off very rapidly as n increases because the excitation wavelength falls and less field crosses the air gap and penetrates the magnets. Consequently, losses were observed to fall off by about an order of magnitude for each succeeding harmonic, so this approximation is nearly exact.

Note that the higher harmonic waves are travelling *more slowly* than the rotor, and will be time-varying in the frame of the rotor. In order to model the eddy current losses, the harmonics must be transformed into the stationary frame of the rotor. In the *stator* frame, the rotor is spinning with a rotational speed ω_m, so a stationary point on the rotor will appear at angle

$$\theta' = \theta - \omega_m t \tag{2.43}$$

Substituting this expression into Eq. 2.42 gives

$$J_{an} = J_n \sin(np(\theta' + \omega_m t) \mp p\omega_m t) = J_n \sin(np\theta' + p(n \mp 1)\omega_m t) \tag{2.44}$$

and from this point forward the rotor frame angle θ' will be noted as θ to simplify notation. Note that for the fundamental armature space harmonic, n is 1, so the armature wave appears stationary in the frame of the rotor, as we would expect.

This expression indicates that the higher order harmonics will be travelling backwards in space in the rotor frame, half at time harmonic order $(n + 1)$ and the other half at time harmonic order $(n - 1)$. If the higher order harmonics are paired in the form

$$\{2mq - 1, 2mq + 1\}$$

where m is an integer, as shown in Eq. 2.41, the time harmonic order as seen by the stator will be

$$n_t = (n \mp 1) = 2mq \tag{2.45}$$

for both harmonics in that pair. Eq. 2.44 can now be written

$$J_{an} = J_n \sin(np\theta + pn_t\omega_m t) = J_n \sin(np\theta + n_t\omega_e t) \tag{2.46}$$

For a three-phase machine, then, the first two higher order harmonics will be the 5th and 7th harmonics in space, and both will be 6th order harmonics in time. In the rotor frame, the lower order harmonic will appear to be travelling backwards at a rotational speed of $\frac{6}{5}\omega_m$, and the higher order harmonic will also be going backwards, at a speed of $\frac{6}{7}\omega_m$. These time-varying waves will drive eddy currents in the magnets.

• **Eddy current loss model** If a stationary, magnetically permeable material is exposed to a time-changing magnetic field, Faraday's Law

$$\nabla \times \boldsymbol{E} = -\mu \frac{\partial \boldsymbol{H}}{\partial t} \tag{2.47}$$

indicates that an electric field will be induced. If the material is also conducting, Ohm's Law

$$\boldsymbol{J} = \sigma \boldsymbol{E} \tag{2.48}$$

will give rise to currents in the material. These are called *eddy currents* and produce instantaneous Ohmic losses given by

$$P_i = \iiint_V \frac{\boldsymbol{J} \cdot \boldsymbol{J}}{\sigma} dV \tag{2.49}$$

The most straightforward way to calculate the eddy losses is to solve for the bulk current everywhere in the material and carry out this volume integral. The current can be found by combining Ampère's Law

$$\nabla \times \boldsymbol{H} = \boldsymbol{J} \tag{2.50}$$

with Eqs. 2.47 and 2.48 to obtain

$$\nabla \times \nabla \times \boldsymbol{H} = -\mu\sigma \frac{\partial \boldsymbol{H}}{\partial t} \tag{2.51}$$

Using the vector identity

$$\nabla \times (\nabla \times \boldsymbol{H}) = \nabla(\nabla \cdot \boldsymbol{H}) - \nabla^2 \boldsymbol{H} \tag{2.52}$$

and the fact that $\boldsymbol{H}$ is divergenceless, or

$$\nabla \cdot \boldsymbol{H} = 0 \tag{2.53}$$

gives the *diffusion equation*

$$\nabla^2 \boldsymbol{H} = -\mu\sigma\frac{\partial \boldsymbol{H}}{\partial t} \tag{2.54}$$

This partial differential equation describes the behavior of magnetic fields in the presence of permeable conductors.

Given appropriate boundary conditions, the diffusion equation can be solved for the magnetic fields in a conductor, and Ampère's Law can then be applied to give the current density in the conductor, which can be integrated to find the power loss. In practice, the mathematical complexity of this approach becomes prohibitive in a problem with more than one or two regions. The magnetic fields can be found in this manner, but for only slightly complicated problems a closed form solution to Eq. 2.49 may not exist, so the integration must be done numerically. This is very time-consuming and impractical for repeated design evaluations.

Fortunately, there is a much simpler method of solving the loss problem. This technique does not require solving for the bulk fields, but only those *at the material boundaries*. This analysis uses the *Poynting vector*

$$\boldsymbol{S} = \boldsymbol{E} \times \boldsymbol{H} \tag{2.55}$$

which describes the magnitude and direction of power flow in a region. Poynting's theorem

$$P_i = \iiint_V (\nabla \cdot \boldsymbol{S}) dV = \iint_A \boldsymbol{S} \cdot \hat{\boldsymbol{n}} dA = \iint_A (\boldsymbol{E} \times \boldsymbol{H}) \cdot \hat{\boldsymbol{n}} dA \tag{2.56}$$

indicates that instantaneous power into or out of a volume V is given by the flow of $\boldsymbol{S}$ across the surface A enclosing the region.

In this model, the eddy current loss can be found by assigning V to the rotor volume. Because the problem is formulated in the stationary frame of the rotor, there is no

mechanical power associated with rotor motion. Hence, all of the power captured in Poynting's vector is the power dissipated by Ohmic loss. If we assign the surface A to be the inside of the rotor and measure the power flowing radially into the rotor, this will give the rotor loss. If we define a cylindrical coordinate system, the component of interest is

$$S_r = -E_z H_\theta \tag{2.57}$$

It is then necessary to find the axial electric field and the azimuthal magnetic field at the inner surface of the rotor.

The fields E_z and H_θ will be induced by the current density of Eq. 2.46. They will time-varying at frequency $n_t\omega_e$ and will be phase shifted in space. In complex notation, they can be expressed as

$$E_z = \Re\{\hat{E}_z e^{j(np\theta + n_t\omega_e t)}\} \qquad H_\theta = \Re\{\hat{H}_\theta e^{j(np\theta + n_t\omega_e t)}\} \tag{2.58}$$

where $\hat{E}_z$ and $\hat{H}_\theta$ are complex quantities.

A method for finding these boundary fields in a problem with an arbitrary number of coupled regions has been thoroughly developed by Melcher [16] and is presented in Appendix E. It finds H_θ and the vector potential A_z at the material boundaries, given the armature current density, machine geometry and material properties.

A_z, like E_z and H_θ, will be of the form

$$A_z = \Re\{\hat{A}_z e^{j(np\theta + n_t\omega_e t)}\} \tag{2.59}$$

The relevant field E_z can be readily obtained from A_z by using Faraday's Law and substituting the definition of vector potential

$$\nabla\times\boldsymbol{E} = -\frac{\partial \boldsymbol{B}}{\partial t} = -\frac{\partial}{\partial t}(\nabla\times\boldsymbol{A}) = \nabla\times\left(-\frac{\partial \boldsymbol{A}}{\partial t}\right) \tag{2.60}$$

which can be applied termwise to give

$$E_z = -\frac{\partial}{\partial t}A_z = -jn_t\omega_e A_z \tag{2.61}$$

Substituting this expression into Eq. 2.57 gives

$$S_r = jn_t\omega_e A_z H_\theta \tag{2.62}$$

To find the total *time average* 2D rotor power loss P_r^{2D}, S_r can be integrated over the surface area of the inside of the rotor and averaged in time to give

$$P_r^{2D} = \frac{1}{\tau}\int_0^\tau \int_0^L \int_0^{2\pi} S_r r d\theta dz dt \Big|_{r = R_m} \tag{2.63}$$

This can be combined with Eqs. 2.58, 2.59, and 2.62 to yield

$$P_r^{2D} = \frac{1}{\tau}\int_0^\tau \int_0^L \int_0^{2\pi} jn_t\omega_e \Re\{\hat{A}_z e^{j(np\theta + n_t\omega_e t)}\}\Re\{\hat{H}_\theta e^{j(np\theta + n_t\omega_e t)}\} r d\theta dz dt \Big|_{r = R_m} \tag{2.64}$$

which integrates to

$$P_r^{2D} = \pi r L \Re\{jn_t\omega_e \hat{A}_z (\hat{H}_\theta)^*\}\Big|_{r = R_m} \tag{2.65}$$

where $(\hat{H}_\theta)^*$ denotes the complex conjugate of $\hat{H}_\theta$. This expression allows for computationally efficient evaluation of rotor eddy current losses.

• **3D effect of machine length** The 2D loss model assumes that the machine is infinitely long in the z direction, so that eddy currents are only z directed. In actuality, these currents must terminate at the end of the rotor and "turn around", forming current

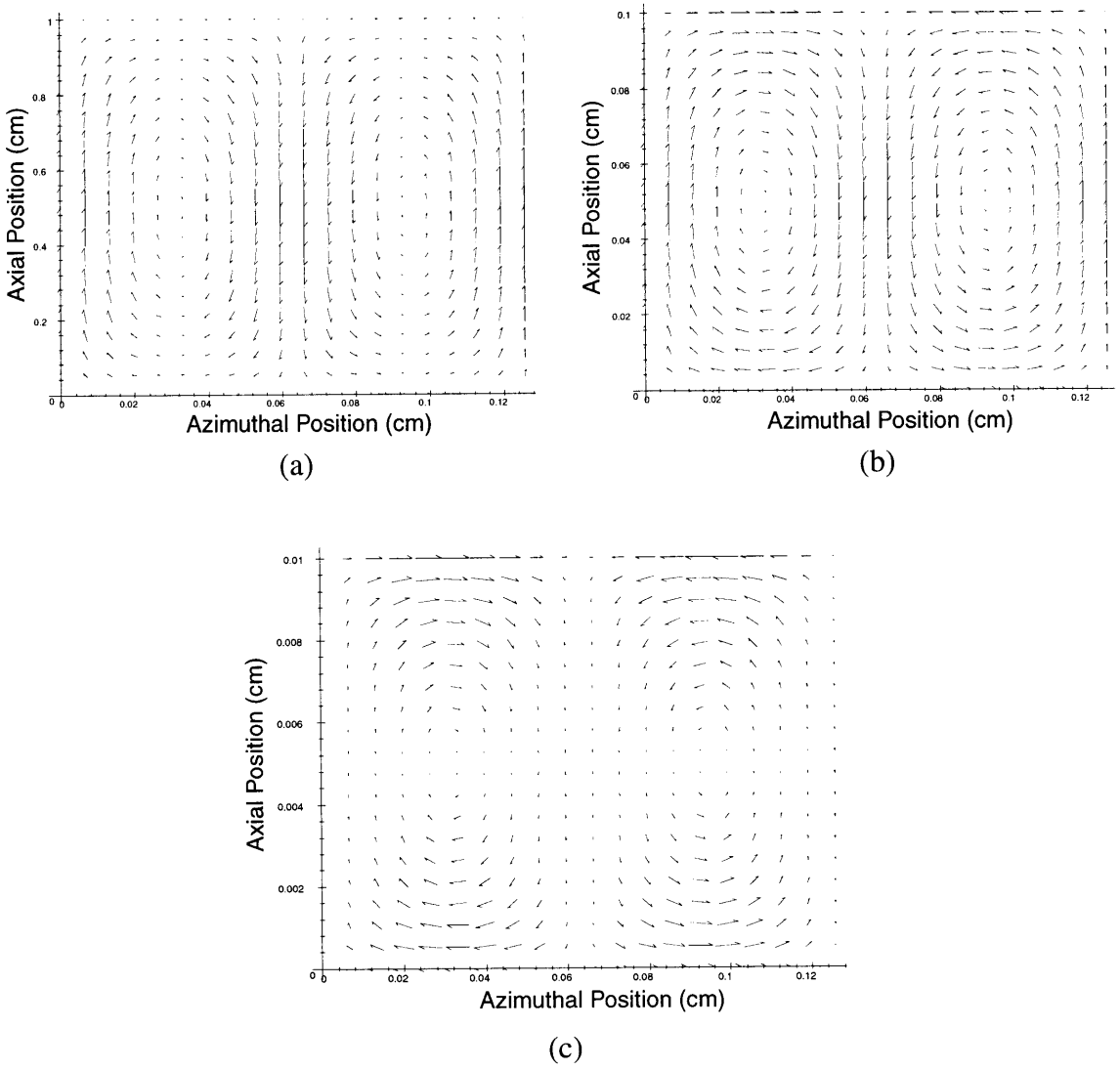

Figure 2.8: Eddy current loops over one wavelength for machines with (a) axial length >> wavelength, (b) axial length = wavelength, and (c) axial length << wavelength

loops like those illustrated in Fig. 2.8. As the axial length of the machine decreases, this effect will become more pronounced and will tend to impede current flow, reducing losses. This is the same principle that motivates the axial lamination of iron cores in electric machines. To further develop the accuracy of the loss model, and allow for a wide range of machine dimensions, a machine length coefficient k_l is derived in Appendix F. This coefficient approaches unity as the machine becomes infinitely long, and begins to

attenuate the losses when the machine length is comparable to the wavelength of excitation, reaching zero when the length is zero. The expression for k_l is

$$k_l = \sum_{\text{m odd}} \frac{8}{\pi^2}\left(\frac{np}{R_{avg}}\right)\frac{1}{m^2}\frac{1}{\left(\frac{m\pi}{L}\right)^2 + \left(\frac{np}{R_{avg}}\right)^2} \tag{2.66}$$

where R_{avg} is the average magnet radius

$$R_{avg} = \frac{R_m + R_s}{2} \tag{2.67}$$

The complete expression for rotor eddy current losses is then

$$P_r = P_r^{2D} k_l = \pi r L k_l \Re\{ j n_t \omega_e \hat{A}_z (\hat{H}_\theta)^* \}\Big|_{r = R_m} \tag{2.68}$$

2.5.4 Other Machine Attributes

In addition to power rating and losses, there are three other machine attributes: material weight, material cost and length.

• **Material weight** The material weight w_t will be the sum of the copper weight w_c and the magnet weight w_m, which can be expressed

$$\begin{aligned} w_c &= \rho_c q N_a l_t N_{par} \pi\left(\frac{d_w}{2}\right)^2 \\ w_m &= \rho_m L \pi[(R_s)^2 - (R_m)^2] \end{aligned} \tag{2.69}$$

• **Material cost** The cost of the materials will then be

$$C_t = w_c C_c + w_m C_m \tag{2.70}$$

• **Length** The overall machine length is

$$l_o = L + 2h_t \tag{2.71}$$

where h_t is the end turn height derived in Appendix C.

This completes the analytical models of the permanent-magnet synchronous machine. In the next chapter, these analytical models will be verified using finite element analysis.

Chapter 3

Model Verification by Finite Element Analysis

3.1 Introduction

In this chapter, the Ansoft *Maxwell* 2D finite element analysis (FEA) software package [17] is used to verify the analytic models derived in the previous chapter. This software allows input of a machine geometry as well as material properties (including magnetization), current sources, and boundary conditions. Finite element analysis breaks up the geometry of the problem into adjacent triangles, and solves for the field in each element. The number of elements can be increased to allow for the desired model accuracy. The software produces graphical field plots, as well as numerical calculation of torque and eddy current loss.

The objective is to use FEA to verify the models of magnet- and armature-produced magnetic fields, machine torque, and 2D eddy current losses in a PMSM machine. This software package did not offer 3D analysis, so no attempt was made to verify the 3D eddy current loss model.

Two representative machines were chosen and their attributes calculated with the analytical models. The relevant results are summarized in Table 3.1. These designs are not optimized for performance, but they are reasonable machines that meet all of the design requirements. The choice of only 1 or 2 pole pairs reflects a desire to increase the accuracy of the finite element analysis by decreasing the resolution of machine geometry. Experiments with the software found that accuracy began to erode for more than 3 or 4 pole pairs. As the following results demonstrate, analytical model predictions agreed with FEA results to within about 1% error for all measured attributes. Relevant graphs and figures are collected at the end of this chapter.

	Variable	Machine A	Machine B	Units
Specifications	P_{mech}	10,000	35,000	W
	RPM_{min}	20,000	30,000	RPM
	V	100	155	V
Parameters	R_{ai}	3.5	8.0	cm
	t_a	1.0	2.0	cm
	g	0.15	0.2	cm
	t_m	0.5	0.75	cm
	p	1	2	pole pairs
	L	10	3	cm
	N_{ac}	1250	5000	conductors
	B_r	1.2	1.2	T
	μ_r	1.14	2.00	unitless
	σ_r	7.0×10^5	2.5×10^4	S/m
Attributes	N_a	75	106	turns
	I	37.7	80.1	A
	δ	26.9	28.9	degrees
	P_r^{2D}	12.98	5.00	W
	P_r^{3D}	10.52	1.94	W

Table 3.1: Sample machines for finite element analysis

3.2 Stationary Field Analysis

To analyze the stationary magnetic fields in the machine, *Maxwell*'s magnetostatic module was used. This package analyzes field phenomena that result from stationary field properties, including electromechanical torque. The machine geometries were rendered in the *Maxwell* environment and are pictured in Figs. 3.1 and 3.14. The angle ϕ indicates the rotation of the rotor around the stationary armature. The arrows indicate the direction of permanent magnetization for each magnet in the Halbach array, and the letters A, B, and C

indicate the armature phases. The software was versatile enough to accommodate radial and azimuthal magnetization with a $1/r$ dependence, as specified in the magnet field model outlined in Appendix B.

Figs. 3.2 and 3.15 illustrate the element mesh that *Maxwell* automatically generated for each machine. The solution process is iterative, so that regions with intense magnetic fields are more densely modeled in each succeeding solution step. Calculation of field quantities and machine parameters tends to stabilize after about 5,000 triangles are generated, but for more complex geometries more triangles are needed to ensure accuracy. In this problem, calculations and plots for the two-pole Machine *A* used about 5,000 triangles, while the four-pole Machine *B* required about 8,000 triangles.

• **Magnet-produced magnetic field and flux density** Figs. 3.3 and 3.16 are *Maxwell* contour plots of the magnetic flux density in the two machines. To verify the magnet-produced magnetic field model derived in Appendix B, the symbolic analysis package *Maple* [18] was used to produce a plot of the Fourier series for magnetic flux density summarized by Eq. B.32. Figs. 3.4(a) and 3.17(a) are plots of this field at the inner armature radius for each machine. Figs. 3.4(b) and 3.17(b) are *Maxwell* plots of the flux density at the same radius.

• **Armature magnetic field and flux density** Figs. 3.5 and 3.18 illustrate the FEA plot of armature-produced magnetic fields for both machines. In these graphs, note that the axis of magnetic field is offset ($\phi = \delta$), reflecting the torque angle of each machine. Figs. 3.6(a) and 3.19(a) are *Maple* plots of the analytical expressions for armature flux density derived in Appendix A and summarized by Eq. A.32. In these plots, the field is evaluated at the armature inner radius, with the current vector aligned with the center of phase A. Figs. 3.6(b) and 3.19(b) are FEA calculations of the same quantity. For both field

plots, analytical predictions match nearly exactly with FEA results. The superposition of these two fields gives the complete machine magnetic field, which is pictured in Figs. 3.7 and 3.20.

3.3 Torque Analysis

Torque, unlike eddy currents, results from static interaction of fields and is independent of material motion, so magnetostatic time-stationary methods can be applied. *Maxwell* has a torque calculation module that allows for the direct computation of torque per unit depth produced by a two-dimensional geometry. However, the magnetostatic package only finds instantaneous quantities, while the torque expressions presented in Sec. 2.5.2 are time-average quantities. While *time-average,* nonzero constant torque will be produced by the fundamental magnet field, the higher order terms will give rise to a *time-varying,* zero time-average torque that causes a ripple in the torque characteristic.

To correct for this, an expression for time-varying torque can be constructed by starting with the expression for the magnet field Fourier series, Eq. B.32, and then finding the flux linked by each armature phase for each Fourier term, following the method of Sec. B.2. The torque produced by the entire machine is then the sum of the Fourier series for each armature phase. Plots of this quantity were obtained with *Maple* and are pictured for each machine in Figs. 3.8(a) and 3.21(a). Note that the torque ripple is periodic in the number of phase belts, as would be expected from the symmetry of the machine. More detailed plots of the torque ripple over one cycle are presented in Figs. 3.8(b) and 3.21(b).

To test the model, the instantaneous torque was computed with the calculated torque angle at seven rotor angles spaced over one phase belt. The results matched the predictions very closely, with errors of less than 1 percent, and are summarized in Table 3.2 as well as

Machine	Rotor Angle (ϕ)	Model Torque (N·m)	FEA Torque (N·m)	Error
A	0°	4.28	4.27	0.2%
A	10°	4.72	4.71	0.2%
A	20°	5.28	5.31	0.6%
A	30°	5.16	5.23	1.4%
A	40°	4.83	4.83	0.0%
A	50°	4.36	4.38	0.5%
A	60°	4.28	4.28	0.0%
Average		4.77	4.72	0.4%
B	0°	10.34	10.28	0.6%
B	5°	11.10	11.16	0.5%
B	10°	11.98	12.03	0.4%
B	15°	11.82	11.91	0.8%
B	20°	11.19	11.24	0.4%
B	25°	10.42	10.32	1.0%
B	30°	10.34	10.37	0.3%
Average		11.17	11.04	0.6%

Table 3.2: Comparison of analytical torque predictions and FEA calculations

illustrated by the data points on Figs. 3.8(b) and 3.21(b). These accurate results for both machines reasonably verify the machine rating model.

3.4 Eddy Current Loss Analysis

In this section the *Maxwell* eddy current module is used to predict the time varying fields and eddy current losses in the problem. Because only the 5th and 7th armature space harmonics will produce significant eddy current losses, the armature was constructed as the superposition of these current density waves, with magnitudes given by Eq. 2.41. *Maxwell* only allows for one frequency of excitation, but these harmonics have the same

time frequency so can be superimposed in this way.

The software only allows for standing waves of current density, but travelling waves are the sum of two standing waves, each with the same amplitude as the travelling wave, and which each produce half of the time-average eddy current losses. Hence, in the FEA current densities were specified as standing waves with the same amplitude as the travelling wave being analyzed, and the corresponding time-average losses were doubled to compensate.

Plots of the finite element mesh for this simulation are picture in Figs. 3.9 and 3.22. Again, more triangles were included in the four-pole machine analysis to ensure accurate results. The calculated magnetic fields are shown in Figs. 3.10 and 3.23, and the resulting eddy current contours are pictured in Figs. 3.11 and 3.24. As indicated by Eq. 2.65, the eddy current losses can be characterized by H_θ and A_z at the inner radius of the magnets. These quantities were computed analytically using the most accurate of the four methods described in Appendix E (Model IV in Table E.1) and the results plotted with *Maple*. These quantities were also calculated with FEA and a comparison of the results is pictured in Figs. 3.12 and 3.13 for Machine *A*, and Figs. 3.25 and 3.26 for Machine *B*. Again, the calculated fields are very nearly the same as the analytically derived fields.

Maxwell also computes total eddy current power loss, and the results are presented in Table 3.3 along with the model predictions. The errors are again acceptably small, so the finite element analysis verification of the motor alternator analytical models is complete.

Machine	Model Eddy Current Loss (W)	FEA Eddy Current Loss (W)	Error
A	12.98	12.87	0.9%
B	5.00	4.94	1.2%

Table 3.3: Comparison of analytical eddy current loss predictions and FEA calculations

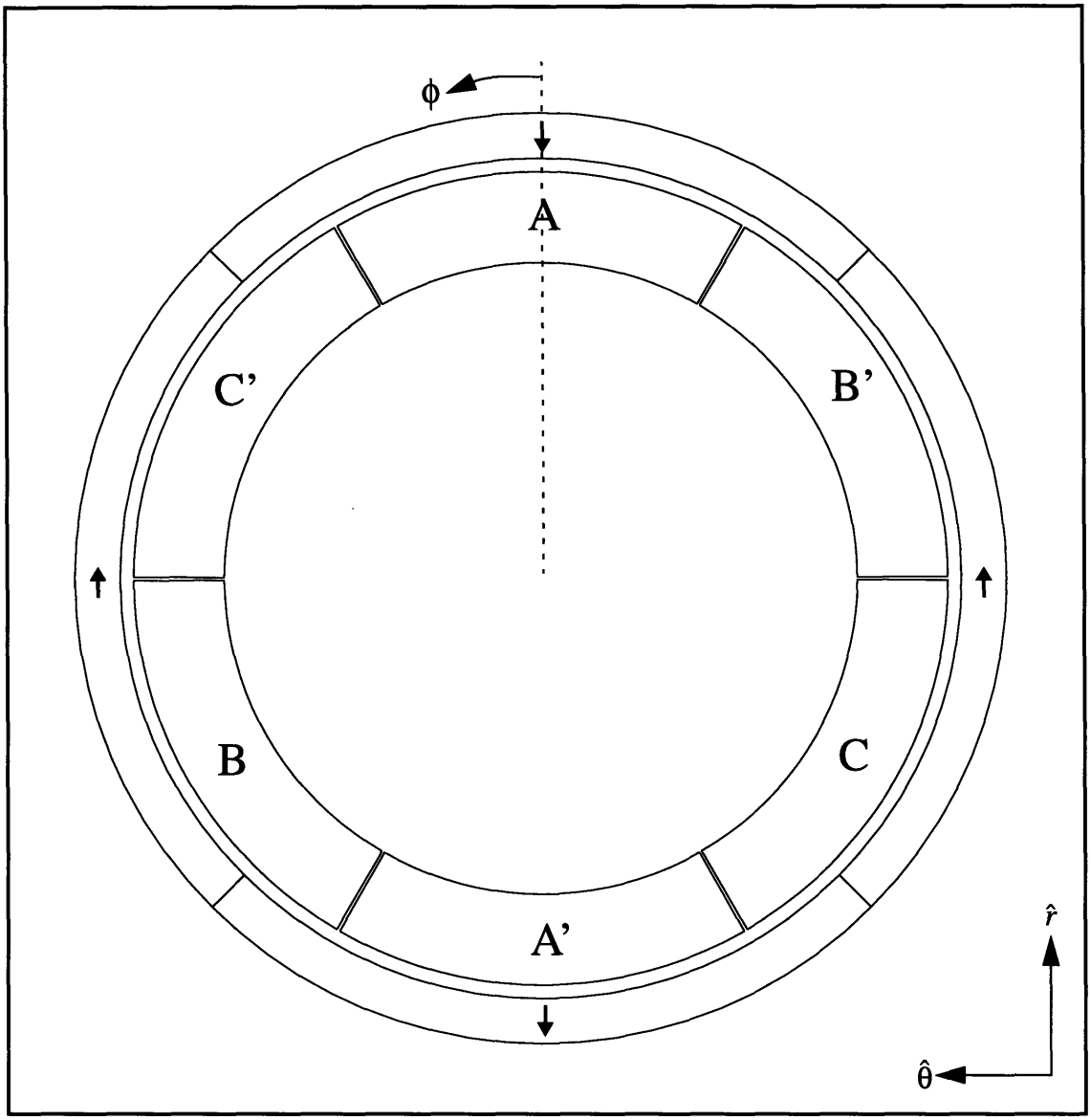

Figure 3.1: Machine *A* geometry generated in *Maxwell*

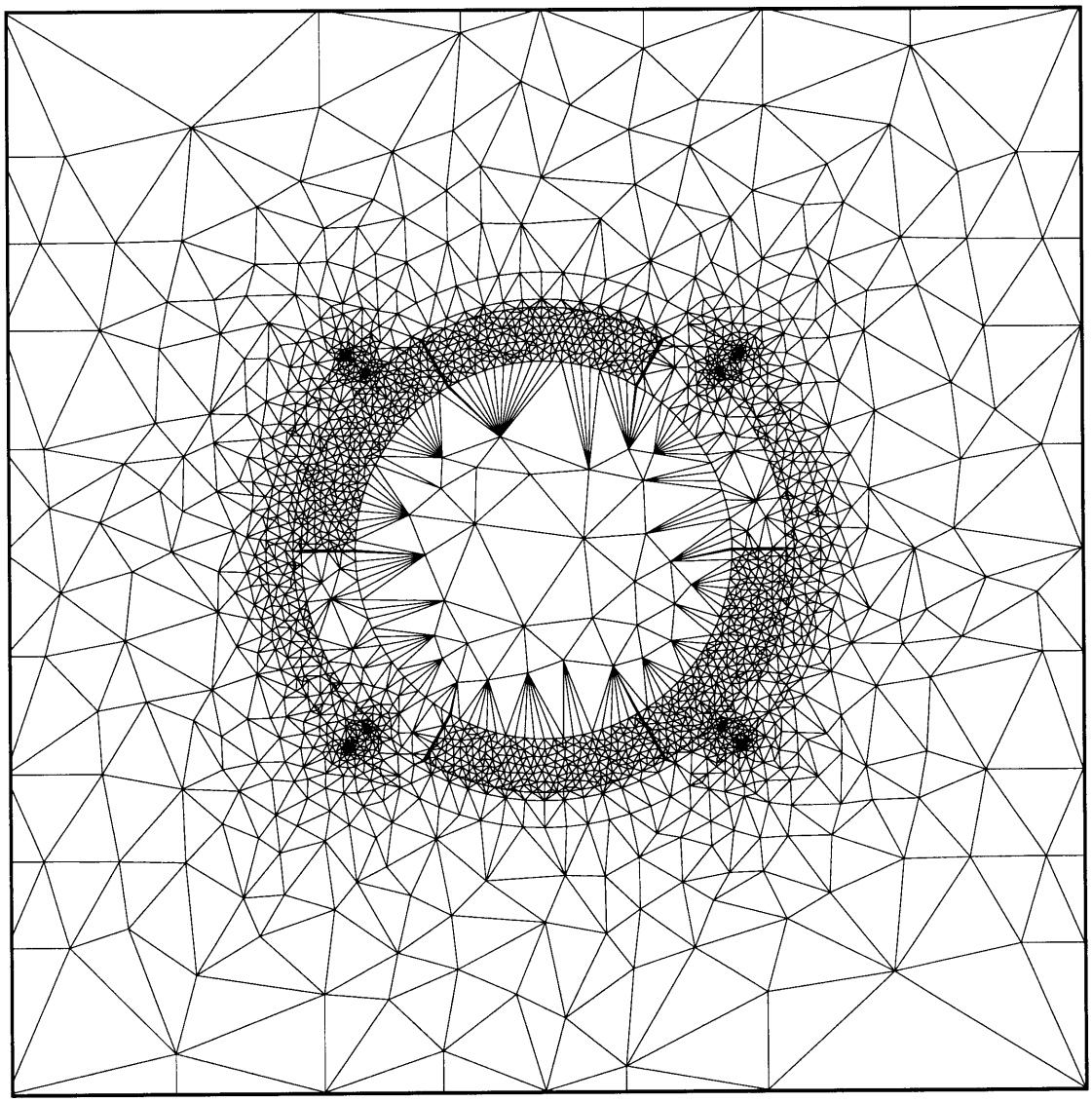

Figure 3.2: Machine *A* finite element mesh for torque analysis

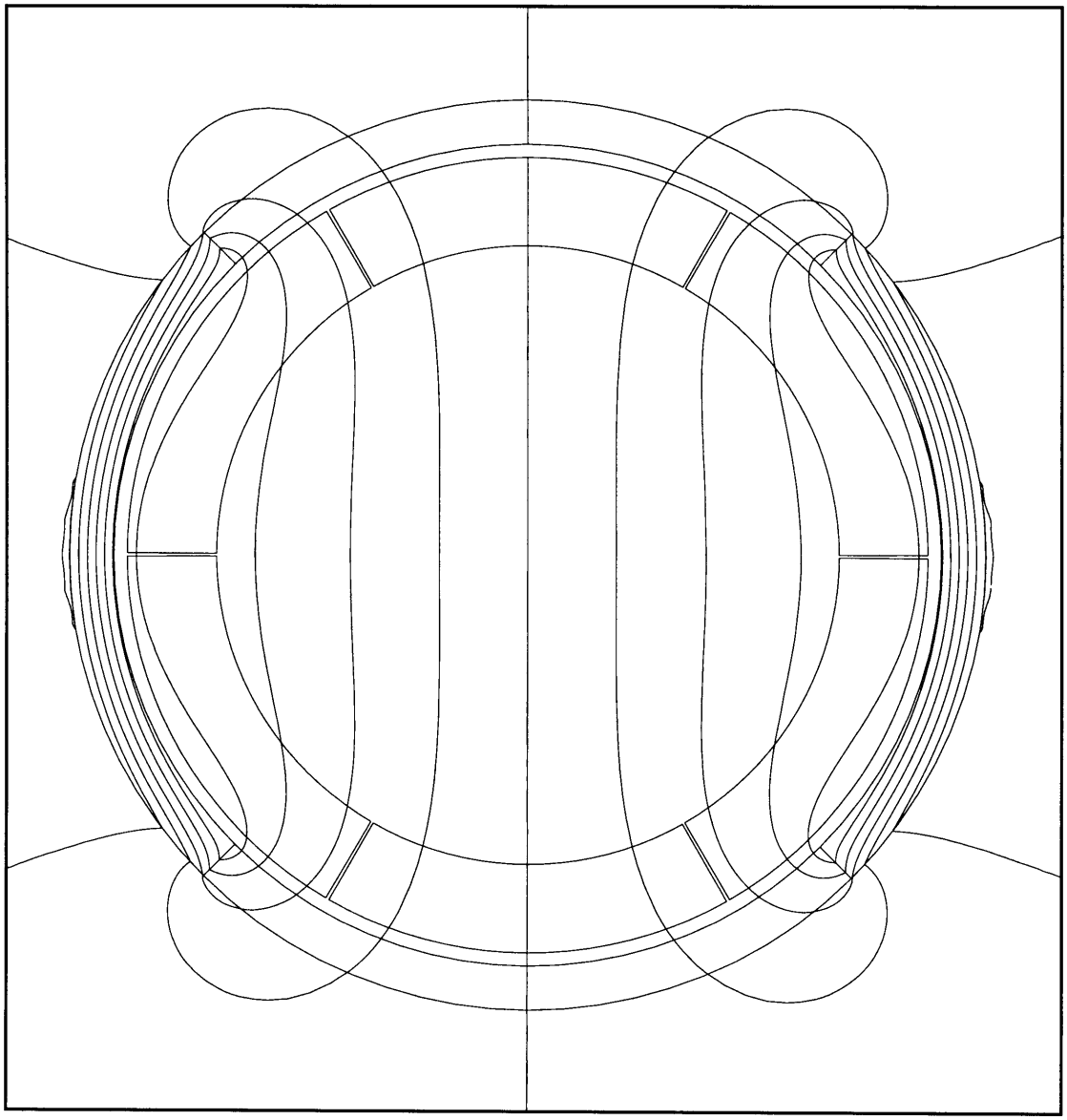

Figure 3.3: Machine *A* magnet-produced magnetic fields

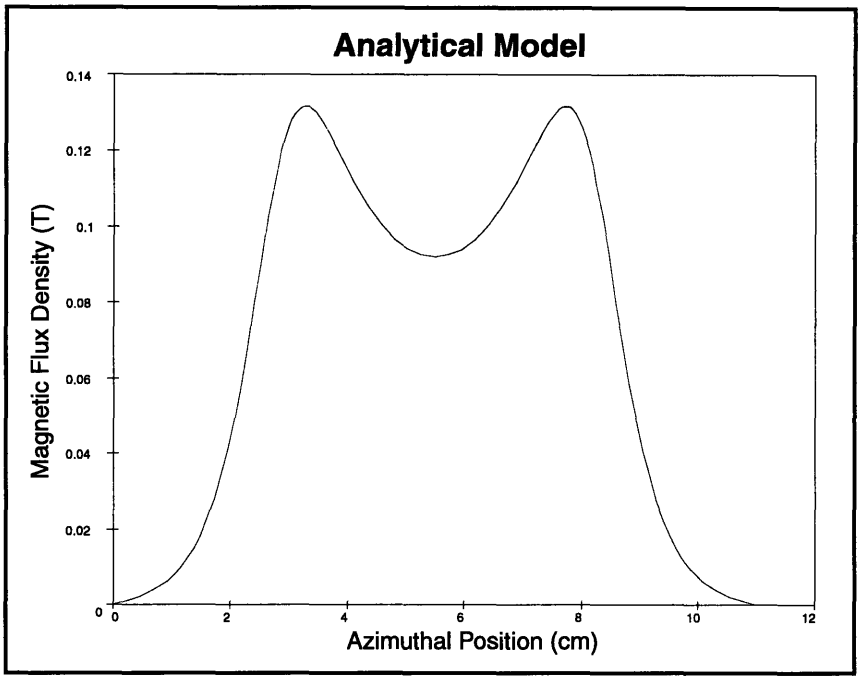

(a)

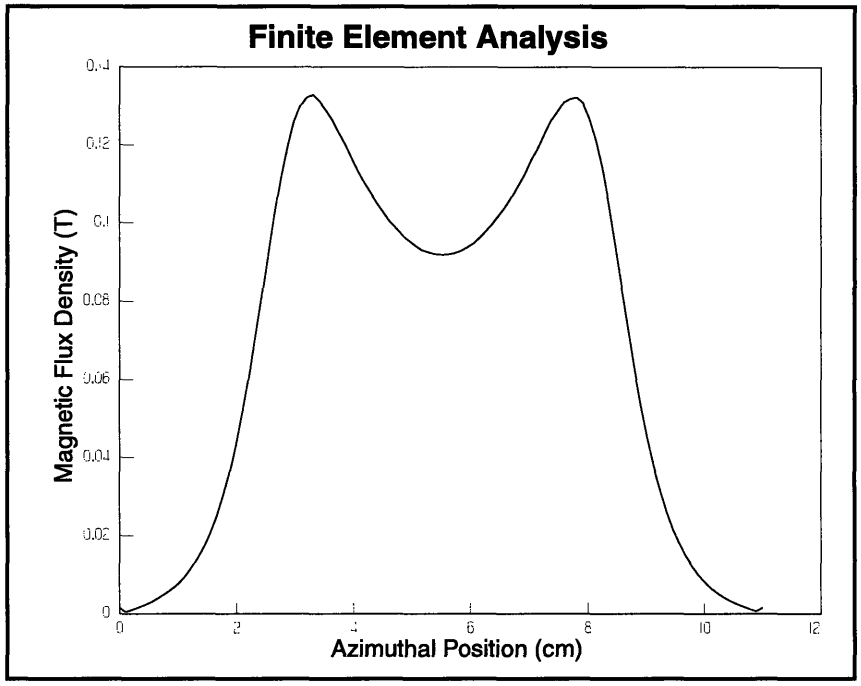

(b)

Figure 3.4: Comparison of (a) *Maple* plot of analytical model and (b) *Maxwell* finite element analysis of magnet-produced magnetic flux density at inner armature radius of Machine *A*

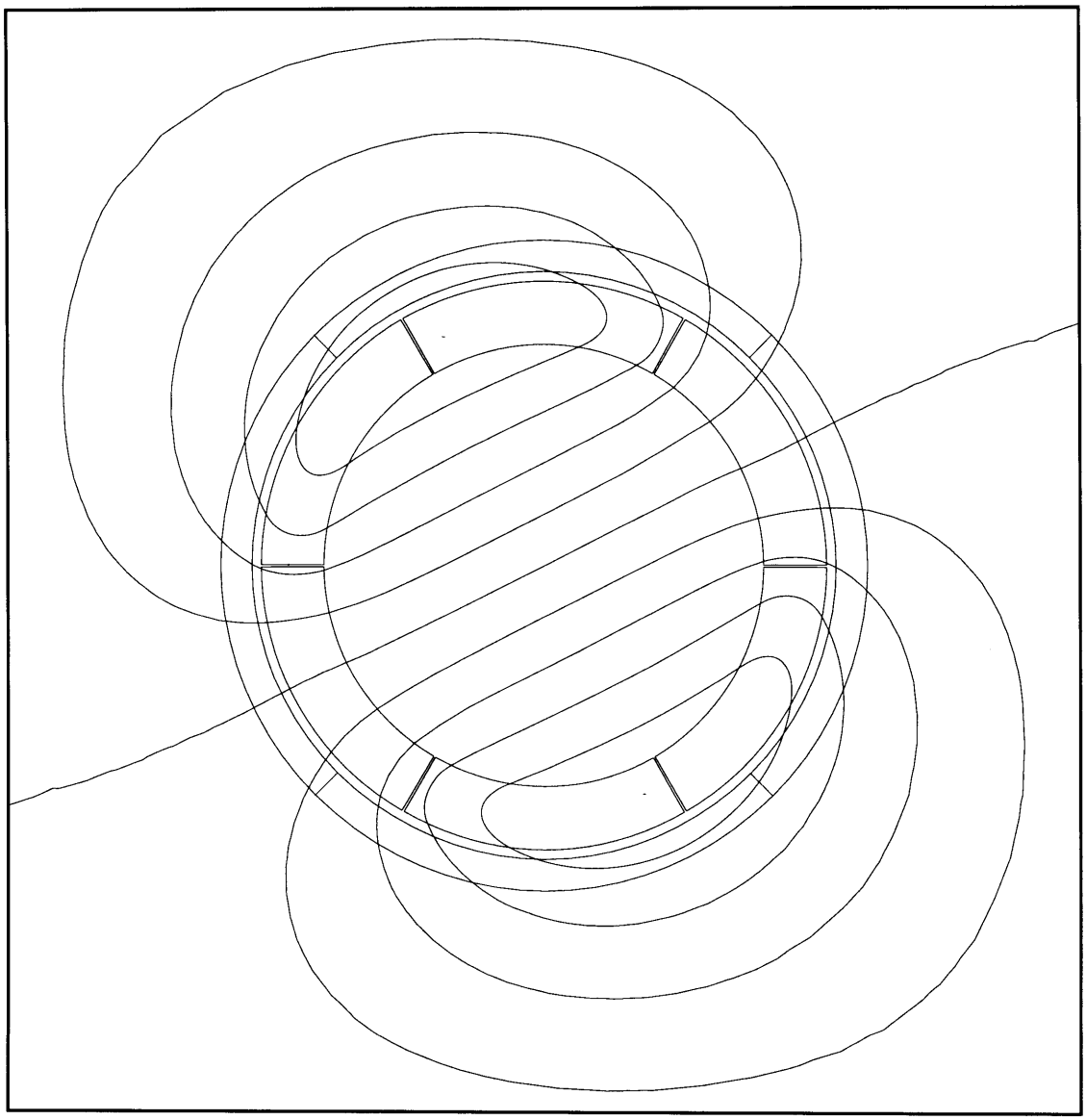

Figure 3.5: Machine *A* armature magnetic field

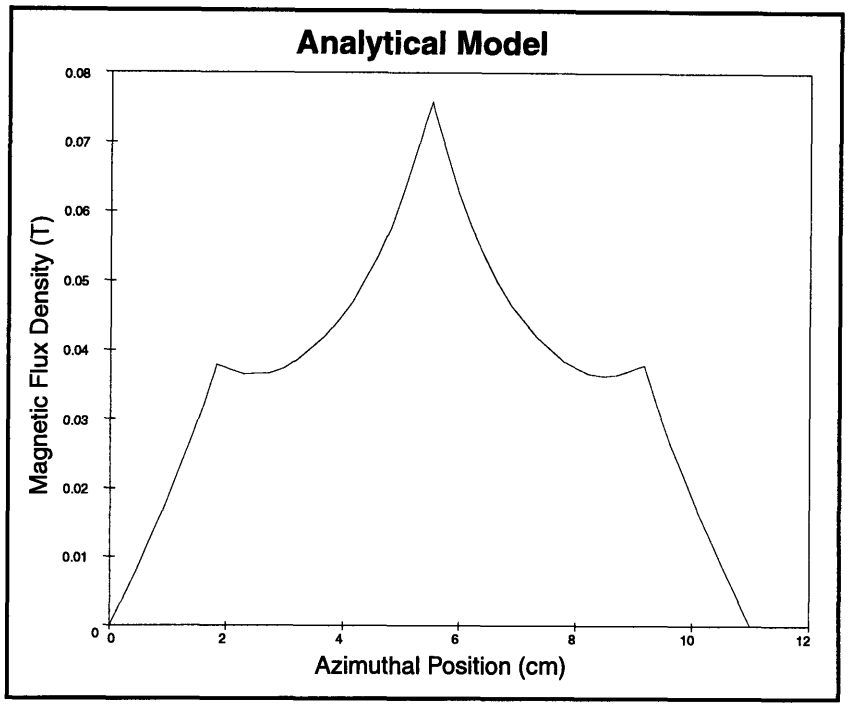

(a)

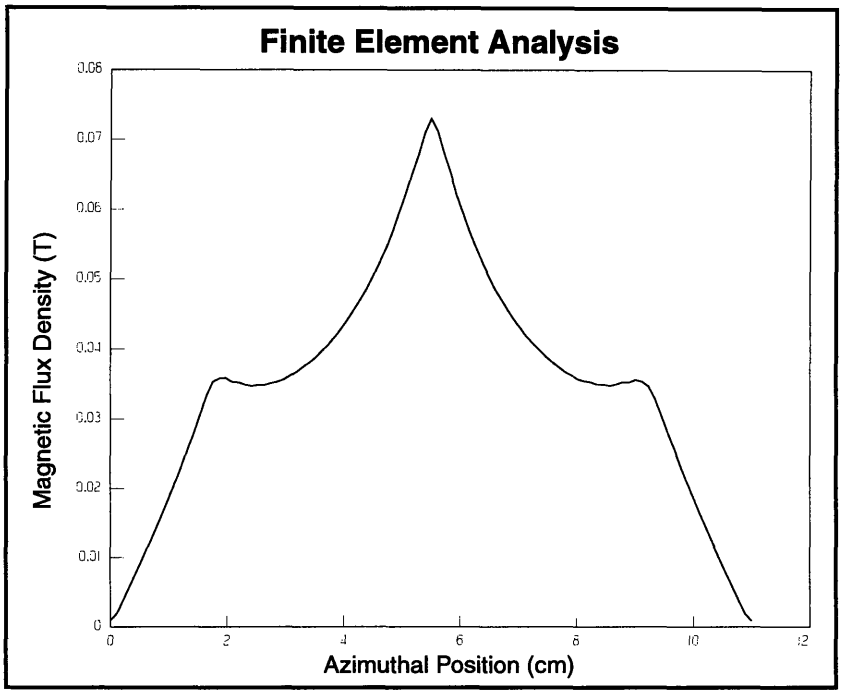

(b)

Figure 3.6: Comparison of (a) *Maple* plot of analytical model and (b) *Maxwell* finite element analysis of armature magnetic flux density at inner armature radius of Machine *A*

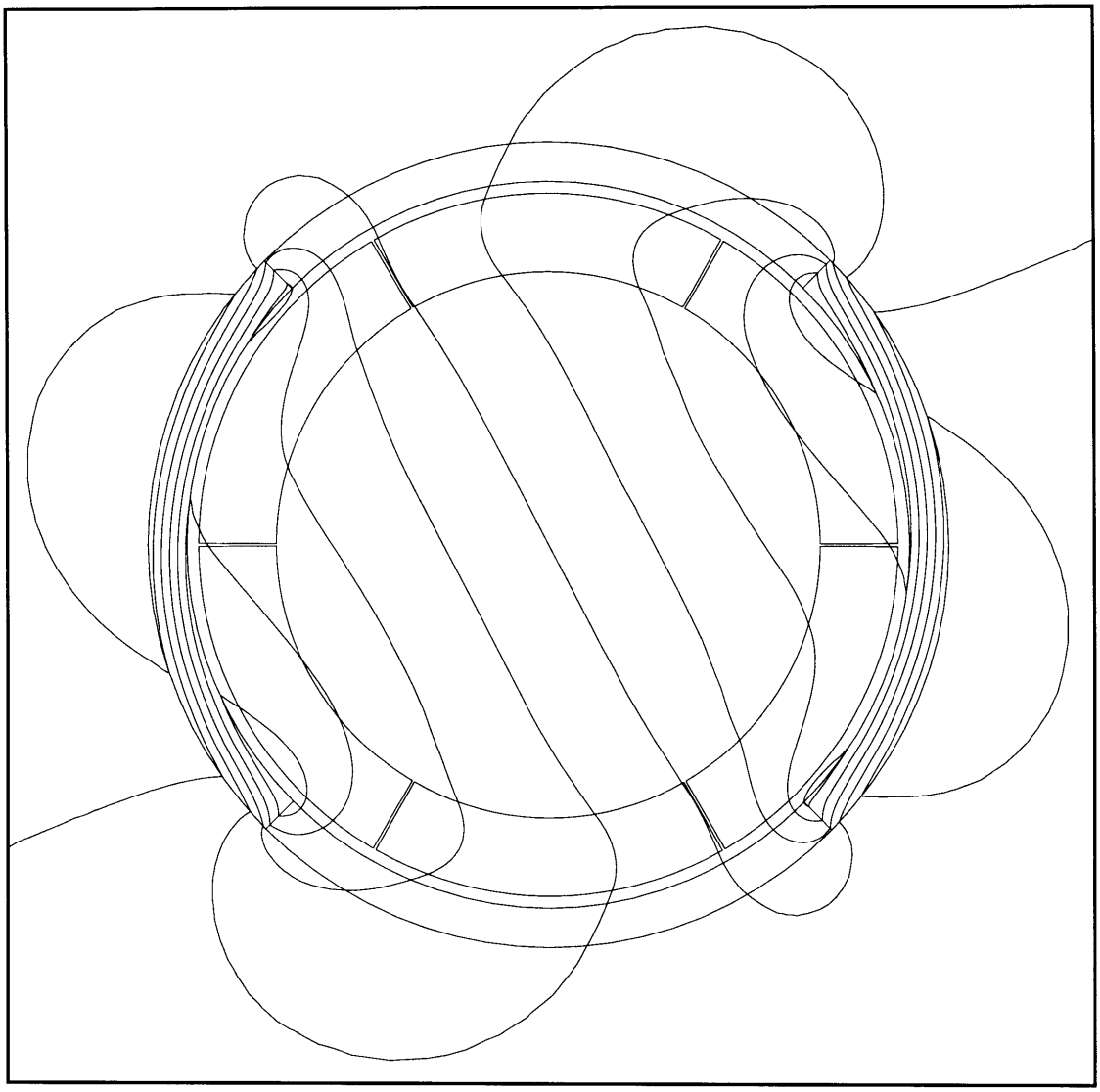

Figure 3.7: Machine *A* complete magnetic field

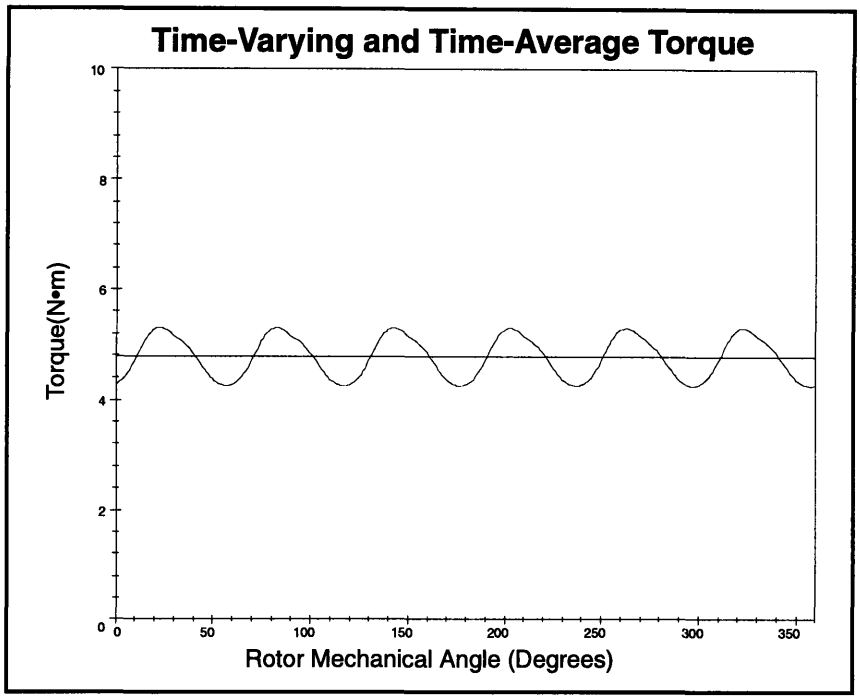

(a)

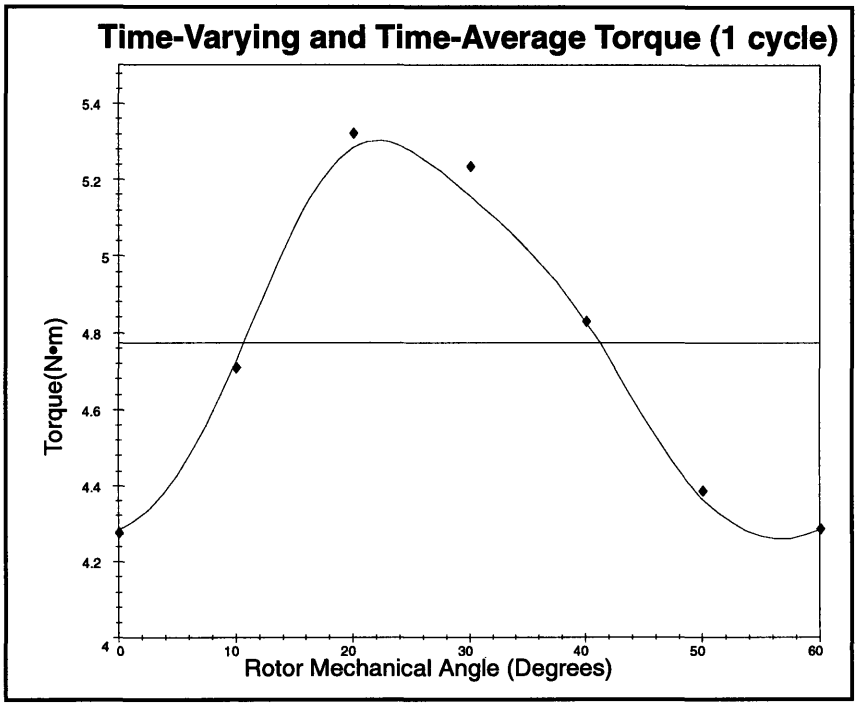

(b)

Figure 3.8: Time-varying and time-average torque of Machine *A* over (a) one full rotor rotation and (b) one cycle. The ♦ marks in plot (b) indicate FEA calculations.

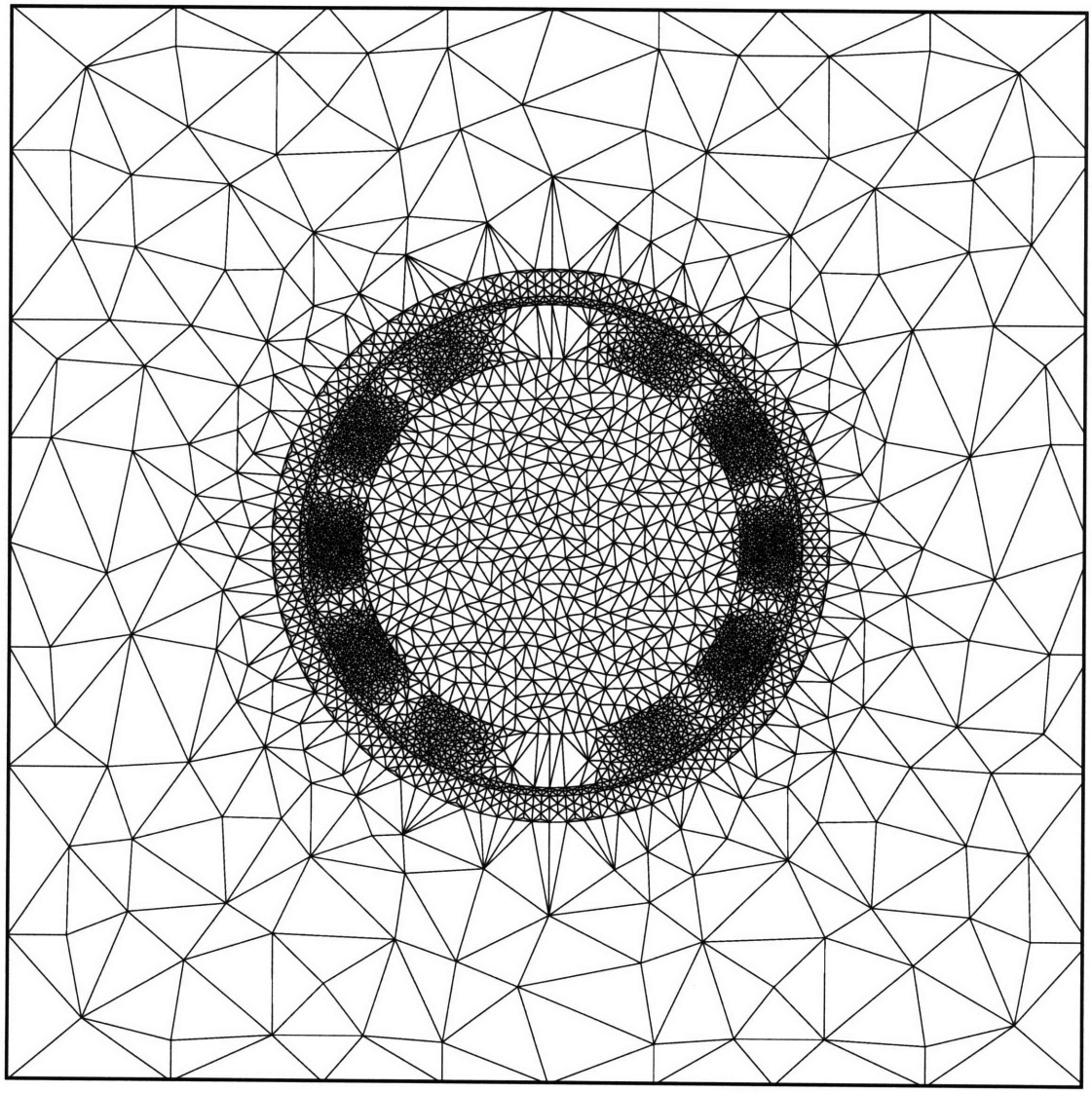

Figure 3.9: Machine *A* finite element mesh for eddy current analysis

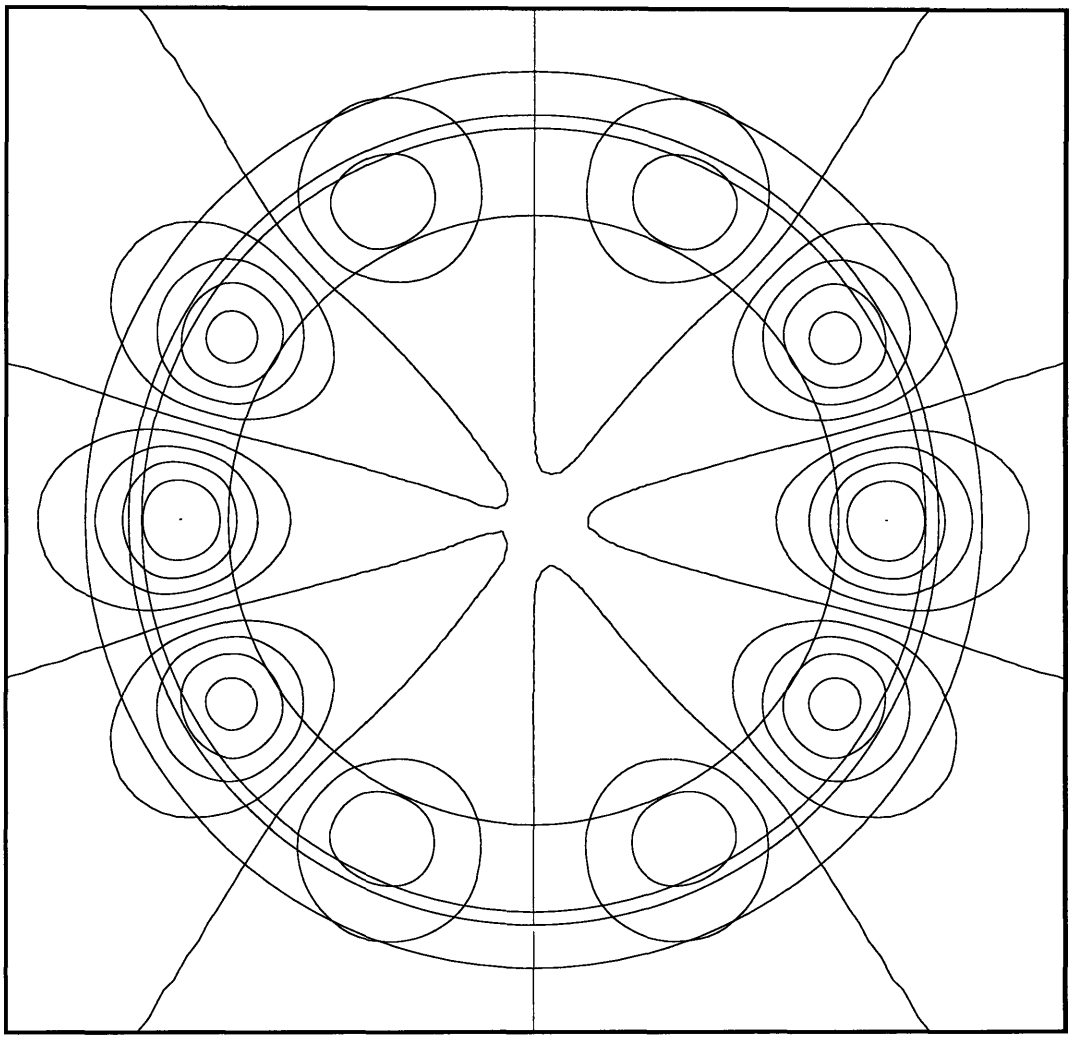

Figure 3.10: 5th and 7th harmonics of Machine *A* time-varying magnetic field

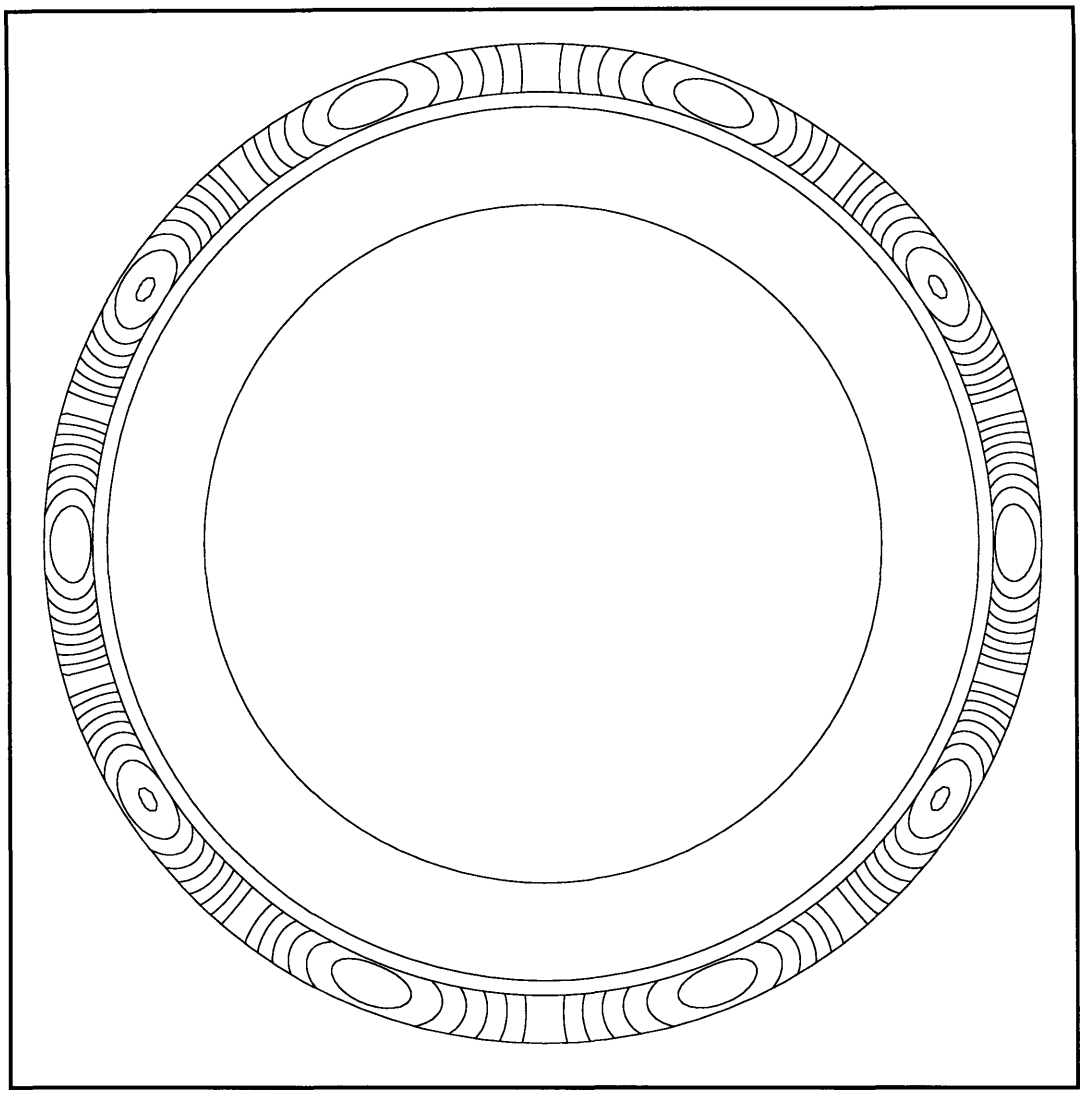

Figure 3.11: 5th and 7th harmonics of Machine *A* eddy currents

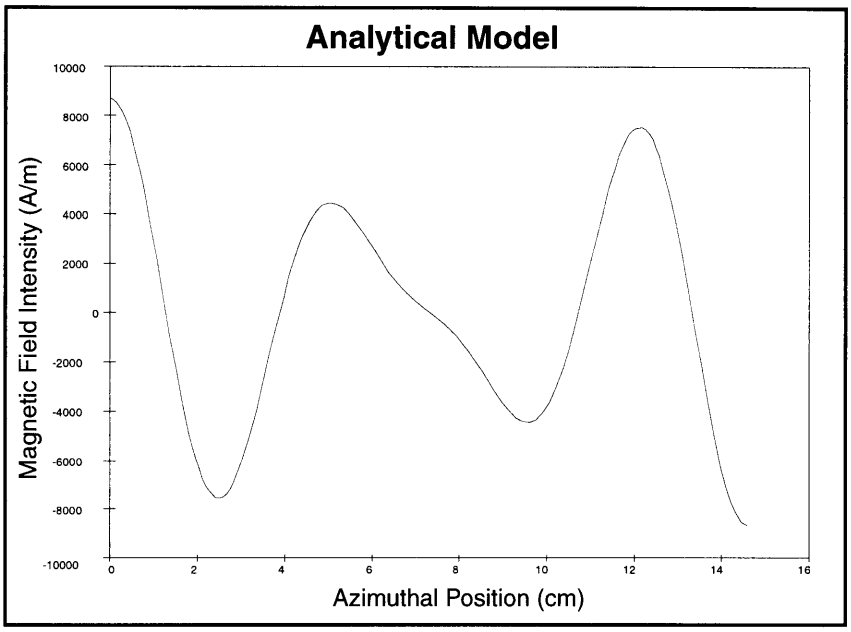

(a)

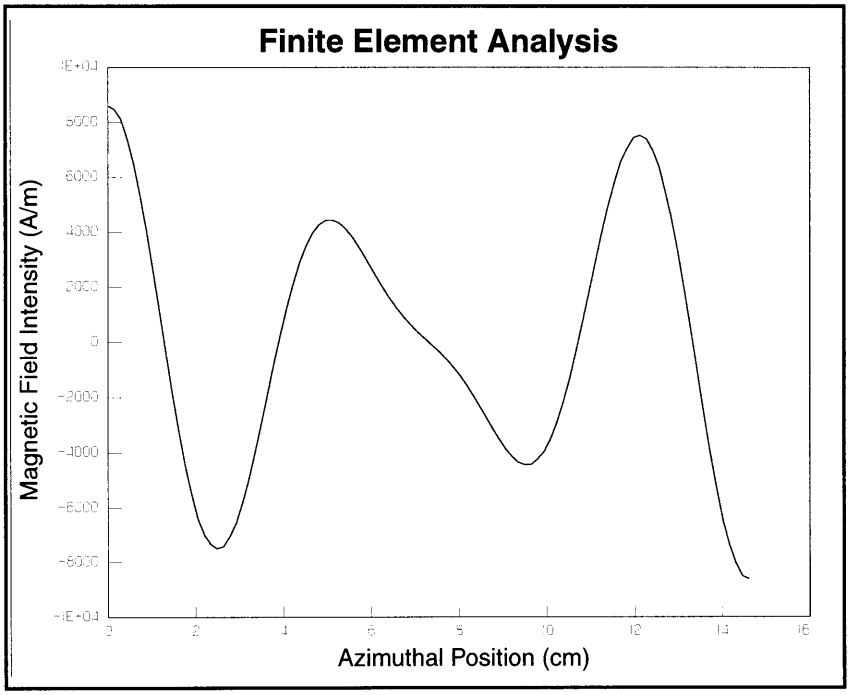

(b)

Figure 3.12: Comparison of (a) *Maple* plot of analytical model and (b) *Maxwell* finite element analysis of time-varying magnetic field intensity at inner magnet radius of Machine *A*

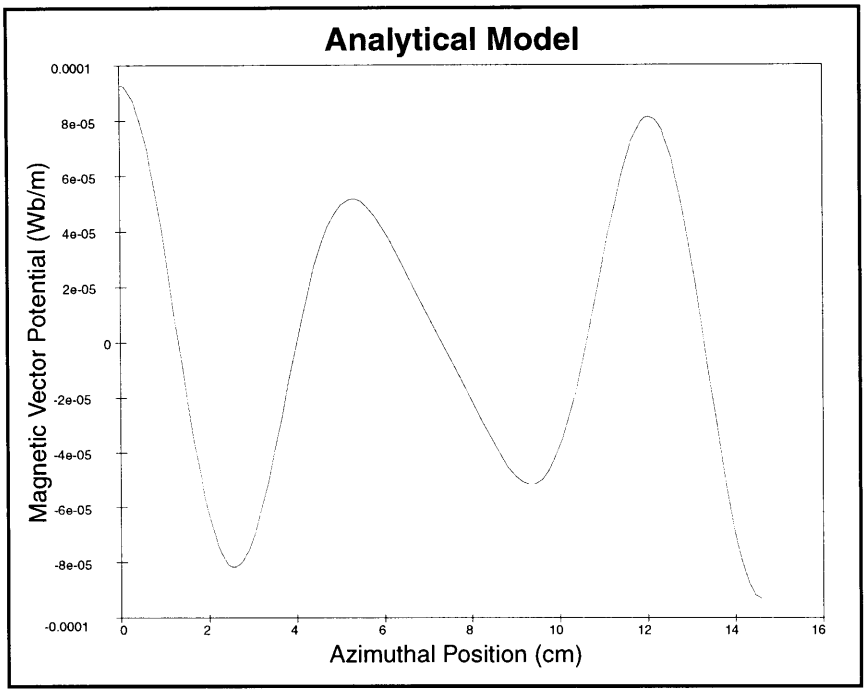

(a)

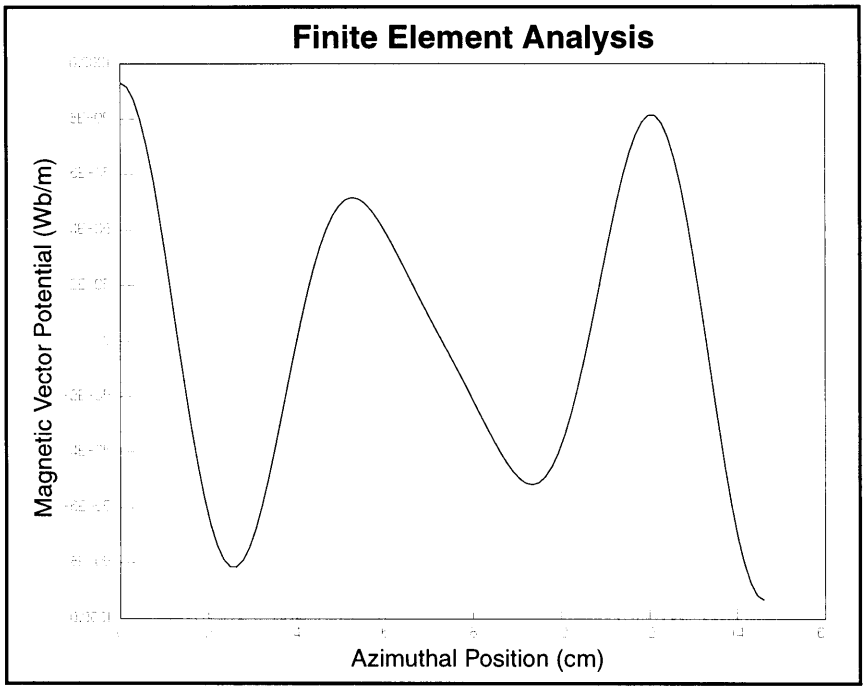

(b)

Figure 3.13: Comparison of (a) *Maple* plot of analytical model and (b) *Maxwell* finite element analysis of time-varying magnetic vector potential at inner magnet radius of Machine *A*

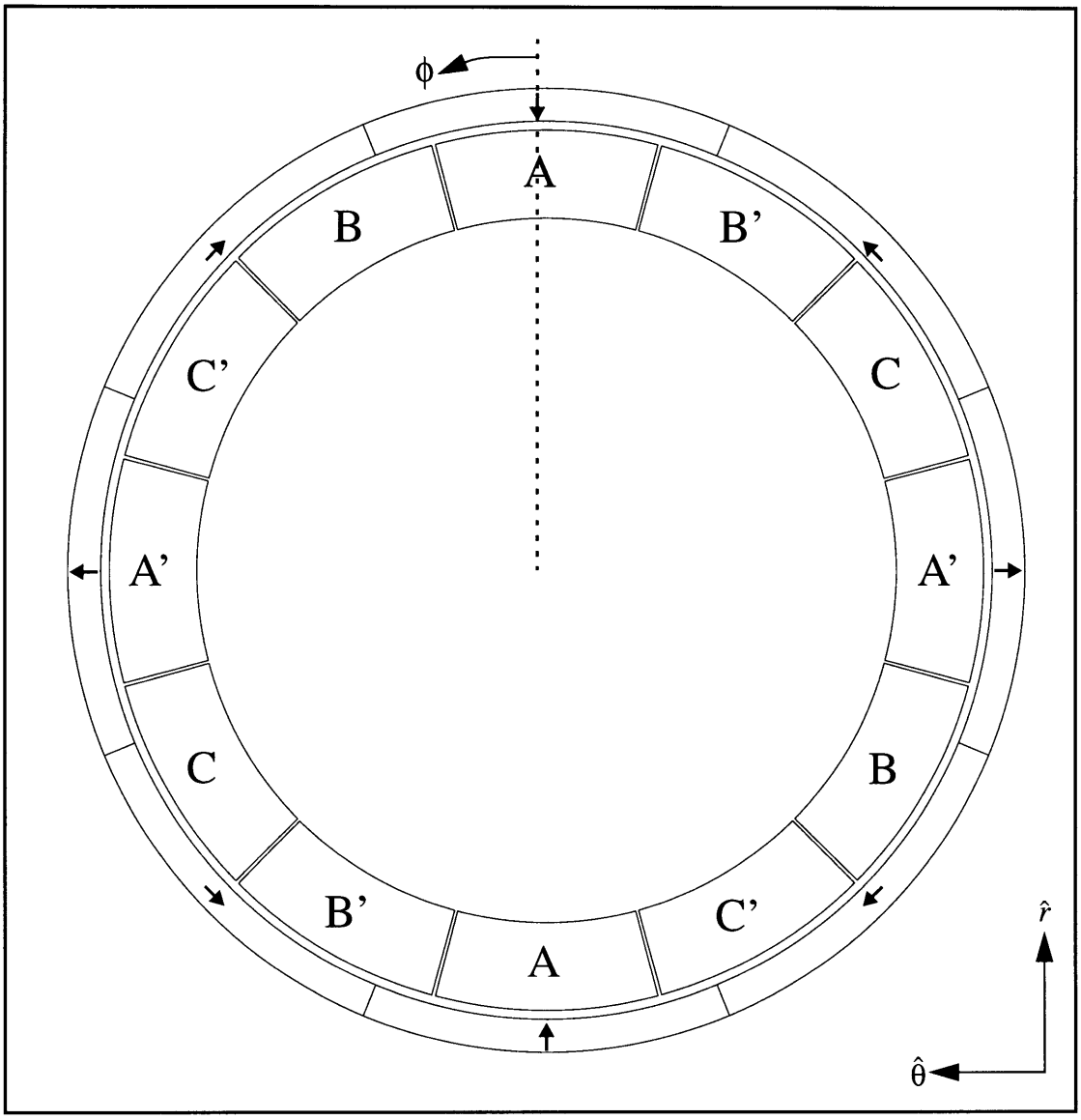

Figure 3.14: Machine *B* geometry generated in *Maxwell*

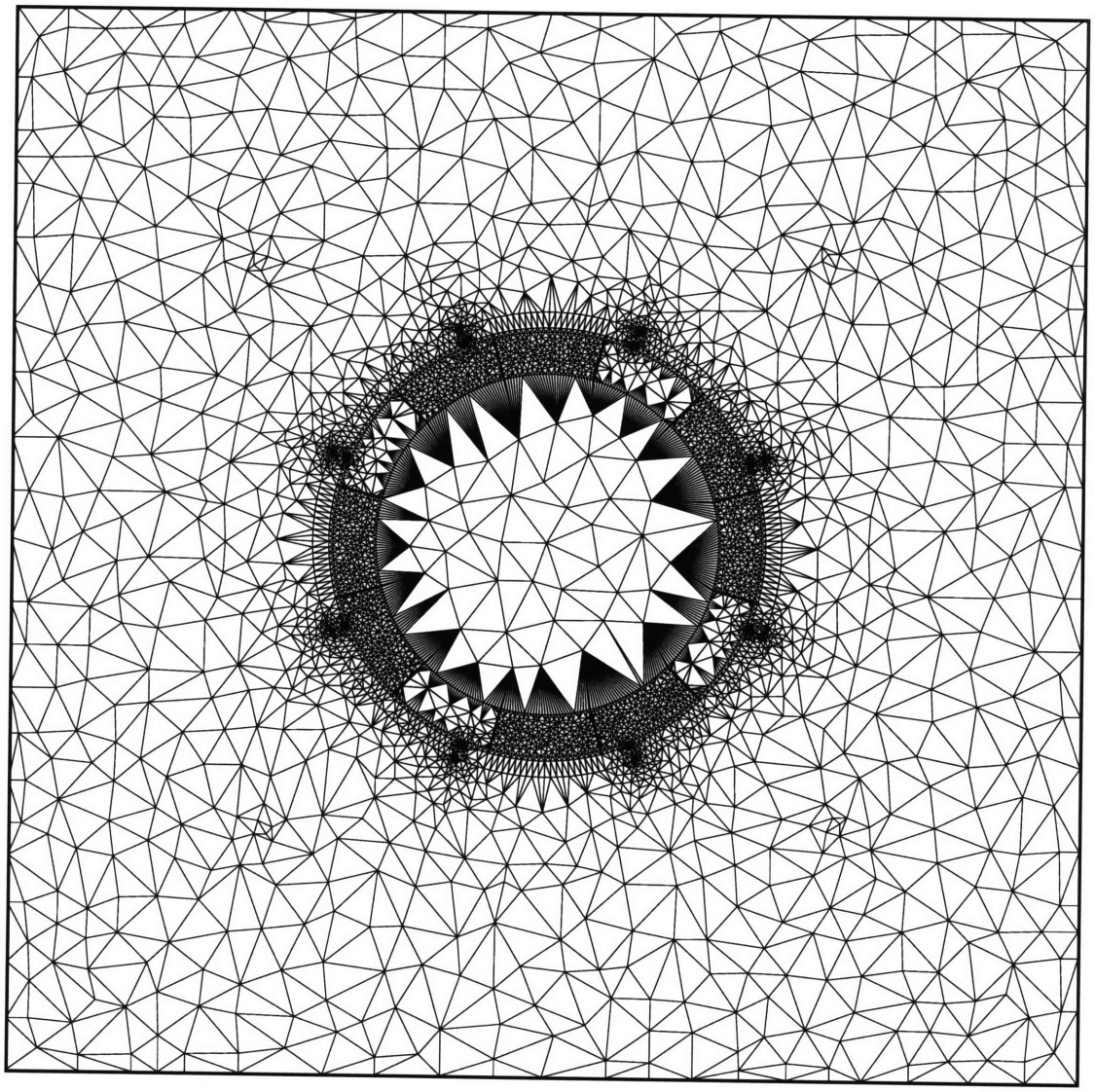

Figure 3.15: Machine *B* finite element mesh for torque analysis

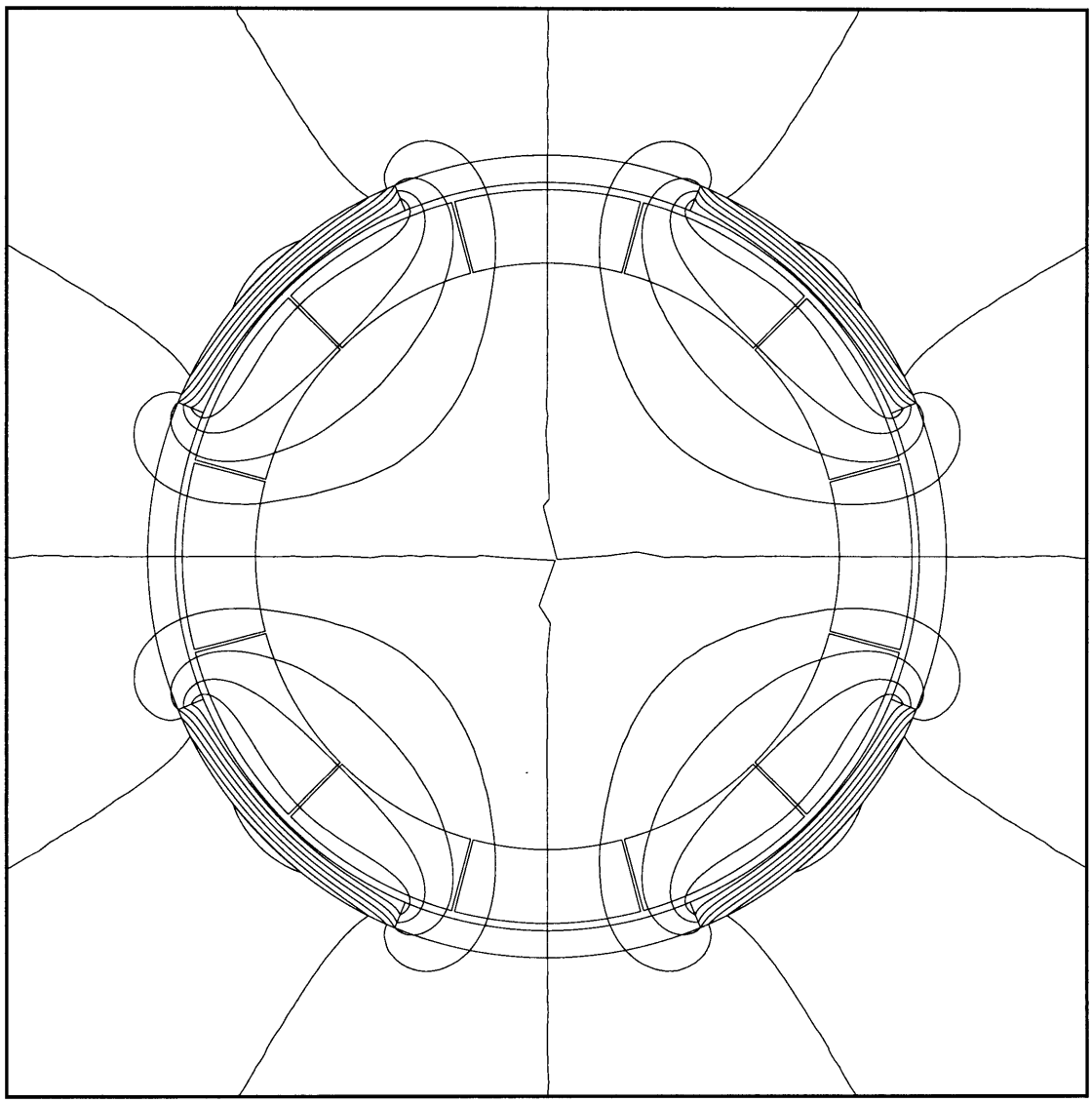

Figure 3.16: Machine *B* magnet-produced magnetic fields

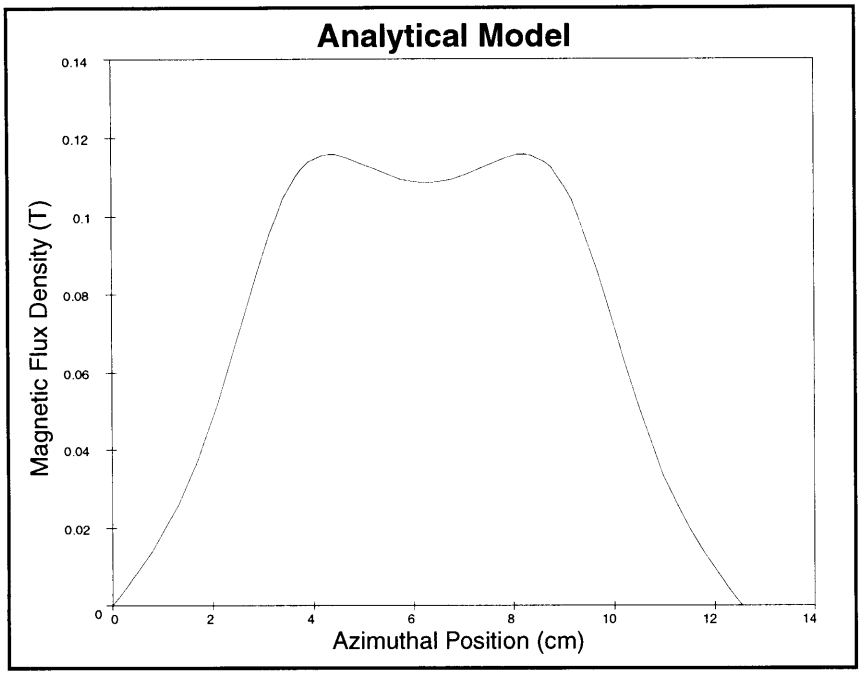

(a)

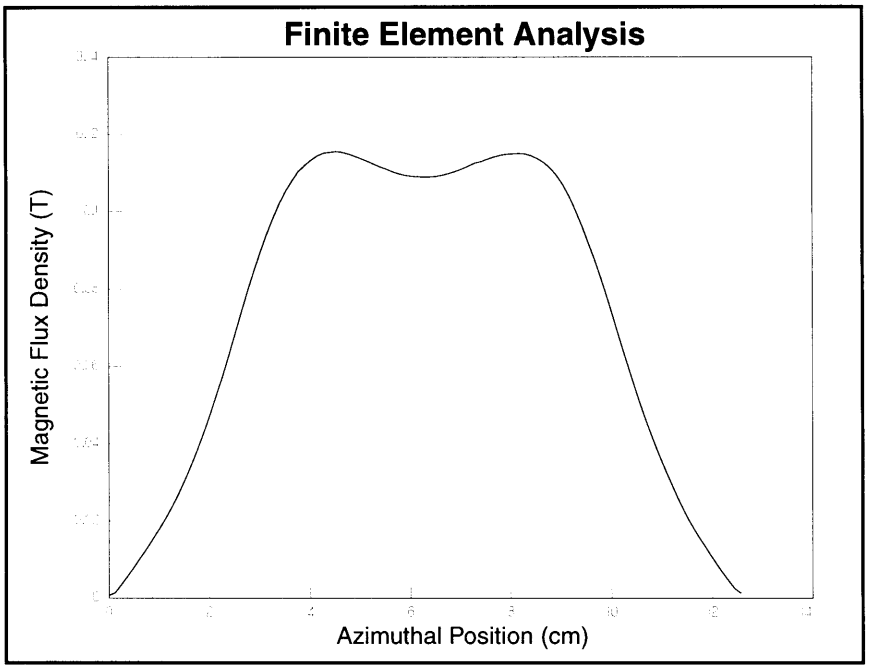

(b)

Figure 3.17: Comparison of (a) *Maple* plot of analytical model and (b) *Maxwell* finite element analysis of magnet-produced magnetic flux density at inner armature radius of Machine *B*

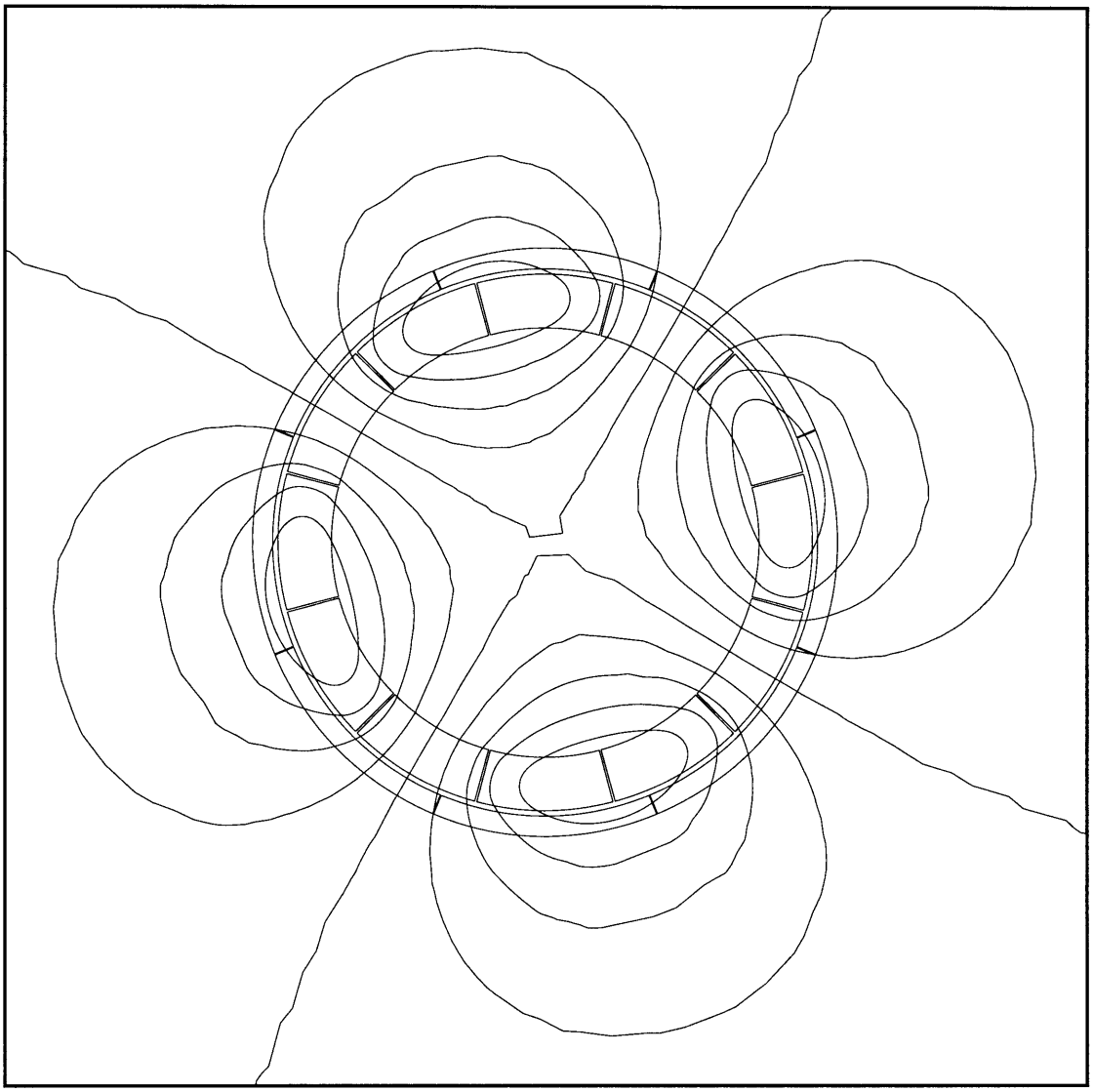

Figure 3.18: Machine *B* armature magnetic field

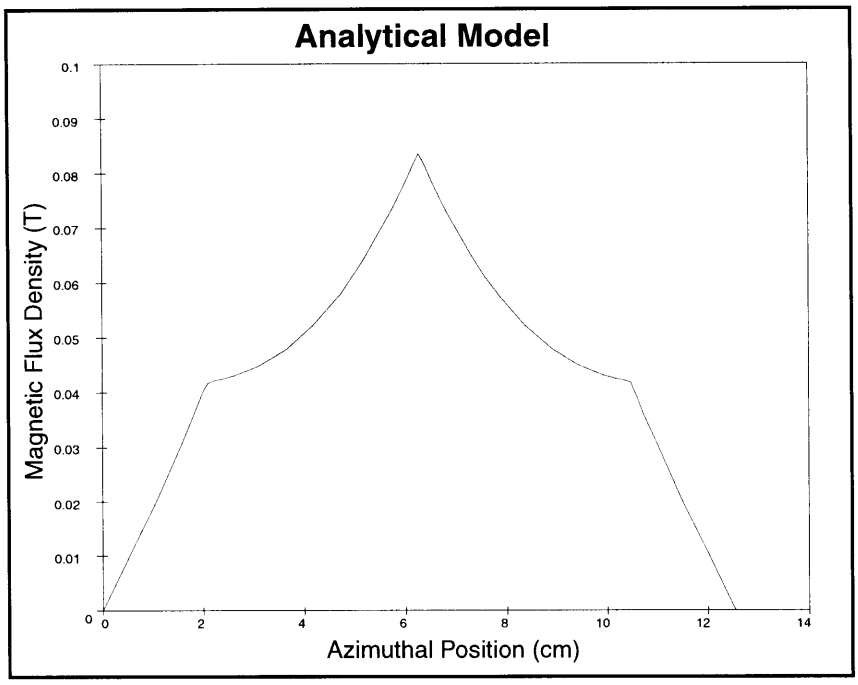

(a)

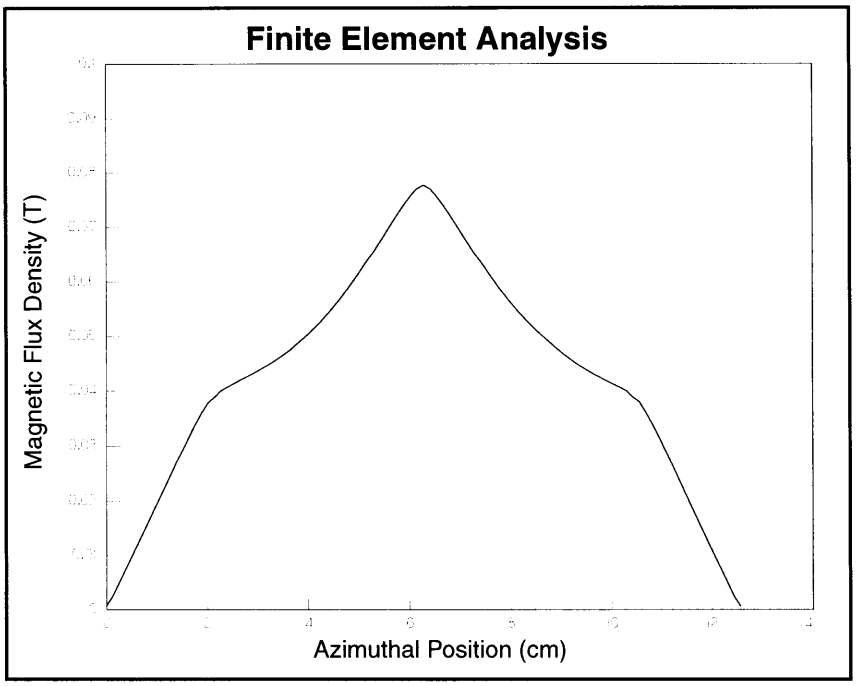

(b)

Figure 3.19: Comparison of (a) *Maple* plot of analytical model and (b) *Maxwell* finite element analysis of magnet-produced magnetic flux density at inner armature radius of Machine *B*

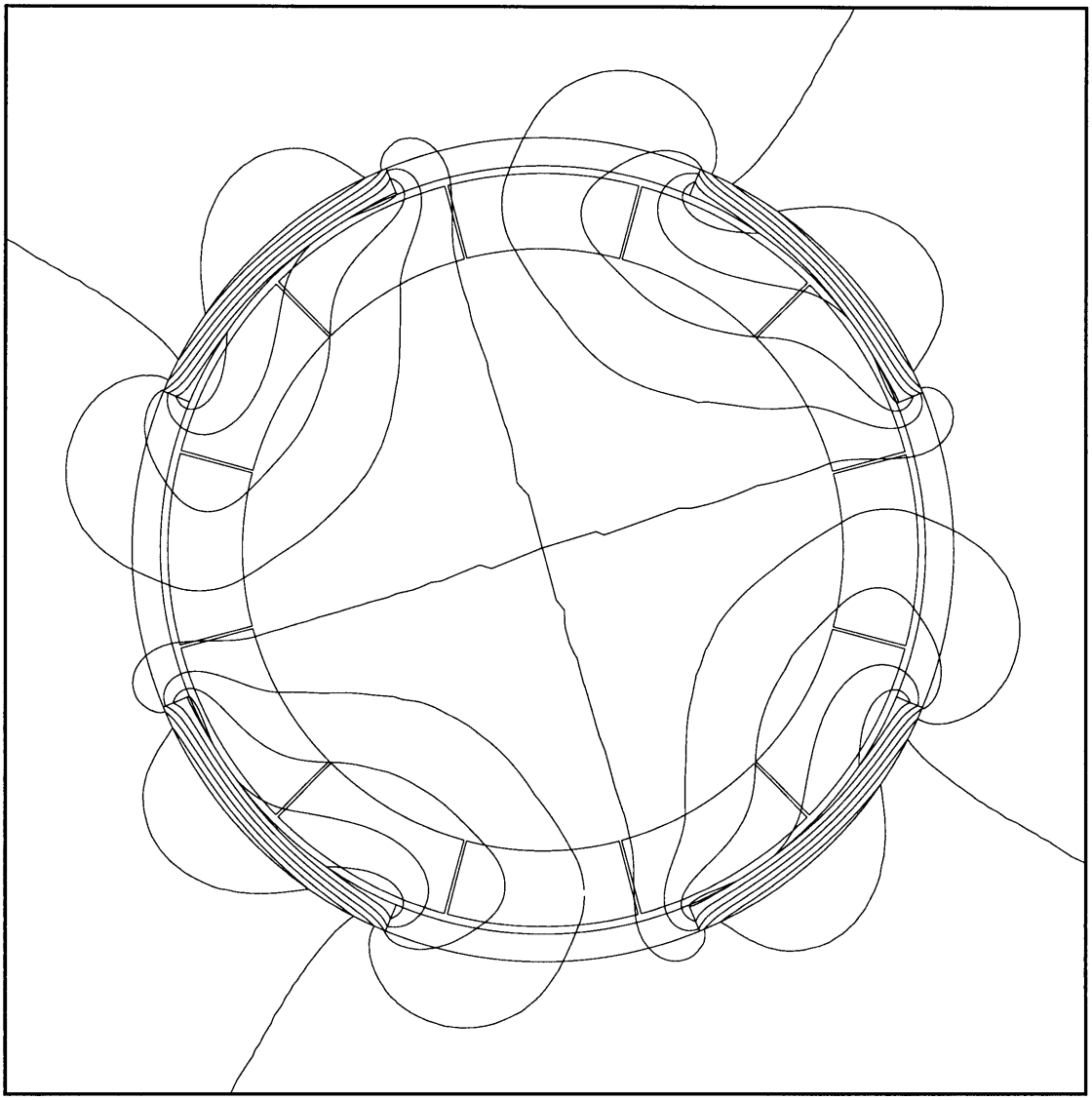

Figure 3.20: Machine *B* complete magnetic field

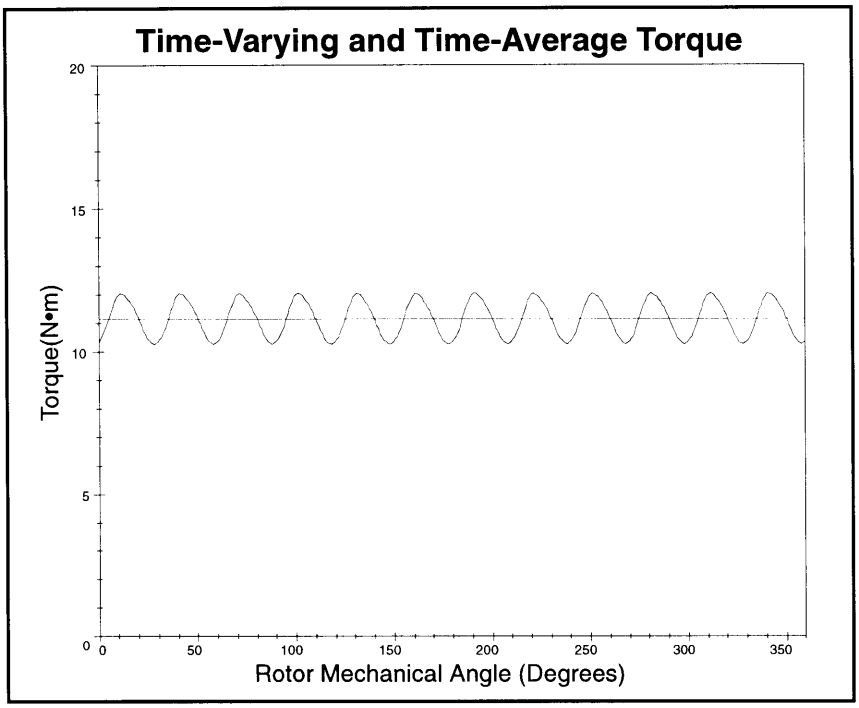

(a)

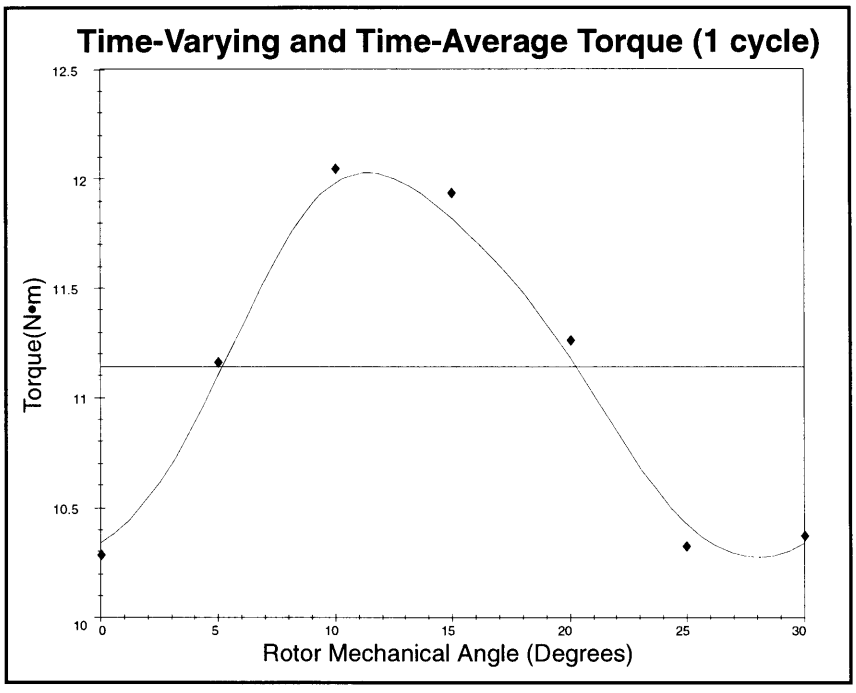

(b)

Figure 3.21: Time-varying and time-average torque of Machine *B* over (a) one full rotor rotation and (b) one cycle. The ♦ marks in plot (b) indicate FEA calculations.

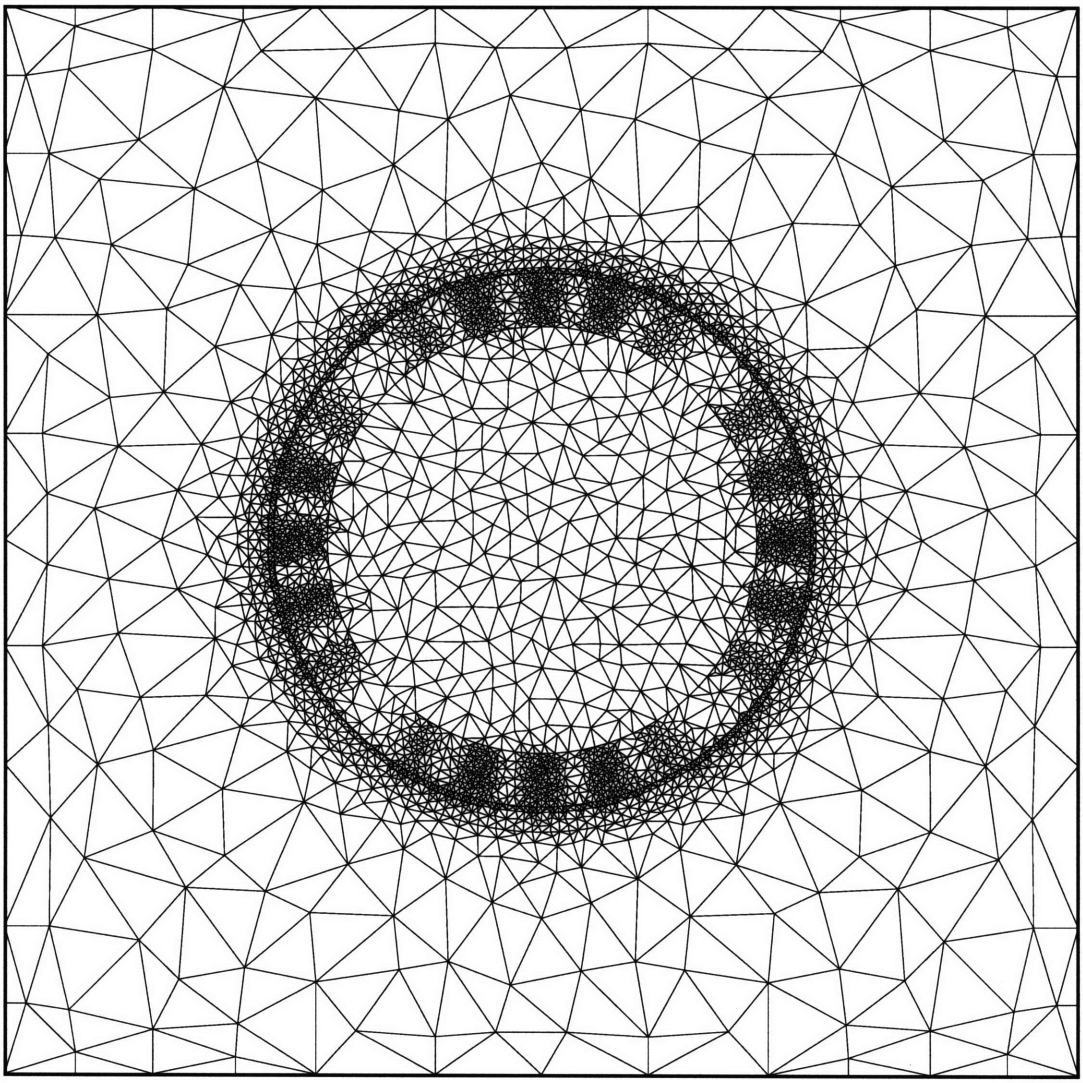

Figure 3.22: Machine *B* finite element mesh for eddy current analysis

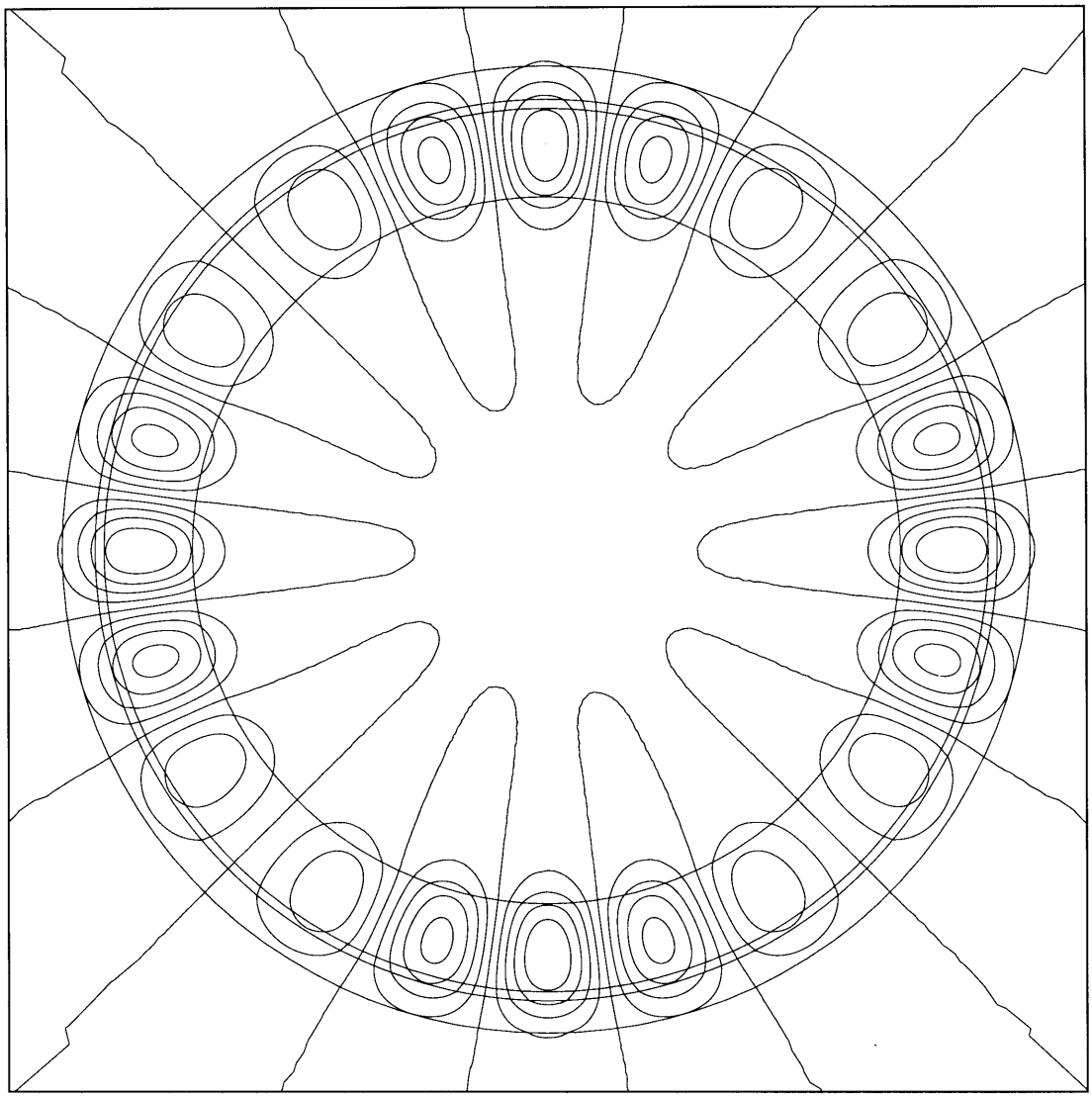

Figure 3.23: 5th and 7th harmonics of Machine *B* time-varying magnetic field

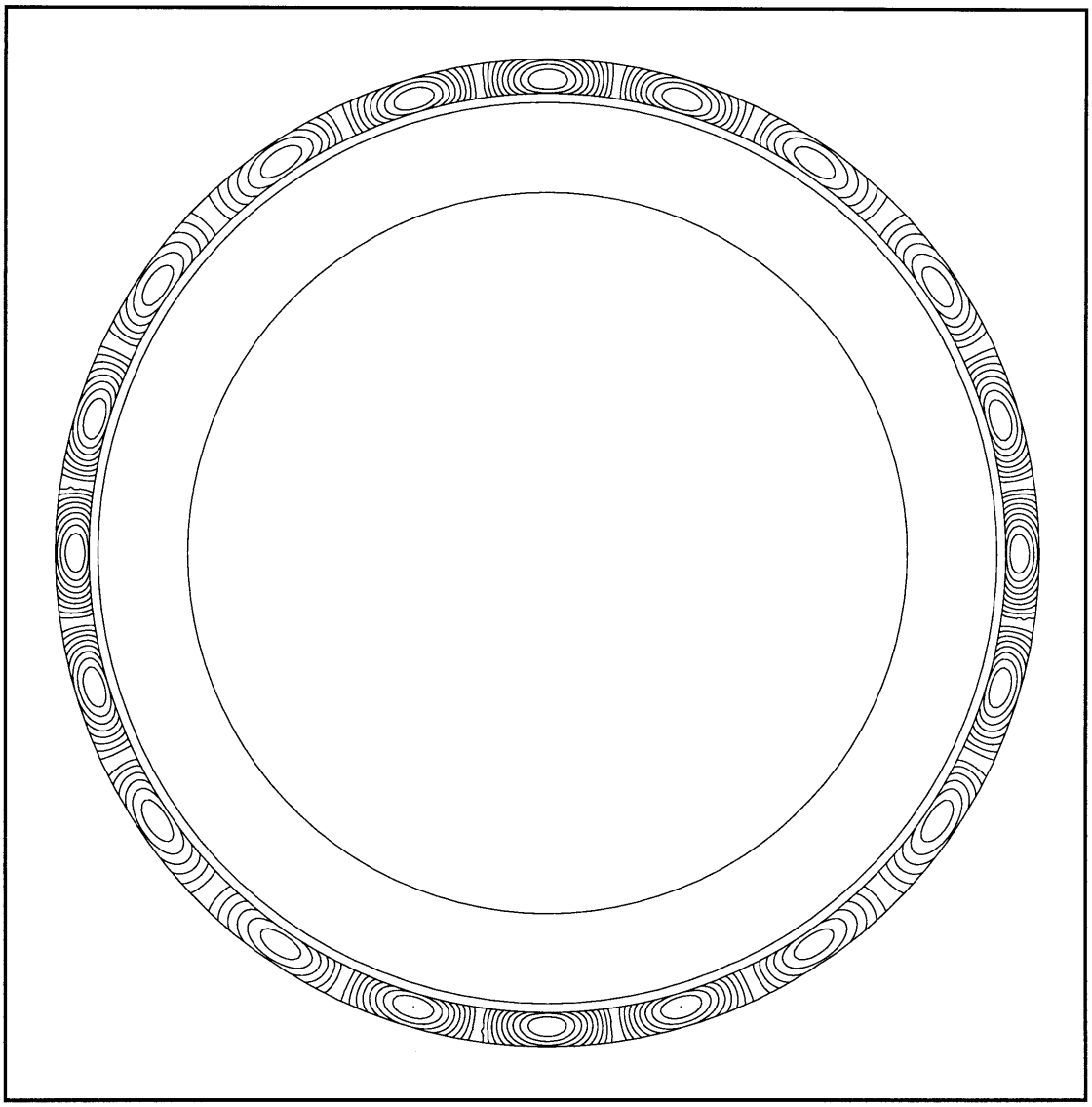

Figure 3.24: 5th and 7th harmonics of Machine *B* eddy currents

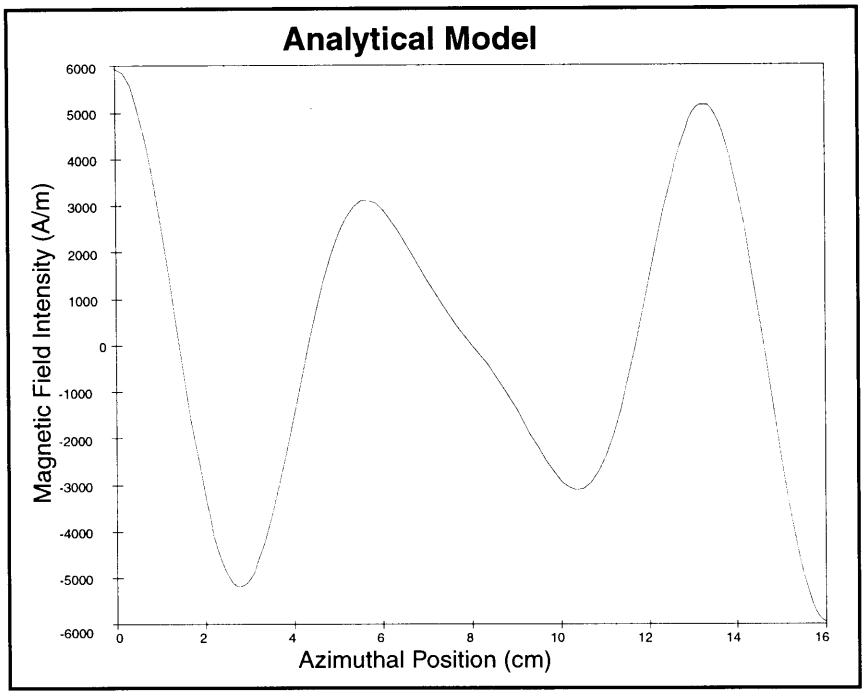

(a)

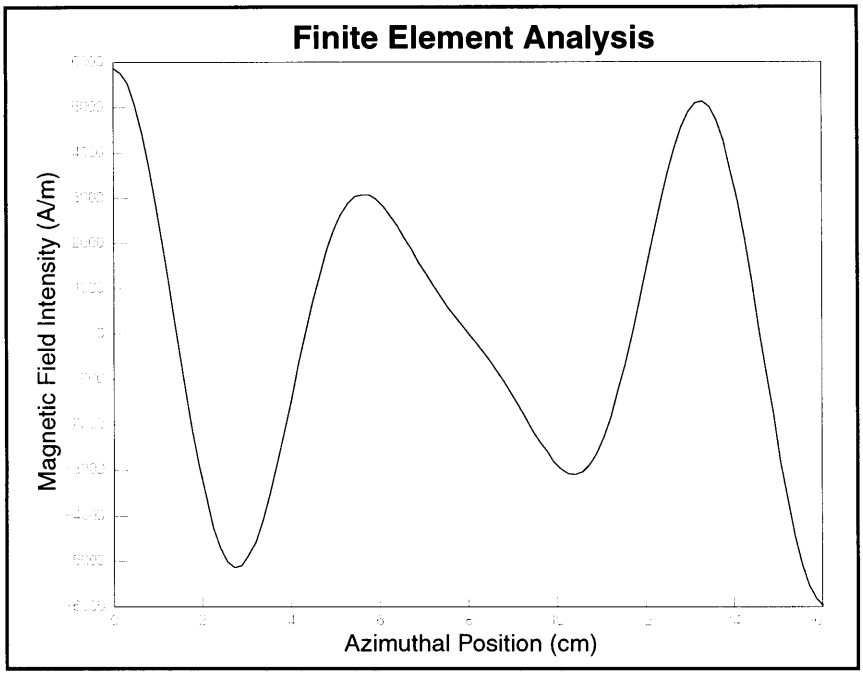

(b)

Figure 3.25: Comparison of (a) *Maple* plot of analytical model and (b) *Maxwell* finite element analysis of time-varying magnetic field intensity at inner magnet radius of Machine *B*

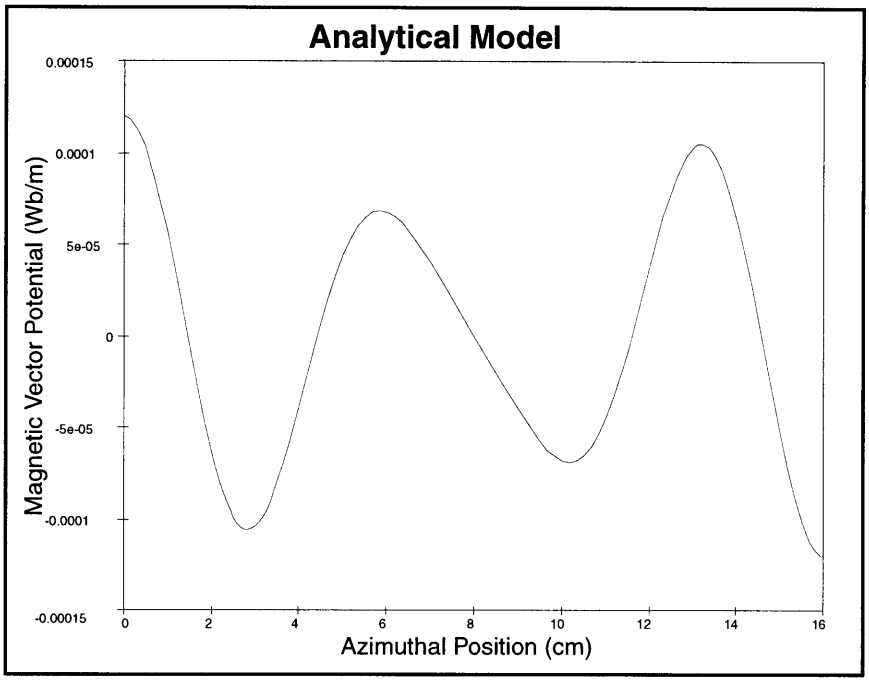

(a)

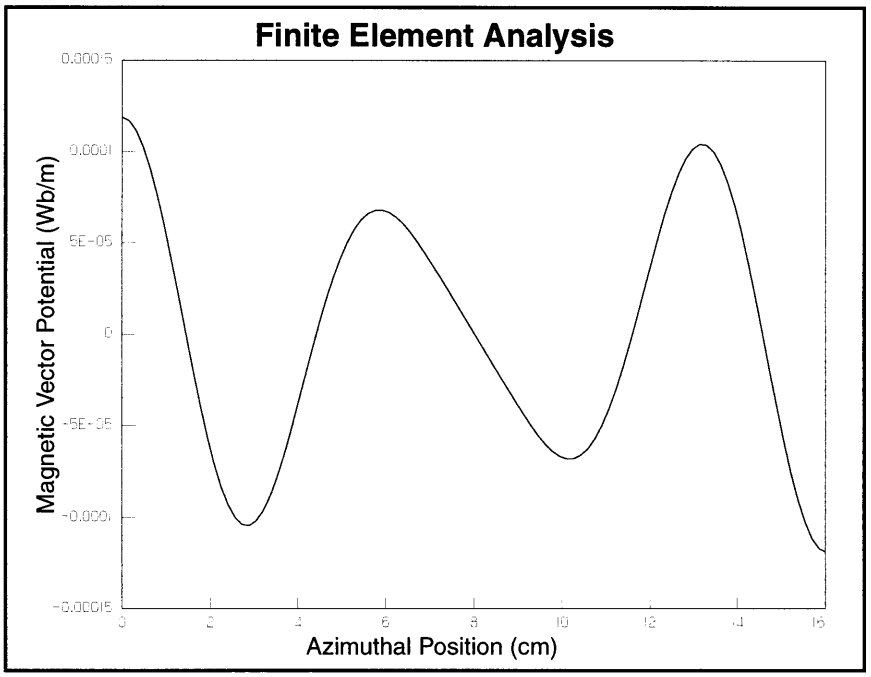

(b)

Figure 3.26: Comparison of (a) *Maple* plot of analytical model and (b) *Maxwell* finite element analysis of time-varying magnetic vector potential at inner magnet radius of Machine *B*

Chapter 4

Motor-Alternator Design Process

4.1 Overview

In this chapter, the design process for the flywheel motor-alternator is developed and executed, and the results are analyzed. An integrated, numerical design approach is used in which machines are synthesized, analyzed, and evaluated with computational methods. The approach employed is called the Novice Design Assistant and was developed by Moses [9]. It uses Monte-Carlo synthesis to generate designs, and analyzes them with the models developed in Chapter 2. The NDA saves of all of the *non-dominated designs*, valid designs that are not surpassed by another design *in all performance attributes*, creating a multi-dimensional "design frontier" of perhaps a few dozen designs. The designer can then select the design best suited for the application.

An integrated design was chosen because the various electromechanical and electromagnetic phenomena in the motor-alternator demonstrate complex interactions with each other and with the external constraints. For example, increasing the number of magnetic poles reduces end turn Ohmic losses, but increases the electrical frequency of excitation. This reduces the skin depth of the permanent magnets, but causes larger eddy currents to flow in that skin depth. The nonlinearity and complexity of the system model make it impossible to analytically maximize a performance function of the attributes.

The model complexity also precludes the use of a non-integrated design process in which the system is divided into subsystems and each subsystem is optimized independently. While this approach may simplify the design process by allowing closed-form solution of optimal parameters, it will fail to fully capture subsystem interactions and the overall design may not be optimal.

The approach taken is an integrated approach in which all aspects of performance are optimized simultaneously. This entails searching the design space, within constraints set by the designer, to find areas of optimal machine performance. While integrated design is more capable of finding optimal designs, it requires proper interaction from the designer to ensure that it converges on the optimal designs correctly. If the wrong area of the design space is searched, the optimal design cannot be found. On the other hand, if the constraints are set too broadly, excessive computation time will be exhausted evaluating poor designs. Hence, the design process must be carefully constructed to provide the proper balance between design creativity and speed of convergence.

4.2 Construction of the Integrated Design Process

The operating procedure for a general integrated design approach is illustrated by the block diagram in Fig. 4.1 Because the process must be iterated for many designs, the blocks inside the dashed box are automated with computational methods. The user is required to provided 4 sets of inputs to the design software: (1) performance requirements that the design must meet; (2) performance constraints, or ranges that the attributes must

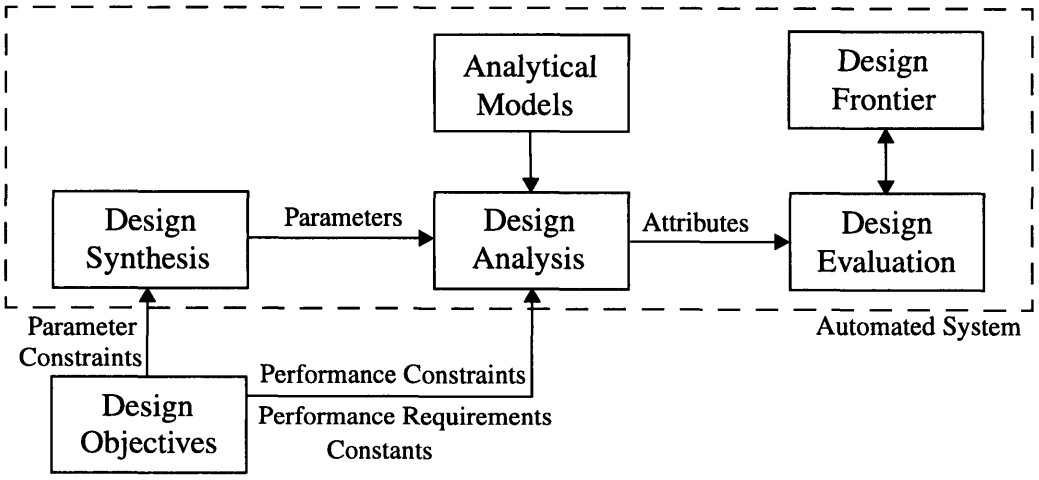

Figure 4.1: Integrated design process

be in; (3) constraints on the parameters, determined by external system limitations or designer intuition about design optimality; and (4) physical and material constants. Once the process is initialized with these inputs, it can begin the process of searching the design space.

4.2.1 Performance Requirements and Constraints

The PMSM operates in a larger system that will determine the requirements and constraints on several of the attributes and parameters. The selected values and ranges for this design were obtained by consulting with engineers familiar with EMB design issues and are summarized in Table 4.1. In this design problem, the performance requirement is a typical steady state power rating and rotational speed of a permanent-magnet synchronous machine in an HEV flywheel system.

Variable	Description	Required Value or Range
P_{mech}	Mechanical power	30 kW
ω_m	Rotational speed	3142 rad/sec (30,000 RPM)
V	Terminal voltage (line-to-neutral RMS)	≤ 155 V
J_c	Copper current density	≤ 6×10^6 A/m^2
u_m	Magnet tip speed	≤ 300 m/sec
t_m	Magnetic Radial Thickness	≤ 0.3 in (0.76 cm)
g	Air gap	1 mm
P_r	Rotor eddy current loss	< 1 W

Table 4.1: PMSM performance requirements and constraints

There are four design constraints determined by external thermal, structural, and electronic design considerations not explicitly integrated into the model:

- **Terminal voltage** The EMB is powered by the DC voltage bus of the vehicle. The

RMS line-to-neutral terminal voltage of the PMSM cannot exceed this bus voltage or it will overload the power electronics.

• **Copper current density** Too much current density in the armature wires can overheat the armature and cause machine failure. The copper current density is given by

$$J_c = \frac{J}{\lambda_a} \tag{4.1}$$

where J is the armature current density, given by Eq 2.39, and λ_a is the armature packing factor, given by Eq. C.1.

• **Magnet tip speed** The tip speed is the maximum speed of the magnets at their outer radius. In units of m/sec, this is

$$u_m = 2\pi R_s \frac{RPM_{max}}{60} \tag{4.2}$$

Excessively high speed will place undesirable stress on the permanent magnets. RPM_{max} is estimated to be 50,000 RPM for this application. Note that this effectively limits the outer radius of the machine to

$$R_s \leq \frac{(60\text{ s})(300\text{ m/s})}{2\pi(50000\text{ RPM})} = 5.73\text{ cm} \tag{4.3}$$

• **Air gap** To allow sufficient rotor clearance, the air gap must be at least 1 mm.

• **Rotor eddy current losses** As discussed in Sec. 1.3, rotor losses are constrained by radiative heat transfer out of the vacuum. A conservative upper bound on these losses was chosen to be 1 W.

If a parameter is chosen outside of the allowable range, the synthesis module discards the design. If a valid synthesized design is unable to meet the performance requirements, it is discarded during the analysis stage.

4.2.2 Selection of Independent and Dependent Variables

The number of iterations required to thoroughly search the design space is strongly dependent on the number of independent parameters. If there are N independent variables, the design space will be N-dimensional. If we consider M evenly spaced values of each parameter and systematically analyze each design, M^N iterations are required. The addition of an additional parameter increases the number of iterations needed by a factor of M. Hence, the designer should take steps to ensure that every variable chosen to be independent is constraining the system in a relevant manner.

There are several that a variable could be removed from the independent parameters, as discussed below.

• A parameter may not constrain the design performance at all. In the PMSM, the terminal voltage does not affect the machine attributes. This is because the terminal voltage of a given machine can be arbitrarily chosen by selecting the number of armature turns, as discussed in Sec 2.5.2. Furthermore, the machine losses will be independent of terminal voltage, as outlined in Sec 2.5.3. In this design the terminal voltage was required to be equal to the 155 V bus voltage. However, when the best designs are selected, they can be scaled to any desired voltage without changing their performance.

• A parameter can be constrained by the choice of another parameter. The model will have a certain number of degrees of freedom, so if too many variables are synthesized independently, the model will be overconstrained. In the PMSM design, Eq. 2.27 indicates that only 2 of the 3 parameters V_t, N_a, and N_{par} can be specified independently,

so if V_t is fixed, selecting N_a and N_{par} independently will overconstrain the system. A valid choice for an independent parameter is the *product* of N_a and N_{par}, which is the number of armature conductors N_{ac}. N_a and N_{par} will then become dependent variables in the design process.

• A parameter may be selected *a priori* based on intuition or test design runs. If a parameter value is only constrained in one direction by the model, it will tend to be as large or as small as allowed by the design. If this is the case its optimal value *is* the boundary value and it should be changed to a constant.

To test for these cases, an experimental design run was conducted with the parameter constraints set as broadly as possible. On the design frontier, the wire diameter d_w tended to be as small as is allowed, because eddy current losses go as $(d_w)^4$ according to Eq. D.8. Because of this the wire diameter was set to a reasonably small value of 0.5 mm.

Similarly, the rotor tip speed tended towards its maximum, indicating that overall performance increases with diameter. Following Eq. 4.3, the outer magnet radius R_s was then constrained to be 5.73 cm. R_s is not a parameter, but it is the sum of 4 parameters as shown in Eq. 2.1. To account for this, t_a, g, and t_m are kept as independent parameters and R_{ai} is then a dependent variable with value

$$R_{ai} = 5.73 \text{ cm} - t_a - g - t_m \tag{4.4}$$

It was also observed that bonded NeFeB magnets were not strong enough to produce viable machines without making the machine very long (30-40 cm), as compared to lengths of about 15 cm for machines with the sintered NeFeB magnets. Because the magnet eddy current losses were sustainable (about 100 mW) for sintered magnet machines, the sintered magnets were chosen as the superior material. This established the

magnet conductivity, permeability, density, and cost as constants equal to the values given in Table 2.1.

This completes the formulation of the inputs to the integrated design process, which are summarized in Table 4.2.

4.2.3 Design Synthesis

The first step in the automated design process is design synthesis, which can be done either systematically or randomly, and may be accelerated by iterative methods. Numerous methods for improving the speed of design convergence have been developed. Grid-gradient methods break up the design space into an equally spaced grid and search every point systematically, then use gradient analysis to determine the location of the optimal designs. Probability distribution function (PDF) shading [7] iteratively redefines the function specifying where in the design space the designs tend to be synthesized. These and other methods tend to accelerate the design process and allow for some measure of convergence, but their major drawback is that they require *a priori* information about design optimality. This is usually provided in a *cost function*, which assigns weightings to each attribute to give a total measure of machine performance. Hence the use of accelerators tends to be limited to design problems in which the application requirements are well understood.

The design process uses a Monte-Carlo simulation approach in which machines are randomly synthesized within a specified design space. The designer must specify the median, maximum, and minimum values of each parameter, as well as the standard deviation of the normal distribution from which the parameter is randomly chosen. This approach is termed a "novice" approach because it does not attempt to iteratively pinpoint the best designs, but merely "rolls the dice" many times over the entire design space,

	Symbol	Description	Value
Requirements	P_{mech}	Mechanical power	30 kW
	ω_m	Rotational speed	3142 rad/sec
	V	Terminal voltage	155 V
Parameters	t_a	Armature thickness	variable
	g	Air gap	variable
	t_m	Magnet thickness	variable
	L	Machine length (without end turns)	variable
	N_{ac}	Armature conductors	variable
Dependent Variables	N_a	Armature turns per phase	variable
	N_{par}	Parallel strands per turn	variable
	I	Terminal current	variable
	R_{ai}	Armature inner radius	variable
Attributes	*Eff*	Electrical efficiency	variable
	P_r	Rotor eddy current losses	variable
	C_t	Total cost	variable
	w_t	Total material weight	variable
	l_o	Machine length (including end turns)	variable
Constants	μ_0	Permeability of free space	$4\pi\times10^{-7}$ H/m
	σ_c	Copper conductivity	4.5×10^{7}
	d_w	Wire diameter	0.5 mm
	μ_c	Copper permeability	μ_0
	ρ_c	Copper density	8500 kg/m^3
	C_c	Copper cost	\$10/kg
	B_r	Magnet residual flux density	1.2 T
	σ_m	Magnet conductivity	7×10^{5} S/m
	μ_r	Magnet relative permeability	1.05
	ρ_m	Magnet density	7500 kg/m^3
	C_m	Magnet cost	\$82/kg

Table 4.2: Design process requirements, parameters, dependent variables and attributes

eliminating the need for a cost function. Computationally, this approach is less efficient than an accelerated process, but with increasing computational speed this becomes less of a limitation.

The NDA is well suited for design applications that seek to explore viability of a design concept or establish overall performance trends rather than design for a specific customer application. In this thesis, information about attribute weights, such as the relative performance of cost to weight, is not available at this time, and will require integration of the flywheel system into a larger HEV model. Before that can happen, the NDA design thus provides a vehicle for the investigation of the viability and design trends of a flywheel motor-alternator.

4.2.4 Design Analysis

If a design is generated within the parameter constraints, it is passed to the analysis module and its attributes are calculated by using the analytical expressions from Chapter 2. As noted in the previous section, machines that are unable to meet the performance requirements and constraints are flagged and eliminated from consideration. In this design, this will happen when the machine is too small to generate sufficient torque, when the copper current density is too large, or when the rotor eddy current losses are too large.

4.2.5 Design Evaluation

If a design is valid it proceeds to the evaluation stage, where it is compared against each machine on the design frontier. If it dominates one or more machines, i.e., has a higher efficiency, lower cost, lower weight and shorter total length, the dominated machines are discarded and the new machine is added to the frontier; otherwise the candidate design is discarded. This concludes one iteration, and the design process returns to the synthesis stage.

4.3 Results of the Integrated Design

With the integrated design process constructed, it was coded in *Matlab* [19] and a design run was executed with 1.5 million iterations. This was chosen because it took only a few hours and because only 2 or 3 machines tended to be added to the design frontier between 1 and 1.5 million iterations. A design frontier of 50 machines was generated and the results are presented in Fig. 4.3.

4.3.1 Selection of the Optimal Design

Although a cost function is not available for this application, some evaluation of performance was needed to pick designs that tended to perform best. The method chosen is to evaluate each machine attribute by calculating its deviation from the mean for the entire frontier. Each machine is then assigned a "performance score" equal to the average number of standard deviations above or below the mean for each of the 4 attributes. Fig. 4.3 is sorted according to this performance score.

The overall "best" design is summarized in Table 4.4. Note that the top five machines have similar attributes, indicating there is a single region of performance maxima around 6 pole pairs for this cost function. In a more thorough design process, the process could be rerun with parameter constraints tightened around the mean of the first few optimal machines. This will search the neighborhood of best designs to pinpoint the absolute peak performance of the machine.

4.3.2 Design Trends

The key results of the design are as follows.

• Rotor losses for the optimal machine are on the order of 100 mW, well below the conservative maximum of 1 W. This establishes the viability of the PMSM for use in this application and is the key result of the thesis. Furthermore, none of the top 20 machines has an eddy current loss exceeding 350 mW. This indicates that, if loss capacity estimates

	p	Na	Npar	Rai	ta	g	tm	L	P_m	length	pack	eff	weight	cost	rank:				
Rank	(pairs)	(turns)	(strands)	(cm)	(cm)	(cm)	(cm)	(cm)	(mW)	(cm)	(%)	(%)	(kg)	($)	eff	weight	cost	length	score
1	6	33	55	4.090	1.144	0.105	0.390	10.62	112.40	14.11	81.88	96.06	3.753	199.60	33	17	14	5	0.583
2	5	25	56	4.127	0.961	0.108	0.533	10.45	154.90	13.81	75.71	96.61	3.497	250.20	27	10	35	4	0.552
3	5	26	57	4.020	1.049	0.120	0.540	10.35	128.50	13.49	73.98	96.57	3.578	251.50	28	12	36	3	0.534
4	6	31	56	4.051	1.115	0.142	0.421	10.77	68.77	14.14	81.31	96.05	3.740	214.20	34	16	20	6	0.509
5	7	28	56	4.380	0.870	0.103	0.376	10.77	75.72	14.93	88.76	95.08	3.456	193.10	40	8	9	9	0.499
6	6	24	55	4.418	0.794	0.101	0.417	11.69	129.00	15.38	82.62	96.00	3.378	223.80	35	6	24	11	0.488
7	4	32	55	3.912	1.117	0.113	0.587	8.75	331.90	14.32	84.59	97.30	3.985	237.10	21	20	31	7	0.482
8	7	23	56	4.494	0.748	0.104	0.384	12.01	73.97	15.56	85.15	95.07	3.266	213.30	41	4	19	13	0.415
9	7	23	56	4.333	0.778	0.105	0.513	9.96	49.09	13.30	84.40	93.81	3.093	228.80	49	2	28	2	0.406
10	8	26	55	4.453	0.827	0.103	0.347	11.90	44.57	14.97	84.88	94.09	3.277	195.00	48	5	11	10	0.394
11	7	26	56	4.419	0.803	0.115	0.393	10.94	64.76	15.55	90.53	94.97	3.431	202.50	43	7	15	12	0.385
12	6	24	54	4.463	0.785	0.112	0.369	13.05	131.70	16.67	81.86	96.36	3.500	223.80	30	11	23	21	0.378
13	6	26	54	4.444	0.773	0.117	0.397	11.41	127.90	16.69	90.19	96.09	3.579	212.70	31	13	18	24	0.354
14	6	32	55	4.253	1.016	0.124	0.337	11.84	121.90	16.32	87.37	96.45	4.000	196.80	29	21	12	17	0.353
15	5	23	55	4.405	0.786	0.107	0.432	12.58	242.80	16.62	80.13	97.07	3.618	248.00	24	14	34	19	0.329
16	6	24	57	4.400	0.760	0.106	0.463	10.75	113.20	15.69	89.19	95.49	3.493	228.20	38	9	27	14	0.302
17	8	25	55	4.250	0.851	0.107	0.520	9.51	24.60	12.24	82.94	92.07	3.018	221.60	50	1	22	1	0.279
18	5	28	56	4.168	1.107	0.102	0.353	13.64	246.90	16.73	72.18	97.32	4.041	229.40	20	24	29	25	0.278
19	7	20	56	4.612	0.623	0.106	0.388	12.84	79.50	16.68	86.66	94.98	3.214	227.20	42	3	26	23	0.247
20	6	33	57	4.084	1.232	0.110	0.303	13.36	130.80	16.33	76.91	96.62	4.270	202.60	26	30	16	18	0.238
21	5	40	56	3.875	1.412	0.110	0.332	11.50	257.80	15.81	83.14	97.08	4.698	197.00	23	41	13	15	0.212
22	4	30	56	4.143	1.041	0.102	0.443	11.36	522.40	16.67	82.29	97.70	4.269	238.80	16	28	32	22	0.203
23	8	26	55	4.536	0.781	0.127	0.286	13.95	42.63	17.75	89.11	94.91	3.628	193.80	44	15	10	31	0.132
24	7	31	58	4.295	1.069	0.105	0.260	14.54	92.55	17.75	82.93	96.07	4.272	192.10	32	31	7	32	0.066
25	9	33	55	4.351	1.028	0.101	0.250	13.62	36.64	16.66	87.36	94.14	3.971	174.50	47	19	1	20	0.058
Avg	**5.50**	**27.52**	**56.02**	**4.248**	**0.967**	**0.118**	**0.397**	**13.22**	**330.98**	**17.48**	**81.46**	**96.57**	**4.125**	**238.24**					
StDev	**1.89**	**4.48**	**1.05**	**0.253**	**0.195**	**0.017**	**0.121**	**2.53**	**312.65**	**2.69**	**6.58**	**1.48**	**0.593**	**48.69**					

Table 4.3: PMSM design frontier ranked by performance (machines 1-26)

	p	Na	Npar	Rai	ta	g	tm	L	P_m	length	pack	eff	weight	cost	rank:				
Rank	(pairs)	(turns)	(strands)	(cm)	(cm)	(cm)	(cm)	(cm)	(mW)	(cm)	(%)	(%)	(kg)	($)	eff	weight	cost	length	score
26	4	35	55	4.011	1.190	0.133	0.396	11.62	461.70	17.21	83.96	97.66	4.682	226.70	17	40	25	27	0.034
27	4	31	57	4.079	1.134	0.130	0.386	12.85	466.20	17.66	79.63	97.82	4.596	239.90	15	38	33	30	-0.012
28	6	32	56	4.389	0.970	0.104	0.266	13.72	205.00	19.33	91.03	96.81	4.486	188.90	25	35	6	38	-0.030
29	3	30	55	3.841	1.212	0.113	0.564	11.27	874.60	16.18	72.58	98.15	4.575	290.30	8	37	40	16	-0.069
30	4	28	57	4.126	1.100	0.118	0.386	14.02	476.40	18.00	73.52	97.88	4.482	256.50	14	34	38	33	-0.071
31	3	25	55	3.717	1.147	0.123	0.743	10.65	511.70	14.70	66.93	98.02	4.269	342.30	11	29	49	8	-0.091
32	8	30	55	4.439	0.969	0.109	0.212	16.85	63.36	19.70	82.70	95.73	4.262	184.90	36	27	4	40	-0.132
33	4	21	55	4.442	0.742	0.103	0.442	14.57	582.40	19.23	77.69	97.95	4.022	290.80	13	23	41	37	-0.155
34	3	32	57	3.821	1.265	0.120	0.524	11.16	948.20	16.86	77.37	98.15	4.851	274.60	9	45	39	26	-0.168
35	8	25	55	4.652	0.741	0.115	0.221	17.41	65.62	21.17	88.55	95.56	3.965	192.40	37	18	8	45	-0.210
36	5	36	57	4.140	1.200	0.120	0.270	14.28	317.50	19.19	85.48	97.36	5.081	203.30	19	48	17	36	-0.249
37	3	23	56	4.099	0.869	0.118	0.643	11.69	872.90	17.62	78.05	98.27	4.374	331.10	4	33	48	29	-0.307
38	9	25	58	4.615	0.801	0.105	0.208	17.82	42.65	20.86	86.63	94.79	4.045	188.10	45	25	5	43	-0.324
39	3	28	56	3.828	1.269	0.126	0.507	13.27	830.90	17.41	66.27	98.25	4.764	308.10	6	43	44	28	-0.337
40	9	28	56	4.590	0.799	0.121	0.219	15.79	35.67	20.76	94.37	94.64	4.185	179.40	46	26	2	42	-0.354
41	3	26	56	4.062	0.977	0.133	0.557	12.21	929.50	18.30	78.76	98.27	4.620	308.20	5	39	45	34	-0.356
42	6	20	57	4.726	0.636	0.110	0.257	19.08	224.40	23.33	84.92	97.12	4.012	234.40	22	22	30	49	-0.383
43	4	27	58	4.311	0.990	0.110	0.319	16.36	681.80	21.15	78.56	98.01	4.849	253.80	12	44	37	44	-0.482
44	9	29	58	4.533	0.891	0.116	0.190	17.80	40.34	21.46	90.33	95.13	4.537	180.40	39	36	3	46	-0.490
45	3	25	57	3.985	1.112	0.127	0.506	14.17	887.30	18.44	66.86	98.35	4.749	324.90	2	42	47	35	-0.496
46	5	32	55	4.250	1.090	0.144	0.245	17.57	273.90	21.56	79.82	97.48	5.071	221.50	18	47	21	47	-0.538
47	4	19	56	4.587	0.659	0.106	0.377	17.80	723.20	22.73	78.71	98.12	4.285	305.60	10	32	43	48	-0.639
48	3	31	57	3.808	1.333	0.169	0.420	14.76	838.50	19.45	70.75	98.21	5.352	295.30	7	50	42	39	-0.716
49	3	26	58	4.051	1.045	0.171	0.463	14.93	859.10	20.33	74.87	98.33	5.095	319.50	3	49	46	41	-0.793
50	3	20	57	4.327	0.737	0.177	0.488	17.17	931.50	23.43	78.63	98.45	5.003	375.30	1	46	50	50	-1.309
Avg	**5.50**	**27.52**	**56.02**	**4.248**	**0.967**	**0.118**	**0.397**	**13.22**	**330.98**	**17.48**	**81.46**	**96.57**	**4.125**	**238.24**					
StDev	**1.89**	**4.48**	**1.05**	**0.253**	**0.195**	**0.017**	**0.121**	**2.53**	**312.65**	**2.69**	**6.58**	**1.48**	**0.593**	**48.69**					

Table 4.3: PMSM design frontier ranked by performance (machines 26-50)

Characteristic	Value	Attribute	Value
mechanical power	30 kW	electrical efficiency	96.1%
rotational speed	30000 RPM	material cost	$199.60
magnet material	sintered NdFeB	material weight	3.75 kg
pole pairs	6	total length	14.1 cm
armature turns	33	P_a (eddy)	930 W
parallel strands	55	P_a (Ohmic)	252 W
armature inner radius	4.09 cm	P_r^{2D}	116.9 mW
armature thickness	1.14 cm	P_r^{3D}	112.8 mW
air gap	1.05 mm		
magnet thickness	3.90 mm		
armature length	10.62 cm		
terminal current	64.6 A		
terminal voltage	155 V		

Table 4.4: Characteristics and attributes of the optimal PMSM

are accurate, the eddy current losses do not constrain a machine that is maximized for the other 4 attributes.

• The optimal five machines have between 5 and 7 pole pairs. This was a key result of the integrated design because no parameter has as varied an effect on machine attributes and could be as hard to intuitively predict as pole pairs. Consider that increasing the pole pairs tends to decrease the efficiency because armature eddy current losses increase, but also tends to decrease the weight, cost, and length of the machine. For each of these 3 attributes, the best machines have between 7 and 9 pole pairs. This can be explained by considering the fact that the Halbach array produces more sinusoidal flux as the number as the number of poles increases, which can be seen by comparing Figs. 3.4 and 3.17 (see also [14] for Halbach's theoretical treatment). However, the flux linked by the armature

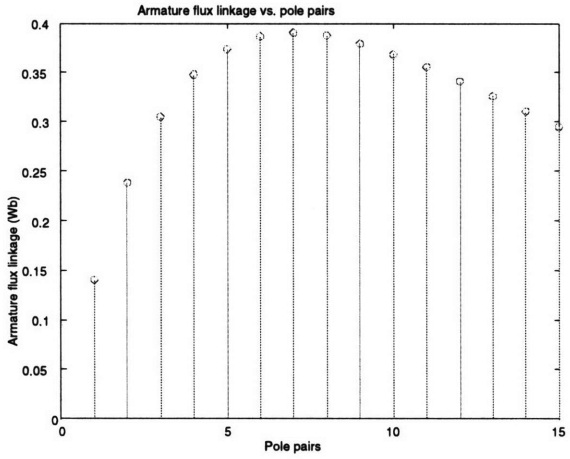

Figure 4.2: Armature flux linkage

decreases as the number of poles increases, because the flux wavelength falls. Hence, the maximum flux linked will occur at an intermediate number of pole pairs. Fig.4.2 plots total armature flux linked versus the number of pole pairs for a typical geometry and demonstrates that the flux linkage is maximized at around 7 or 8 pole pairs. The optimal machine, with 6 pole pairs, then represents a balance between efficiency and low weight and cost.

• The highest efficiency achieved is 98.5% for a 3-pole pair machine. This machine is the costliest and longest machine in the design frontier, however. This reflects the inherent tradeoff between weight/cost and efficiency, as illustrated in Fig. 4.3. This confirms intuition that the most efficient machine will tend to have few poles to reduce eddy current losses, and a relatively low resistance rotor. This is achieved by using a very thick magnet and a very long machine to create the maximum magnet flux. Then fewer armature turns are required, reducing armature resistance.

• The lightest machine is a 3.0 kg, 7-pole pair machine. This also makes sense because the machine with maximum flux linkage will tend to require the least amount of materials

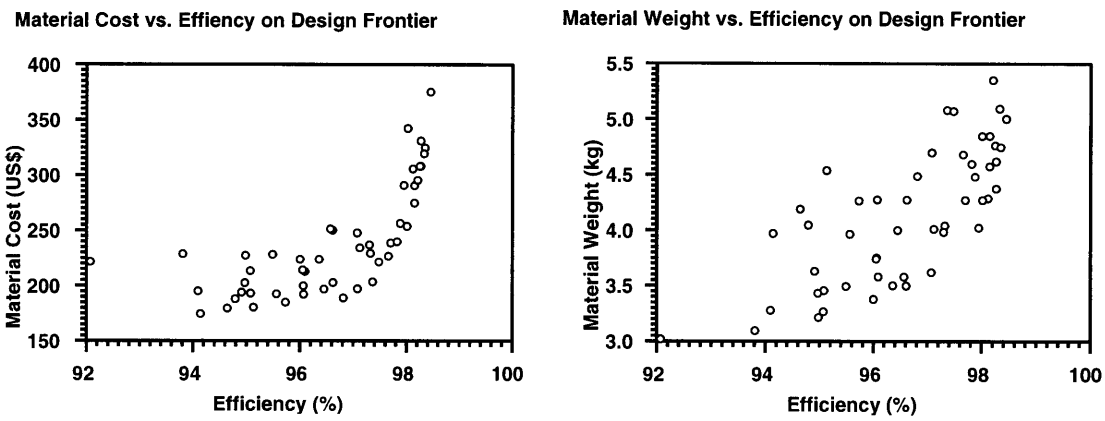

Figure 4.3: Weight/cost vs. efficiency tradeoff

to produce rated torque. Similarly, the least expensive machine, at $174.50, and also the shortest machine, at 12.24 cm, has the most pole pairs at 9.

4.3.3 Summary

Taken collectively, the results of the integrated design tend to closely match engineering intuition. This, coupled with the FEA analysis in Chapter 3, verifies the validity of the analytical models. This design process has not produced the "best" overall machine, but it provides insight into the various tradeoffs that the electromagnetic system presents. It also indicates that eddy current losses on the rotor, a key concern for flywheel development, can be contained for high performance motor-alternators. Hence the results can provide intuition to the designers of other HEV subsystems that interact with the flywheel energy storage system.

Chapter 5

Summary, Conclusion and Suggestions for Future Research

5.1 Summary of Thesis Results

This predominate goal of this thesis has been the analysis and characterization of eddy current losses arising on the rotor of a high-speed permanent-magnet synchronous machines. Because the rotor of the machine is housed in a vacuum, heat transfer is severely limited, and keeping these losses to a sustainable level of less than 1 W represents a key design challenge in this application. Chapter 2 develops analytical models for the relevant electromagnetic and electromechanical phenomena in this machine, including electromagnetic torque, stator losses, and two- and three-dimensional rotor eddy current losses. In Chapter 3, the torque and 2D rotor eddy current loss models are tested against computational finite element analysis. In Chapter 4, an integrated, computational Monte-Carlo design process is constructed and used to develop a design frontier of machines best suited for this application.

The key results of the thesis are presented below.

- The design results demonstrate that for high-performance machines, rotor eddy current losses are on the order of 100 mW in the steady state, well below the conservative maximum sustainable value of 1 W. This confirms the viability of 30 kW, 30,000 RPM PMSMs in flywheel energy storage applications. This represents the key contribution of this thesis toward the ongoing research into the development of flywheel motor-alternators.

- Analytical torque and 2D rotor loss models are developed analytically and

successfully verified with the Ansoft *Maxwell* finite element analysis package. Computed values of torque and rotor power dissipation agrees with analytical results to within about 1%.

• The 3D eddy current loss model contributes original analysis to the nature of eddy currents flowing in an axially-limited machine and is integrated into the design process. However, this model has not been tested with finite element analysis software.

• Optimal machines designs confirm intuition about fundamental tradeoffs and design trends inherent in these types of machines. In particular, the most important tradeoff is low cost/weight versus electrical efficiency. The design process also indicates that optimal machines tend toward 5 to 7 pole pairs. This reflects a fundamental tradeoff between electrical efficiency, which is high for machines with between 3 and 5 pole pairs; and cost, weight, and machine length, which tend to be a minimum for machines with between 7 and 9 pole pairs. This result demonstrates the ability of the integrated design approach to balance the effect of a parameter on interrelated, highly complex subsystems.

To summarize, this thesis has established the potential viability of PMSMs in the EMB application, and has contributed relevant models and design trends that can be considered by engineers developing a larger integrated energy storage system.

5.2 Suggestions for Future Research

This thesis represents just a start toward a thorough and interdisciplinary characterization of the motor-alternator behavior. Suggestions for future investigation are given below.

• The integrated design approach should be broadened to include other PMSM

configurations. Specifically, slotted machines with back iron have higher air-gap flux and could demonstrate higher performance in this application.

• The analytical models should be integrated into a larger EMB system including the power electronics. This will have two predominate effects on motor-alternator design. First, increasing the number of pole pairs increases the electrical frequency of armature waveforms supplied by the power electronics. This will require higher switching frequencies in the electronics, producing higher losses and lowering the overall system electrical efficiency. Second, power electronics are unable to supply waveforms that are perfectly sinusoidal in time, as this thesis assumes. Actual systems use inverters to fit step waves to sinusoids, producing time harmonics. These will in turn affect the higher-order field harmonics seen by the magnets and will increase eddy current losses. A thorough analysis of these effects is warranted.

• A finite element analysis should be performed to verify the validity of the 3D eddy current model. This could be performed with a 2D package following the surface impedance model constructed in Appendix F, but a thorough analysis would require use of 3D FEA software such as the Ansoft 3D package [20].

• A thorough model of the heat transfer characteristics of the system should be developed to gain a more precise estimate of maximum allowable power loss in the rotor.

• Structural analysis of the effect of high-speed rotation on the optimal motor-alternators should be performed.

• A model of the dynamic effects of flywheel charging and discharging is needed to determine the maximum amount of heat generated and the maximum temperature of the rotor. A power demand cycle such as a standard urban or highway driving cycle could be

used as an input to this system.

• The behavior of the motor-alternator under terminal fault conditions should also be studied. In particular, the field intensity should be assessed to determine if it will demagnetize the permanent magnets and destroy the machine.

When this work is carried out, a complete assessment can be made of the viability of permanent-magnet synchronous motor-alternators in hybrid electrical vehicle flywheel energy storage systems.

Appendix A

Air Gap Armature Self-Inductance

As discussed in Sec. 2.5.1, the armature winding affects the behavior of the permanent-magnet synchronous machine in two ways. The first is its linkage of the magnetic flux produced by the magnets, which is characterized by the winding factor k_w in the expression for back emf. The second is the armature linkage of its own magnetic field, giving rise to the synchronous armature self-inductance L_d. This appendix derives analytical expressions for k_w and L_d.

A.1 Armature Winding Factor

In this section a winding factor, relating the geometry of the armature winding to the flux linked by it, is derived. The winding factor is the ratio of the flux linked by a distributed winding to that linked by full-pitched coil. Consider an armature where the turns in each phase belt are distributed along an arc of the stator circumference spanning a mechanical angle θ_{wm}, as shown for a two-pole polyphase machine in Fig. A.1. If there are q phases in the machine, this angle is

$$\theta_{wm} = \frac{2\pi}{(2q)p} = \frac{\pi}{qp} \tag{A.1}$$

Now consider a single coil in this winding, offset from a diameter by a mechanical angle ϕ, represented by the solid line in Fig. A.1. If the radial magnetic flux at the armature radius R is the n^{th} harmonic term

$$B_{rn} = B\sin(np\theta) \tag{A.2}$$

then the flux linked by the single coil is given by

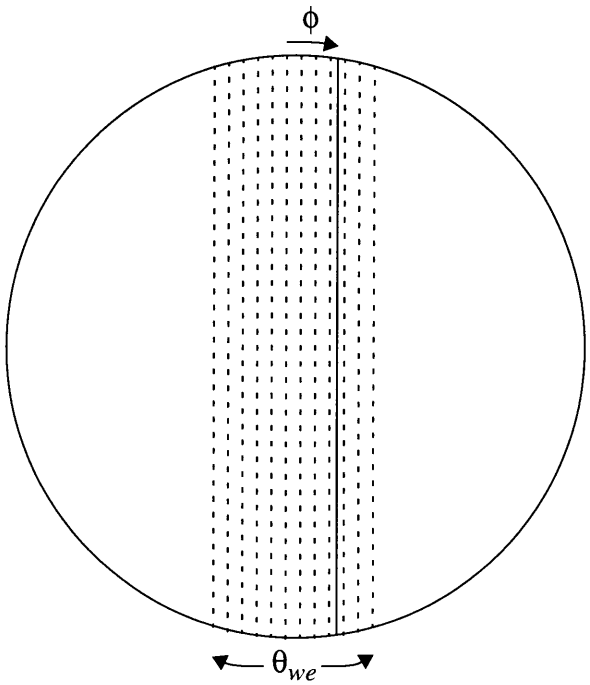

Figure A.1: Distributed armature winding

$$\lambda_{sn} = \int_{\phi}^{\pi-\phi} B\sin(np\theta)Rd\theta = \frac{2BR\cos(np\phi)}{np} \tag{A.3}$$

Note that a single full-pitched coil ($\phi = 0$) links flux

$$\lambda_{fn} = \frac{2BR}{np} \tag{A.4}$$

λ_{sn} can be integrated and averaged over the entire winding to give the average flux linked by each winding in the distributed armature

$$\lambda_{dn} = \frac{1}{\theta_{wm}} \int_{-\frac{\theta_{wm}}{2}}^{\frac{\theta_{wm}}{2}} \lambda_{sn} d\phi = \frac{1}{\theta_{wm}} \int_{-\frac{\pi}{2qp}}^{\frac{\pi}{2qp}} \frac{2BR\cos(np\phi)}{np} d\phi = \frac{4qBR}{n^2 p\pi} \sin\left(\frac{n\pi}{2q}\right) \tag{A.5}$$

Now we can define an armature winding factor k_{wn} that is the ratio of the average flux

linked by the distributed winding to the flux linked by a single full pitched coil:

$$k_{wn} = \frac{\lambda_{dn}}{\lambda_{fn}} = \frac{\sin\left(\frac{n\pi}{2q}\right)}{\frac{n\pi}{2q}} \tag{A.6}$$

The fundamental winding coefficient

$$k_w = \left.\frac{\sin\left(\frac{n\pi}{2q}\right)}{\frac{n\pi}{2q}}\right|_{n=1} = \frac{\sin\left(\frac{\pi}{2q}\right)}{\frac{\pi}{2q}} \tag{A.7}$$

will occur frequently in flux linkage calculations.

A.2 Armature Magnetic Field

To determine the armature self-inductance, first the fields produced by the armature currents must be analyzed. This model is developed in a cylindrical coordinate system, as illustrated in Fig. A.2. In this model, the magnetic fields are assumed to have no $\hat{z}$

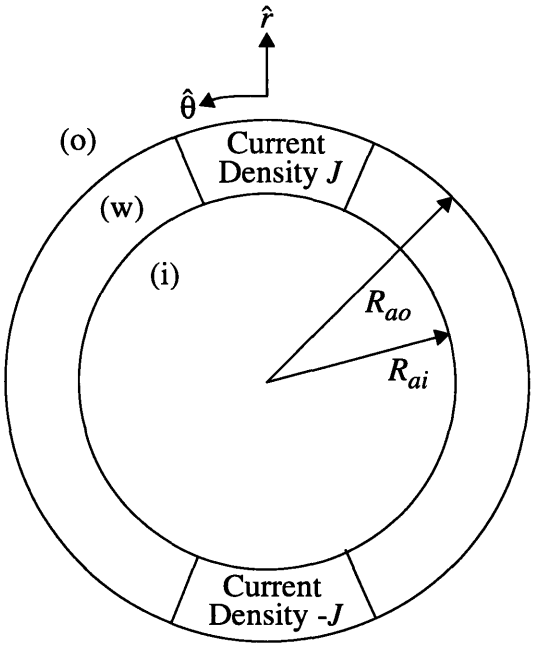

Figure A.2: Armature magnetic field model geometry for one phase

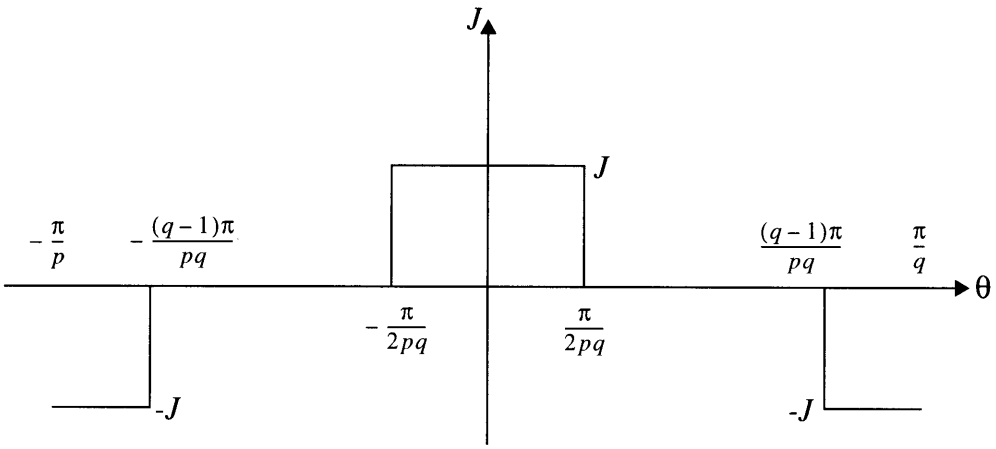

Figure A.3: Current distribution for a single armature phase

component. This will sacrifice a small bit of accuracy in exchange for a great deal of mathematical simplification.

The permeability is assumed to be μ_0 everywhere, so that there are no finite ferromagnetic boundaries. The armature windings in a single phase carry a current density J that is assumed to be z-directed and uniform throughout the armature, giving rise to a current density of magnitude

$$J = \frac{N_a I}{\frac{\theta_{we}}{2}(R_{ao}^2 - R_{ai}^2)} = \frac{N_a I}{\frac{\pi}{2q}(R_{ao}^2 - R_{ai}^2)} \tag{A.8}$$

The resulting current distribution for a single phase, illustrated in Fig. A.3, can be Fourier analyzed to give

$$J_z = \sum_{\text{n odd}} J_{zn} \cos(np\theta) \tag{A.9}$$

where

$$J_{zn} = \frac{4}{n\pi} J \sin\left(\frac{n\pi}{2q}\right) = \frac{4}{2q} J k_{wn} = \frac{4}{\pi} \frac{N_a I k_{wn}}{R_{ao}^2 - R_{ai}^2} \tag{A.10}$$

Each of these terms will produce a magnetic field, and the contribution to armature inductance of each of these fields can be summed to find the total armature self-inductance of one phase.

To solve this field problem, first define a magnetic vector potential $\boldsymbol{A}$, such that

$$\nabla \times \boldsymbol{A} = \boldsymbol{B} \tag{A.11}$$

Next, consider Ampère's Law

$$\nabla \times \boldsymbol{H} = \boldsymbol{J} \tag{A.12}$$

In a material where the permeability is divergence-free and equal to μ_0,

$$\boldsymbol{B} = \mu_0 \boldsymbol{H} \tag{A.13}$$

so that Ampère's Law can be rewritten as

$$\nabla \times \boldsymbol{B} = \nabla \times (\nabla \times \boldsymbol{A}) = \mu_0 \boldsymbol{J} \tag{A.14}$$

Using the vector identity

$$\nabla \times (\nabla \times \boldsymbol{A}) = \nabla (\nabla \cdot \boldsymbol{A}) - \nabla^2 \boldsymbol{A} \tag{A.15}$$

and the Coulomb gage

$$\nabla \cdot \boldsymbol{A} = 0 \tag{A.16}$$

Eq. A.14 can be expressed as the differential equation

$$\nabla^2 \boldsymbol{A} = -\mu_0 \boldsymbol{J} \tag{A.17}$$

which fully characterizes the magnetic field behavior in the problem.

Using the assumption that $\boldsymbol{J}$ is only z directed, this equation can be written in cylindrical coordinates as

$$\frac{1}{r}\frac{\partial}{\partial r}r\frac{\partial}{\partial r}A_z(r,\theta) + \frac{1}{r^2}\frac{\partial^2}{\partial\theta^2}A_z(r,\theta) = -\mu_0 J_z(\theta) \tag{A.18}$$

A_z will have the same θ dependence as J_z and can be expressed as

$$A_z = A(r)\cos(np\theta) \tag{A.19}$$

so that Eq. A.18 can be rewritten

$$\frac{1}{r}\frac{\partial}{\partial r}r\frac{\partial}{\partial r}A(r) + \frac{(np)^2}{r^2}A(r) = -\mu_0 J \tag{A.20}$$

The problem can now be divided into three sections (i), (w), and (o) as labeled in Fig. A.2. In each region, *A(r)* can be expressed as the sum of a homogeneous and a particular solution. The homogeneous solution will be of the form

$$A(r) = A_+ r^{np} + A_- r^{-np} \tag{A.21}$$

For the fields inside the magnets, *A(r)* must vanish at $r = 0$, establishing

$$A_-^i = 0 \tag{A.22}$$

Similarly, *A(r)* must vanish at $r = \infty$, so

$$A_+^o = 0 \tag{A.23}$$

The particular solution is also zero in these regions, because there is no current density. In the winding region, the particular solution has the form

$$A_p = \begin{cases} -\dfrac{\mu_0 J r^2}{4-(np)^2} & np \neq 2 \\ -\dfrac{\mu_0 J r^2}{4}\left(\ln r - \dfrac{1}{4}\right) & np = 2 \end{cases} \tag{A.24}$$

The vector potential in each region can now be expressed as

$$\begin{aligned} A_z^i &= A_+^i r^{np} \\ A_z^w &= A_+^w r^{np} + A_-^w r^{-np} + A_p \\ A_z^o &= A_-^o r^{-np} \end{aligned} \tag{A.25}$$

This system of equations has four unknowns, so there are four boundary conditions:

- B_r is continuous at R_{ai} and R_{ao}, which is equivalent to A_z continuous at these boundaries.
- H_θ is continuous at R_{ai} and R_{ao}, and can be obtained from

$$H_\theta = -\frac{1}{\mu_0}\frac{\partial}{\partial r}A_z \tag{A.26}$$

This establishes a system of four equations in four variables:

$$\begin{aligned} A_+^i (R_{ai})^{np} &= A_+^w (R_{ai})^{np} + A_-^w (R_{ai})^{-np} + A_p \\ A_+^w (R_{ao})^{np} + A_-^w (R_{ao})^{-np} + A_p &= A_-^o (R_{ao})^{-np} \\ npA_+^i (R_{ai})^{np-1} &= npA_+^w (R_{ai})^{np-1} - npA_-^w (R_{ai})^{(-np-1)} + \frac{\partial}{\partial r}A_p \\ npA_+^w (R_{ao})^{np-1} - npA_-^w (R_{ao})^{-np-1} + \frac{\partial}{\partial r}A_p &= -npA_-^o (R_{ao})^{-np-1} \end{aligned} \tag{A.27}$$

which can be solved to yield

$$A_i^+ = \begin{cases} \frac{1}{2}\frac{\mu_0 J}{np}\frac{(R_{ao})^{2-np} - (R_{ai})^{2-np}}{2-np} & np \neq 2 \\ \frac{1}{4}\mu_0 J \ln\frac{R_{ao}}{R_{ai}} & np = 2 \end{cases} \tag{A.28}$$

$$A_w^+ = \begin{cases} \frac{1}{2}\frac{\mu_0 J}{np}\frac{(R_{ao})^{2-np}}{2-np} & np \neq 2 \\ \frac{1}{4}\mu_0 J \ln R_{ao} & np = 2 \end{cases} \tag{A.29}$$

$$A_w^- = \begin{cases} -\frac{1}{2}\frac{\mu_0 J}{np}\frac{(R_{ai})^{2+np}}{2+np} & np \neq 2 \\ -\frac{1}{16}\mu_0 J (R_{ai})^4 & np = 2 \end{cases} \tag{A.30}$$

$$A_o^- = \begin{cases} \frac{1}{2}\frac{\mu_0 J}{np}\frac{(R_{ao})^{2+np} - (R_{ai})^{2+np}}{2+np} & np \neq 2 \\ \frac{1}{16}\mu_0 J((R_{ai})^4 - (R_{ao})^4) & np = 2 \end{cases} \tag{A.31}$$

In the inductance calculation the relevant expression is A_z in the winding, which is

$$A_z^i = \begin{cases} -\frac{1}{2}\frac{\mu_0 J}{np}\left[\frac{(R_{ao})^2}{np-2}\left(\frac{r}{R_{ao}}\right)^{np} + \frac{(R_{ai})^2}{np+2}\left(\frac{R_{ai}}{r}\right)^{np} + \frac{2npr^2}{4-(np)^2}\right]\cos(np\theta) & np \neq 2 \\ -\frac{1}{4}\mu_0 J\left[r^2\left(\ln\left(\frac{r}{R_{ao}}\right) - \frac{1}{4}\right) + \frac{1}{4}\frac{(R_{ai})^4}{r^2}\right]\cos(np\theta) & np = 2 \end{cases} \tag{A.32}$$

This expression completely characterizes the fields in the winding, which give rise to the armature self-inductance.

A.3 Armature Self-Inductance

The fields produced by the armature will in turn be linked by the armature, producing a synchronous inductance L_d, which is related to armature flux by

$$\lambda_d = L_d I \tag{A.33}$$

The flux linked by a single full pitched coil in the middle of the phase belt is

$$\lambda_i = \int_0^{LR_{ao}} \int_{R_{ai}}^{\frac{\pi}{p}} \int_0 B_r(r,\theta) r d\theta dr dz \tag{A.34}$$

Recognizing that

$$B_r = (\nabla \times \boldsymbol{A})_r = \frac{1}{r}\frac{\partial}{\partial \theta} A_z \tag{A.35}$$

this expression can be rewritten

$$\lambda_i = L \int_{R_{ai}}^{R_{ao}} \int_0^{\frac{\pi}{p}} \frac{1}{r}\frac{\partial}{\partial \theta} A_z(r,\theta) r d\theta dr = L \int_{R_{ai}}^{R_{ao}} \int_0^{\frac{\pi}{p}} d(A(r)\cos(np\theta)) dr = 2L \int_{R_{ai}}^{R_{ao}} A(r) dr \tag{A.36}$$

To find the flux linked by a distributed winding, this expression can by multiplied by the winding factor k_{wn} derived in Sec. A.1. Also, each armature turn will link flux so the flux linkage must be multiplied by a radial turns function *N(r)* before integrating over *r*. Assuming that the density of the armature turns is uniform, this function is

$$N(r) = \frac{2N_a r}{R_{ao}^2 - R_{ai}^2} \tag{A.37}$$

where the *r* dependence indicates that there is more room for turns as the radius increases. Note that this expression integrates to N_a over the armature radius. The n^{th} component of

total flux linked is then

$$\lambda_n = -\frac{4N_a L k_{wn}}{R_{ao}^2 - R_{ai}^2} \int_{R_{ai}}^{R_{ao}} A(r) r dr \tag{A.38}$$

Carrying out this integration using the expression for $A_z^i(r)$ given by Eq. A.32, and substituting for J by using Eq. A.9 gives the n^{th} component of flux linked by a single armature phase

$$L_{sn} = \frac{4}{\pi} \frac{\mu_0 (N_a)^2 (k_{wn})^2 L}{np} k_{sn} \tag{A.39}$$

where k_{sn}, the self inductance coefficient, is given by

$$k_{sn} = \begin{cases} \dfrac{np - 2 + 4\left(\dfrac{R_{ai}}{R_{ao}}\right)^{np+2} - (np+2)\left(\dfrac{R_{ai}}{R_{ao}}\right)^4}{\left(\left(\dfrac{R_{ai}}{R_{ao}}\right)^2 - 1\right)^2 ((np)^2 - 4)} & np \neq 2 \\ \dfrac{1}{4} \dfrac{1 + \left(4 \ln\left(\dfrac{R_{ai}}{R_{ao}}\right) - 1\right)\left(\dfrac{R_{ai}}{R_{ao}}\right)^4}{\left(\left(\dfrac{R_{ai}}{R_{ao}}\right)^2 - 1\right)^2} & np = 2 \end{cases} \tag{A.40}$$

For a q-phase armature winding, a good approximation to the n^{th} component of total armature inductance is

$$L_n = \frac{q}{2} L_{sn} \tag{A.41}$$

The total armature inductance L_{dt} is then

$$L_{dt} = \sum_{\text{n odd}} L_n \tag{A.42}$$

For purposes of three-phase machine design the fundamental component

$$L_d = \frac{3}{2}\frac{4}{\pi}\frac{\mu_0 (N_a)^2 (k_{wn})^2 L}{np} k_{sn}\Big|_{n=1} = \frac{3}{2}\frac{4}{\pi}\frac{\mu_0 (N_a)^2 (k_w)^2 L}{p} k_s \tag{A.43}$$

where

$$k_s = \begin{cases} \dfrac{p - 2 + 4\left(\dfrac{R_{ai}}{R_{ao}}\right)^{p+2} - (p+2)\left(\dfrac{R_{ai}}{R_{ao}}\right)^4}{\left(\left(\dfrac{R_{ai}}{R_{ao}}\right)^2 - 1\right)^2 (p^2 - 4)} & p \neq 2 \\ \dfrac{1}{4}\dfrac{1 + \left(4\ln\left(\dfrac{R_{ai}}{R_{ao}}\right) - 1\right)\left(\dfrac{R_{ai}}{R_{ao}}\right)^4}{\left(\left(\dfrac{R_{ai}}{R_{ao}}\right)^2 - 1\right)^2} & p = 2 \end{cases} \tag{A.44}$$

gives a good approximation to the air gap armature self-inductance.

Appendix B

Armature Flux Linkage of Magnet-Produced Field

As outlined in Sec. 2.5.2, the magnet flux linked by the armature winding is related to the torque rating of the machine as well as terminal electrical characteristics. In this section, an expression for the magnetic flux produced by a Halbach permanent magnet array is derived, and then the total flux linked by each phase of the winding is calculated.

B.1 Magnet-Produced Magnetic Field

In this section, analytical methods are used to derive the magnetic fields arising from a Halbach magnet array. In particular, an expression is obtained for the fields in the interior of the array, which will in turn be linked by the armature and produce back emf and torque. The model is constructed in cylindrical coordinates and is picture in Fig. B.1.

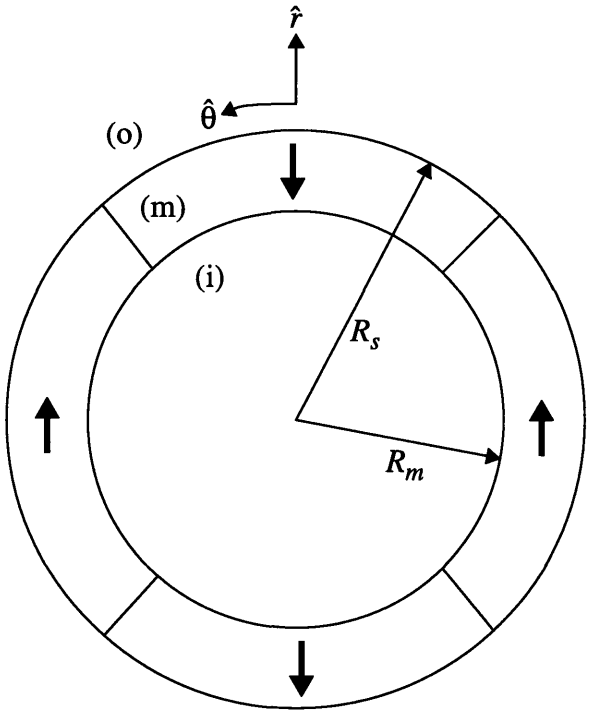

Figure B.1: Magnet field model geometry

The magnets are assumed to have a magnetization field M that is divergence free and oriented either in the azimuthal or radial direction. For the radially oriented magnets,

$$\boldsymbol{M} = \frac{M_0 R_s}{r}\hat{r} \tag{B.1}$$

and for the azimuthally magnetized magnets,

$$\boldsymbol{M} = \frac{M_0 R_s}{r}\hat{\theta} \tag{B.2}$$

M_0 is the magnetization of the magnet material and is given by

$$M_o = \mu_r \mu_0 B_r \tag{B.3}$$

where B_r is the residual flux density of the magnets and μ_r is the relative permeability of the magnets.

The azimuthal variation of the magnetization is illustrated in Fig. B.2 . These magnetization functions M_r and M_θ can be Fourier analyzed to yield

$$M_r = \sum_{\text{n odd}} M_{rn}\cos(np\theta) = \sum_{\text{n odd}} \frac{4}{\pi}\frac{M_o R_s}{nr}\sin\left(\frac{n\pi}{4}\right)\cos(np\theta) = \sum_{\text{n odd}} \frac{\hat{M}_r}{r}\cos(np\theta) \tag{B.4}$$

and

$$M_\theta = \sum_{\text{n odd}} M_{\theta n}\sin(np\theta) = \sum_{\text{n odd}} \frac{4}{\pi}\frac{M_o R_s}{nr}\cos\left(\frac{n\pi}{4}\right)\sin(np\theta) = \sum_{\text{n odd}} \frac{\hat{M}_\theta}{r}\sin(np\theta) \tag{B.5}$$

where we have defined

$$\hat{M}_r = \frac{4}{\pi}\frac{M_o R_s}{n}\sin\left(\frac{n\pi}{4}\right) \qquad \hat{M}_\theta = \frac{4}{\pi}\frac{M_o R_s}{n}\cos\left(\frac{n\pi}{4}\right) \tag{B.6}$$

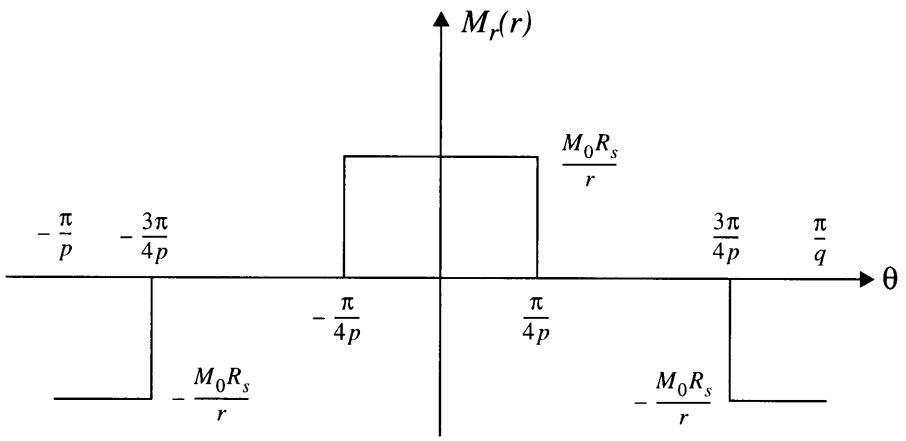

(a)

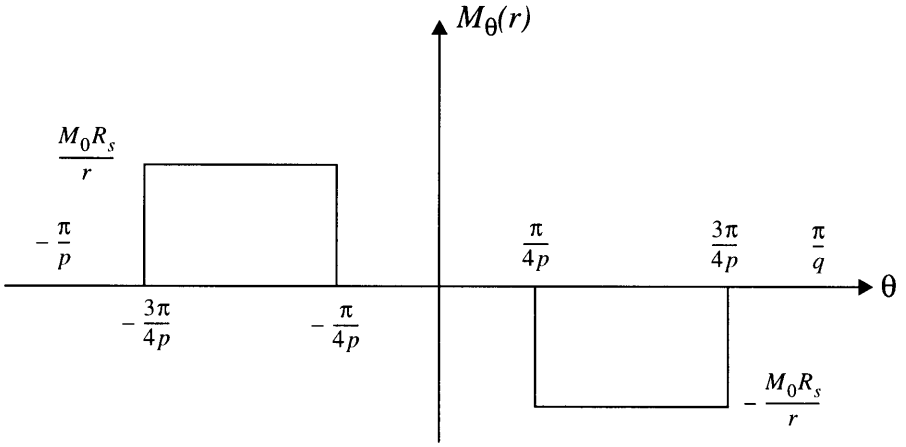

(b)

Figure B.2: Magnetization distribution in a Halbach magnet array for the (a) radially magnetized and (b) azimuthally magnetized magnets

There are no currents in the problem, so we can define a scalar magnetic potential ψ that characterizes the magnetic field, where

$$\boldsymbol{H} = -\nabla\psi \tag{B.7}$$

Taking the divergence of both sides of this equation and rearranging yields

$$\nabla^2\psi = -\nabla \cdot \boldsymbol{H} \tag{B.8}$$

Now using the fact that magnetic flux density is divergenceless,

$$\nabla \cdot \boldsymbol{B} = \mu \nabla \cdot (\boldsymbol{H} + \boldsymbol{M}) = 0 \tag{B.9}$$

rearranging,

$$-\nabla \cdot \boldsymbol{H} = \nabla \cdot \boldsymbol{M} \tag{B.10}$$

and combining this with Eq. B.8 yields

$$\nabla^2 \psi = \nabla \cdot \boldsymbol{M} \tag{B.11}$$

This equation characterizes the magnet-produced fields everywhere in the machine.

The concept of superposition is now applied to divide the problem into two subproblems, one involving the radially oriented magnets and another involving the azimuthally oriented magnets. Because

$$\boldsymbol{M} = M_r \hat{r} + M_\theta \hat{\theta} \tag{B.12}$$

the resulting magnetic potential will be a superposition the of potential distributions resulting from each magnetization:

$$\psi = \psi_r + \psi_\theta \tag{B.13}$$

where

$$\nabla^2 \psi_r = \nabla \cdot \boldsymbol{M}_r \qquad \nabla^2 \psi_\theta = \nabla \cdot \boldsymbol{M}_\theta \tag{B.14}$$

Using the definition of divergence

$$\nabla \cdot \boldsymbol{M} = \frac{1}{r}\frac{\partial}{\partial r}(rM_r) + \frac{1}{r}\frac{\partial}{\partial \theta}M_\theta \tag{B.15}$$

and applying this to Eqs. B.4 and B.5 on a termwise basis gives

$$\nabla \cdot \boldsymbol{M}_r = 0 \qquad \nabla \cdot \boldsymbol{M}_\theta = \frac{np}{r^2}\hat{M}_\theta \cos(np\theta) \tag{B.16}$$

The radial magnets, then, will produce a Laplacian field, but the azimuthal magnet potential will have a particular solution that solves

$$\nabla^2 \psi_\theta^p = \frac{np}{r^2}\hat{M}_\theta \cos(np\theta) \tag{B.17}$$

The solution to this equation is

$$\psi_\theta^p = -\frac{\hat{M}_\theta}{np}\cos(np\theta) \tag{B.18}$$

The problem can now be divided into three regions (i), (m), and (o) and shown in Fig. B.1. Each region will have a homogeneous solution for vector potential that satisfies Laplace's equation

$$\nabla^2 \psi^h = 0 \tag{B.19}$$

In both regions, the solution to this equation will be of the form

$$\psi^h = (\psi^+ r^{np} + \psi^- r^{-np})\cos(np\theta) \tag{B.20}$$

The vector potential must vanish at $r = 0$ and $r = \infty$, establishing

$$\psi_{r,i}^- = \psi_{r,o}^+ = \psi_{\theta,i}^- = \psi_{\theta,o}^+ = 0 \tag{B.21}$$

The form of the total solution for vector potential in each region is then, for the radial magnets,

$$\begin{aligned}
\psi_{r,i} &= \psi^{+}_{r,i} r^{np} \cos(np\theta) \\
\psi_{r,m} &= (\psi^{+}_{r,m} r^{np} + \psi^{-}_{r,m} r^{-np}) \cos(np\theta) \\
\psi_{r,o} &= \psi^{-}_{r,o} r^{-np} \cos(np\theta)
\end{aligned} \tag{B.22}$$

and for the azimuthal magnets,

$$\begin{aligned}
\psi_{\theta,i} &= \psi^{+}_{\theta,i} r^{np} \cos(np\theta) \\
\psi_{\theta,m} &= \left(\psi^{+}_{\theta,m} r^{np} + \psi^{-}_{\theta,m} r^{-np} - \frac{\hat{M}_\theta}{np}\right) \cos(np\theta) \\
\psi_{\theta,o} &= \psi^{-}_{\theta,o} r^{-np} \cos(np\theta)
\end{aligned} \tag{B.23}$$

In both subproblems there are four free variables, and the four appropriate boundary conditions are

- H_θ is continuous at R_m and R_s, which is equivalent to ψ continuous at these boundaries.
- B_r is continuous at R_m and R_s, and can be obtained from

$$B_r = \mu_0(H_r + M_r) = \mu_0\left(-\frac{\partial \psi}{\partial r} + M_r\right) \tag{B.24}$$

This establishes a set of four equations in four variables for each subproblem:

$$\psi^{+}_{i}(R_m)^{np} = \psi^{+}_{m}(R_m)^{np} + \psi^{-}_{m}(R_m)^{-np} + \begin{cases} 0 & \text{radial} \\ -\dfrac{\hat{M}_\theta}{np} & \text{azimuthal} \end{cases} \tag{B.25}$$

$$\psi^{-}_{o}(R_s)^{-np} = \psi^{+}_{m}(R_s)^{np} + \psi^{-}_{m}(R_s)^{-np} + \begin{cases} 0 & \text{radial} \\ -\dfrac{\hat{M}_\theta}{np} & \text{azimuthal} \end{cases} \tag{B.26}$$

$$np\psi_i^+(R_m)^{np-1} = np\psi_m^+(R_m)^{np-1} - np\psi_m^-(R_m)^{-np-1} + \begin{cases} -\dfrac{\hat{M}_r}{R_m} & \text{radial} \\ 0 & \text{azimuthal} \end{cases} \tag{B.27}$$

$$-np\psi_o^-(R_s)^{-np-1} = np\psi_m^+(R_s)^{np-1} - np\psi_m^-(R_s)^{-np-1} + \begin{cases} -\dfrac{\hat{M}_r}{R_m} & \text{radial} \\ 0 & \text{azimuthal} \end{cases} \tag{B.28}$$

These equations can be solved to give

$$\begin{aligned}
\psi_{r,i}^+ &= \frac{1}{2}\frac{\hat{M}_r}{np}\left(\left(\frac{1}{R_s}\right)^{np} - \left(\frac{1}{R_m}\right)^{np}\right) & \psi_{\theta,i}^+ &= \frac{1}{2}\frac{\hat{M}_\theta}{np}\left(\left(\frac{1}{R_s}\right)^{np} - \left(\frac{1}{R_m}\right)^{np}\right) \\
\psi_{r,m}^+ &= \frac{1}{2}\frac{\hat{M}_r}{np}\left(\frac{1}{R_s}\right)^{np} & \psi_{\theta,m}^+ &= \frac{1}{2}\frac{\hat{M}_\theta}{np}\left(\frac{1}{R_s}\right)^{np} \\
\psi_{r,m}^- &= -\frac{1}{2}\frac{\hat{M}_r}{np}\left(\frac{1}{R_m}\right)^{-np} & \psi_{\theta,m}^- &= \frac{1}{2}\frac{\hat{M}_\theta}{np}\left(\frac{1}{R_m}\right)^{-np} \\
\psi_{r,o}^- &= -\frac{1}{2}\frac{\hat{M}_r}{np}\left(\left(\frac{1}{R_s}\right)^{-np} - \left(\frac{1}{R_m}\right)^{-np}\right) & \psi_{\theta,o}^- &= -\frac{1}{2}\frac{\hat{M}_\theta}{np}\left(\left(\frac{1}{R_s}\right)^{-np} - \left(\frac{1}{R_m}\right)^{-np}\right)
\end{aligned} \tag{B.29}$$

Note that for the fundamental term, $\hat{M}_r = \hat{M}_\theta$, and so the fields reinforce inside the magnets and cancel outside of the magnets. This field concentration produces a field intensity that is approximately $\sqrt{2}$ times greater than the field produced by a conventional array with only radially oriented magnets.

In calculating the armature flux linkage, the magnetic potential inside the magnets is the relevant expression. It is the superposition of the potential produced by the radial and azimuthal magnets:

$$\begin{aligned}\psi_i &= \frac{1}{2}\frac{1}{np}\frac{4}{\pi}\frac{M_0 R_s}{n}\left(\sin\left(\frac{n\pi}{4}\right)+\cos\left(\frac{n\pi}{4}\right)\right)\left(\left(\frac{r}{R_s}\right)^{np}-\left(\frac{r}{R_m}\right)^{np}\right)\cos(np\theta)\\ &= \frac{4}{\pi}\cos\left((n-1)\frac{\pi}{4}\right)\frac{\sqrt{2}}{2}\frac{M_0 R_s}{n^2 p}\left(\left(\frac{r}{R_s}\right)^{np}-\left(\frac{r}{R_m}\right)^{np}\right)\cos(np\theta)\end{aligned} \tag{B.30}$$

The armature will link radial magnetic flux, which can be obtained from

$$B_{rn} = \mu_0 H_r = \mu_0(-\nabla\psi)_r = -\mu_0\frac{\partial\psi}{\partial r} \tag{B.31}$$

Carrying this out gives

$$B_{rn} = \frac{4}{\pi}\cos\left((n-1)\frac{\pi}{4}\right)\frac{\sqrt{2}}{2}\frac{B_r}{n}\left(\frac{R_s}{R_m}\left(\frac{r}{R_m}\right)^{np-1}-\left(\frac{r}{R_s}\right)^{np-1}\right)\cos(np\theta) \tag{B.32}$$

Time-average torque will only be produced by the fundamental component of the radial flux

$$B_{rf} = \frac{4}{\pi}\sqrt{2}B_r k_m(r)\cos(p\theta) \tag{B.33}$$

where the magnet coefficient $k_m(r)$ is

$$k_m(r) = \frac{1}{2}\left[\frac{R_s}{R_m}\left(\frac{r}{R_m}\right)^{p-1}-\left(\frac{r}{R_s}\right)^{p-1}\right] \tag{B.34}$$

B.2 Armature Flux Linkage

The radial magnetic flux density derived in the previous section will be linked by the armature winding to produce a back emf and an accompanying torque. The flux density must be integrated over the volume of the armature winding to find the flux linkage λ. Because the number of turns at a given radius increases with radius, as captured in Eq. A.37, the flux must be multiplied by the turns function

$$N(r) = \frac{2N_a r}{(R_{ao})^2 - (R_{ai})^2} \tag{B.35}$$

before the integration is carried out. Also, the effect of the distributed nature of the winding is captured by the winding factor

$$k_w = \frac{\sin\left(\frac{\pi}{2q}\right)}{\frac{\pi}{2q}} \tag{B.36}$$

derived in Section A.1.

The RMS value of flux linkage is then given by

$$\lambda_a = \frac{1}{\sqrt{2}} \int_0^{L} \int_{R_{ai}}^{R_{ao}} \int_0^{\frac{\pi}{p}} B_{rf}(r, \theta) N(r) k_w r d\theta dr dz \tag{B.37}$$

To simplify the calculation, define

$$B_{rf}(r, \theta) = \hat{B}_{rf} r^{p-1} \cos(np\theta) \tag{B.38}$$

where

$$\hat{B}_{rf} = \frac{4}{\pi} \sqrt{2} B_r \frac{1}{2} \left[\frac{R_s}{R_m} \left(\frac{1}{R_m} \right)^{p-1} - \left(\frac{1}{R_s} \right)^{p-1} \right] \tag{B.39}$$

Substituting Eqs. B.35 and B.38 into Eq. B.37 gives

$$\lambda_a = \frac{2N_a}{(R_{ao})^2-(R_{ai})^2}\frac{\hat{B}_{rf}}{\sqrt{2}}k_w L\int_{R_{ai}}^{R_{ao}}\int_0^{\frac{\pi}{p}} r^{p+1}\cos(p\theta)d\theta dr$$
$$= \frac{2N_a}{(R_{ao})^2-(R_{ai})^2}\frac{\hat{B}_{rf}}{\sqrt{2}}\frac{2k_w L}{p(p+2)}((R_{ao})^{p+2}-(R_{ai})^{p+2}) \quad \text{(B.40)}$$

To express the flux in a more compact manner, we can derive an armature thickness coefficient k_t that is the ratio of the flux linked by a radially distributed winding to the flux linked by a winding concentrated at the inner armature radius R_{ai}. The RMS flux λ_c linked by this concentrated winding would be

$$\lambda_c = N_a\frac{\hat{B_{rf}}}{\sqrt{2}}k_w L(R_{ai})^p\int_0^{\frac{\pi}{p}}\cos(p\theta)d\theta = \frac{2N_a\hat{B_{rf}}k_w L(R_{ai})^p}{p} \quad \text{(B.41)}$$

The armature thickness coefficient is then

$$k_t = \frac{\lambda_a}{\lambda_c} = \frac{2\left(\frac{R_{ai}}{R_{ao}}\right)^{-p}\left(1-\left(\frac{R_{ai}}{R_{ao}}\right)^{p+2}\right)}{(p+2)\left(1-\left(\frac{R_{ai}}{R_{ao}}\right)^2\right)} \quad \text{(B.42)}$$

Combining Eqs. B.41 and B.42, and substituting for $\hat{B_{rf}}$ from Eq. B.39 gives

$$\lambda_a = \frac{4}{\pi}\frac{2B_r N_a R_{ai} L k_w k_t}{p}\frac{1}{2}\left[\frac{R_s}{R_m}\left(\frac{R_{ai}}{R_m}\right)^{p-1}-\left(\frac{R_{ai}}{R_s}\right)^{p-1}\right] = \frac{4}{\pi}\frac{2B_r N_a R_{ai} L k_w k_m k_t}{p} \quad \text{(B.43)}$$

where we have defined

$$k_m = k_m(r)\big|_{r=R_{ai}} \quad \text{(B.44)}$$

As indicated in Eq. 2.15, the back emf of the motor is the time derivative of the armature flux, so

$$E_{af} = \frac{d}{dt}\lambda_a = \omega_e \lambda_a = \frac{4}{\pi} 2 B_r N_a R_{ai} L k_w k_m k_t \tag{B.45}$$

The flux also acts in accordance with Eq. 2.16 to produce the torque

$$T = 3 p \lambda_a I \cos\delta \tag{B.46}$$

Appendix C

End Turn Analysis

As described in Secs. 2.5.1 and 2.5.4, the length of the end turns in the motor-alternator will have an effect on the armature resistance as well as the overall machine length. This appendix develops a simple model for the length of the end turns in each armature phase.

To construct the model, the armature phase belts are unrolled to produce the geometry illustrated in Fig C.1 The end turns are then modeled as triangular and the wires are packed to their maximum capacity in the end turns. This requires that there be some extra room in the axial wires to accommodate bending the wires to form end turns. We can then

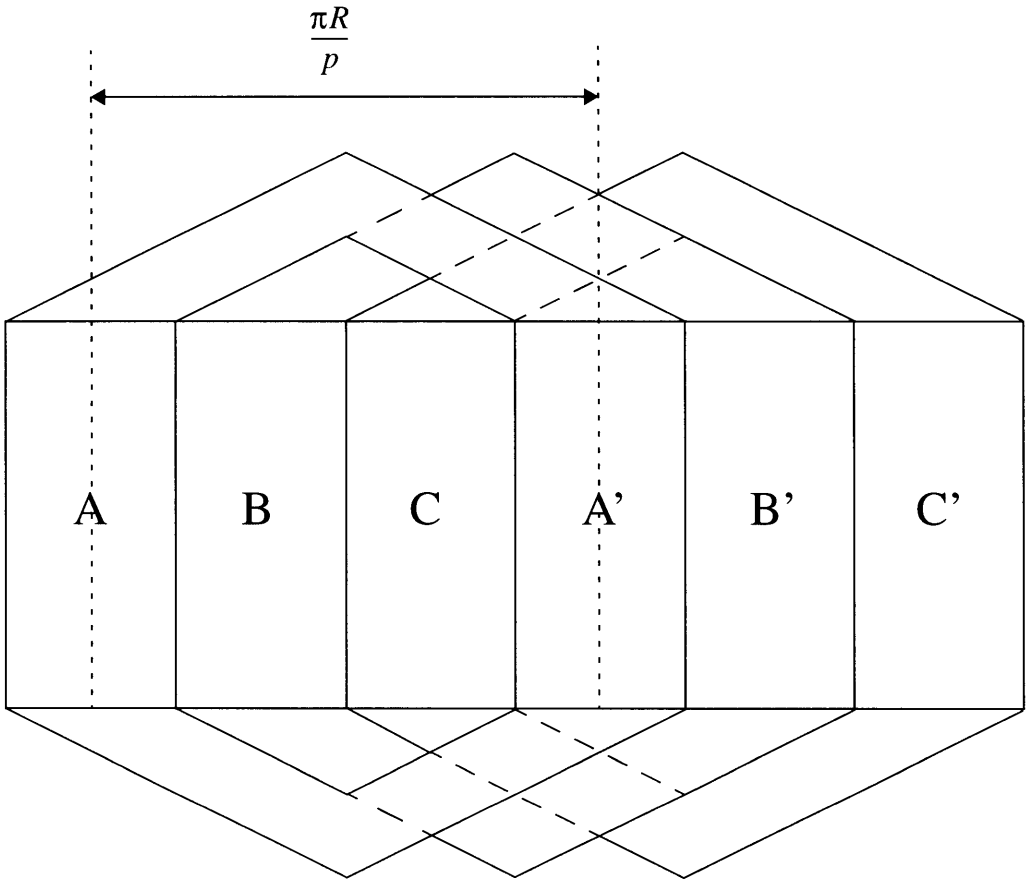

Figure C.1: End turn geometry for one pole

specify a packing factor λ_p that relates the actual cross sectional wire area to the maximum area obtainable. The percentage of the armature occupied by conductors is given by

$$\lambda_a = \frac{6N_{ac}\pi\left(\frac{d_w}{2}\right)^2}{\pi(R_{ao}^2 - R_{ai}^2)} \tag{C.1}$$

The maximum ratio can be approximated by considering the ratio of the area of a circle to a square surrounding and tangent to it, which is

$$\lambda_{max} = \frac{\pi}{4} \tag{C.2}$$

The packing factor is then

$$\lambda_p = \frac{\lambda_c}{\lambda_{max}} = \frac{4}{\pi}\frac{6N_{ac}\left(\frac{d_w}{2}\right)^2}{(R_{ao}^2 - R_{ai}^2)} \tag{C.3}$$

In Fig. C.2, the geometry of one phase belt is illustrated. *CE* is the coil span of each phase, given by

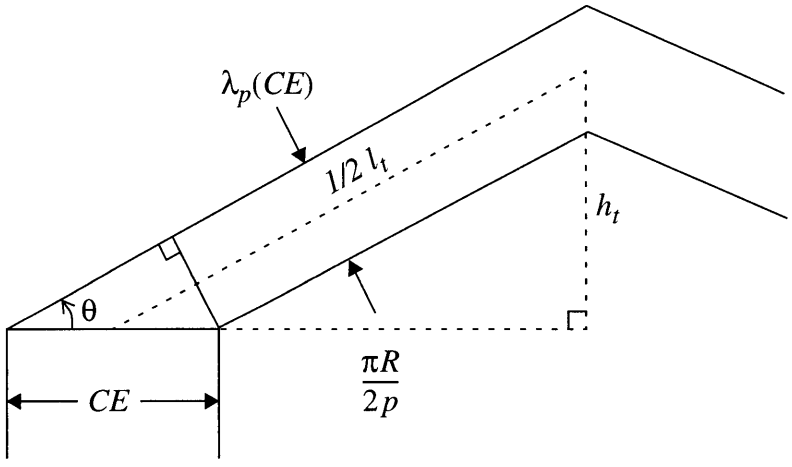

Figure C.2: Detailed view of end turn geometry

$$CE = \frac{\pi R}{pq} \tag{C.4}$$

where R is the average radius of the armature winding. The wires are packed to the maximum in the end turns, so the width of the end turns is $\lambda_p CE$. This establishes the angle θ as

$$\theta = \operatorname{asin}\left(\frac{\lambda_p CE}{CE}\right) = \operatorname{asin}\lambda_p \tag{C.5}$$

The length of the one end turn l_t is then given by

$$l_t = 2CE\cos\theta = \frac{2CE}{\sqrt{1-\lambda_p^2}} = \frac{4\pi R}{pq\sqrt{1-\lambda_p^2}} \tag{C.6}$$

Similarly the height of one end turn h_t is given by

$$h_t = CE\tan\theta = \frac{2\pi R\lambda_p}{pq\sqrt{1-\lambda_p^2}} \tag{C.7}$$

The end turn length and height are then inversely proportional to the number of pole pairs, which will play a part in the integrated motor-alternator design.

Appendix D

Armature Eddy Current Loss

As outlined in Sec. 2.5.3.1, eddy current losses in the armature wires contribute to armature losses and reduce electrical efficiency. These losses arise because the armature is immersed in the time-varying magnetic field of the rotor. This appendix develops an expression for these losses.

The model geometry showing one wire is illustrated in Fig D.1 It is assumed that the magnetic field is crosses the wire in only one direction. A further assumption is that the azimuthal field contributes a negligible amount to average flux density in the armature, so the field is considered to be entirely the radial magnetic field. The Fourier series for the magnet-produced radial magnetic flux density is given by Eq. B.32.

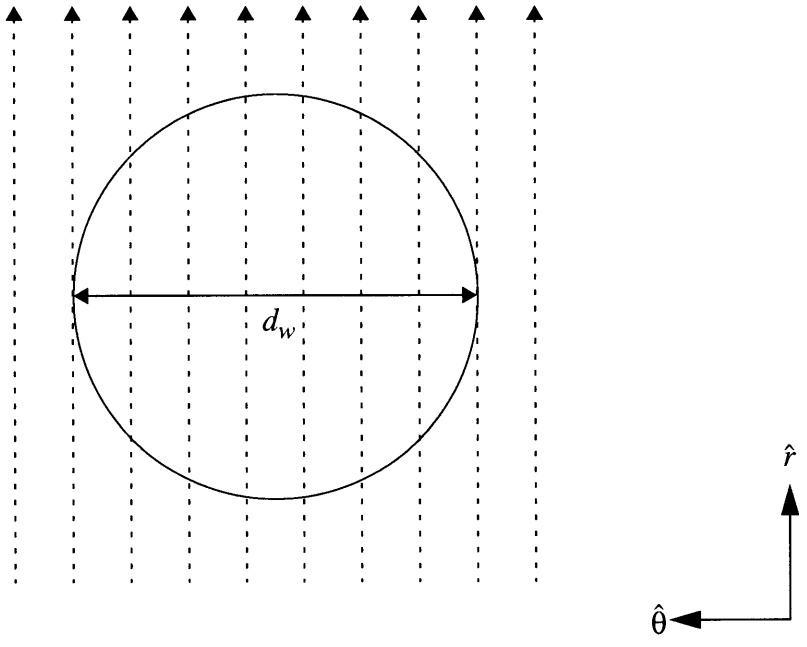

Figure D.1: Armature wire exposed to time-varying magnetic field

In this model only the fundamental term in this series will be considered. This is an approximation, because the electrical frequency is proportional to harmonic number, while the magnitude of the field harmonics is inversely proportional to harmonic number. It is assumed that for the higher order harmonics the skin depth of the copper becomes small enough that the fields are attenuated significantly and can be neglected.

For the fundamental harmonic, the magnetic field is assumed to fully penetrate the wire, eliminating the need to solve the diffusion equation. Following Eq. B.33, the fundamental rotor flux density harmonic is given by

$$B_{rf} = \frac{4}{\pi}\sqrt{2}B_r k_m(r)\cos(p\theta) \tag{D.1}$$

This can be averaged over the radius of the armature by multiplying by the armature thickness coefficient k_t derived in Sec. B.2, and averaged azimuthally by taking the RMS value. If we define B_1 to be the magnitude of this wave

$$B_1 = \frac{4}{\pi}B_r k_m k_t \tag{D.2}$$

the space average, time-varying flux-density is then

$$\boldsymbol{B} = \Re\{B_1 e^{j\omega_e t}\hat{y}\} = \Re\{B_1 e^{j\omega_e t}(\cos\phi\hat{r} - \sin\phi\hat{\phi})\} \tag{D.3}$$

The electric field in the wire can be found applying Faraday's Law

$$\nabla\times\boldsymbol{E} = -\frac{\partial \boldsymbol{B}}{\partial t} \tag{D.4}$$

to Eq. D.3 to obtain

$$E_z = \Re\{j\omega_e B_1 e^{j\omega_e t} r\sin\phi\} \tag{D.5}$$

The time-average power loss can be found by integrating this field over the volume of the wire and over time to give

$$P_w = \int_0^L \int_0^{2\pi} \int_0^{\frac{d_w}{2}} \frac{1}{2}\sigma_c |E_z|^2 r dr d\theta dz \tag{D.6}$$

where σ_c is the conductivity of the copper wire. This integral evaluates to

$$P_w = \frac{\pi L(\omega_e)^2 (B_1)^2 \sigma_c (d_w)^4}{128} \tag{D.7}$$

There are $6N_{ac}$ wires in the armature, so the total time-average eddy current loss will be given by

$$P_{ec} = \frac{6\pi N_{ac} L(\omega_e)^2 (B_1)^2 \sigma_c (d_w)^4}{128} \tag{D.8}$$

Appendix E

2D Rotor Eddy Current Loss Model

As discussed in Section 2.5.3.2, eddy currents will arise in the conducting magnets because they are exposed to time-changing magnetic fields produced by armature space harmonics. This appendix presents a method of characterizing the losses arising from these eddy currents. Because this model is the primary research focus of this thesis, the model will be developed in a high degree of complexity to assure the accuracy of results.

E.1 Transfer Relation Equations

As Eq. 2.65 indicates, the power loss in a 2D element can be completely characterized by the fields A_z (or equivalently E_z) and tangential **H** at the *boundary* of the object. The eddy current loss model then reduces to a model of these two boundary fields. A plausible approach to finding these fields is to solve the diffusion equation, Eq. 2.54, for the distributed magnetic fields, and then apply Faraday's Law to find the electric field. This approach is unnecessarily complex, however, because it involves obtaining quantities like the radial magnetic field and the fields inside the element. These are not needed in the loss model, so an approach that finds the fields at the boundaries is sufficient.

Such a method for characterizing boundaries has been developed by Melcher [16]. It relates tangential **H** to z-directed **A** at the boundaries of a region, and can be used in either rectangular or cylindrical coordinates, as shown in Fig. E.1. The region has some constant depth, and is assumed to extend infinitely in the lateral direction in rectangular coordinates, or join itself to form an annulus in cylindrical coordinates. Each region can have any permeability and conductivity, provided that it is linear.

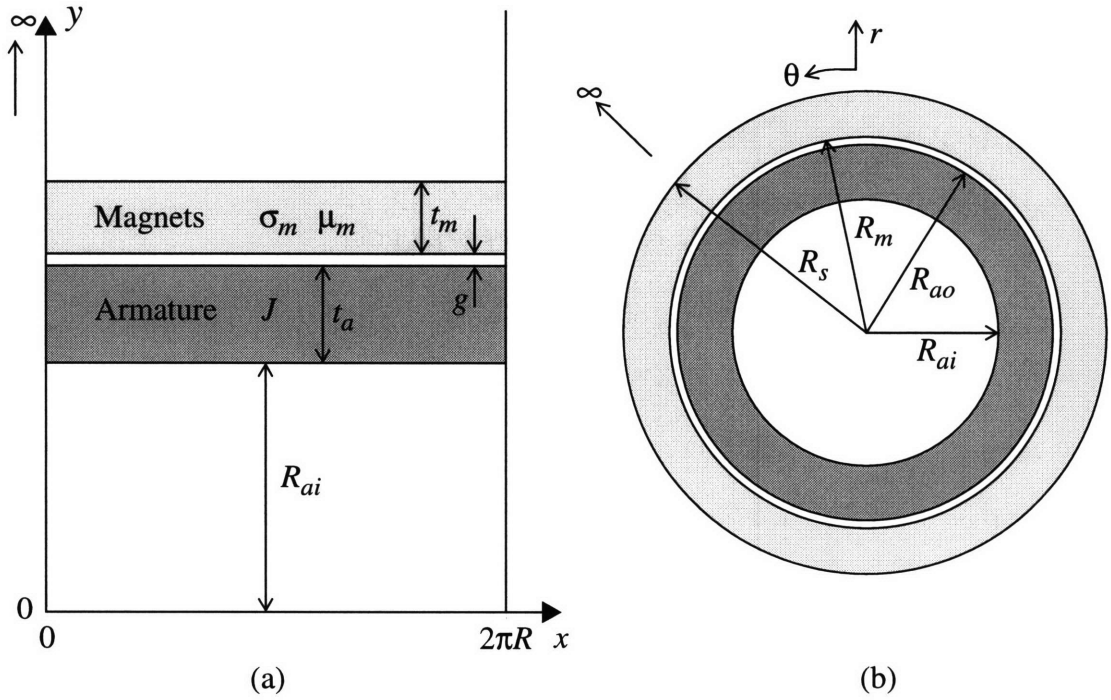

Figure E.1: Rotor eddy current loss model geometries in (a) rectangular and (b) cylindrical coordinates

Note that for the rectangular model, R is not distinctly specified by the machine geometry, because the radii of the regions in the machine vary. In this design it was set equal to the magnet inner R_m, but for machines where the wavelength of excitation is comparable to this radius, the rectangular model will begin to lose accuracy. This represents the major limitation of the rectangular model. For this reason a more accurate model in cylindrical coordinates is also developed.

The field transfer relations can be obtained by solving the diffusion equation inside the region. The diffusion equation in **A** is

$$\nabla^2 \boldsymbol{A} = \mu\sigma\frac{\partial}{\partial t}\boldsymbol{A} \tag{E.1}$$

and because $\boldsymbol{A}$ is only $\underline{z}$-directed this can be written

$$\nabla^2 A_z = \mu\sigma\frac{\partial}{\partial t}A_z \tag{E.2}$$

In this problem, A_z in each coordinate system will be of the form

$$A_z = \Re\left\{A_z(y)e^{j\left(\frac{np}{R}x + n_t\omega_e t\right)}\right\} \qquad A_z = \Re\{A_z(r)e^{j(np\theta + n_t\omega_e t)}\} \tag{E.3}$$

These expression can be substituted into Eq. E.2 and the definition of the Laplacian used to give

$$\frac{\partial^2}{\partial x^2}A_z(x, y) + \frac{\partial^2}{\partial y^2}A_z(x, y) = \frac{\partial^2}{\partial y^2}A_z(y) - \left(\frac{np}{R}\right)^2 A_z(y) = j\mu\sigma p\omega_e A_z(y) \tag{E.4}$$

in rectangular coordinates, and

$$\frac{1}{r}\frac{\partial}{\partial r}\left(r\frac{\partial}{\partial r}A_z(r, \theta)\right) + \frac{1}{r^2}\frac{\partial^2}{\partial \theta^2}A_z(r, \theta) = \frac{1}{r}\frac{\partial}{\partial r}\left(r\frac{\partial}{\partial r}A_z(r)\right) - \left(\frac{np}{r}\right)^2 A_z(r) = j\mu\sigma p\omega_e A_z(r) \tag{E.5}$$

in cylindrical coordinates.

- **Rectangular coordinates** Eq. E.4 is a linear differential equation with homogeneous solution

$$A_z(y) = k_+ e^{\alpha y} + k_- e^{-\alpha y} \tag{E.6}$$

where k_+ and k_- are constants and

$$\alpha = \sqrt{\left(\frac{np}{R}\right)^2 + j\mu\sigma n_t\omega_e} \tag{E.7}$$

The magnetic field can now be found from

$$H_x = \frac{1}{\mu}B_x = \frac{1}{\mu}(\nabla\times\boldsymbol{A})_x = \frac{1}{\mu}\frac{\partial}{\partial y}A_z = \frac{1}{\mu}[\alpha k_+ e^{\alpha y} - \alpha k_- e^{-\alpha y}] \tag{E.8}$$

If the tangential magnetic fields at the boundaries are

$$H_x\big|_{y=0} = \hat{H}_x^1 \qquad\qquad H_x\big|_{y=\Delta} = \hat{H}_x^2 \tag{E.9}$$

this creates a system of 2 equations in k_+ and k_- that can be solved to give

$$\begin{aligned} k_+ &= -\left(\frac{\mu}{\alpha}\frac{e^{-\alpha\Delta}}{e^{\alpha\Delta}-e^{-\alpha\Delta}}\right)\hat{H}_x^1 + \left(\frac{\mu}{\alpha}\frac{1}{e^{\alpha\Delta}-e^{-\alpha\Delta}}\right)\hat{H}_x^2 \\ k_- &= \left(\frac{\mu}{\alpha}\frac{1}{e^{\alpha\Delta}-e^{-\alpha\Delta}}\right)\hat{H}_x^1 - \left(\frac{\mu}{\alpha}\frac{1}{e^{\alpha\Delta}-e^{-\alpha\Delta}}\right)\hat{H}_x^2 \end{aligned} \tag{E.10}$$

Substituting these back into Eq. E.6 and evaluating at the boundaries gives the complete transfer relation

$$\begin{bmatrix}\hat{A}_z^1\\ \hat{A}_z^2\end{bmatrix} = \frac{\mu}{\alpha}\begin{bmatrix}-\coth(\alpha\Delta) & \dfrac{1}{\sinh(\alpha\Delta)}\\ \dfrac{-1}{\sinh(\alpha\Delta)} & \coth(\alpha\Delta)\end{bmatrix}\begin{bmatrix}\hat{H}_x^1\\ \hat{H}_x^2\end{bmatrix} \tag{E.11}$$

• **Cylindrical coordinates** Transfer relations can be similarly constructed for a region in cylindrical coordinates. This analysis will not be carried out here because, in general, there is no closed form solution to Eq. E.5. The solutions to this equation are combinations of the *Bessel functions*, which are infinite series that can be approximated by polynomials. The transfer relation is

$$\begin{bmatrix}\hat{A}_z^i\\ \hat{A}_z^o\end{bmatrix} = \mu\begin{bmatrix}F(R_o,R_i,\gamma,np) & G(R_i,R_o,\gamma,np)\\ G(R_o,R_i,\gamma,np) & F(R_i,R_o,\gamma,np)\end{bmatrix}\begin{bmatrix}\hat{H}_\theta^i\\ \hat{H}_\theta^o\end{bmatrix} \tag{E.12}$$

where

$$\gamma = \sqrt{j\mu\sigma n_t \omega_e} \tag{E.13}$$

Note that $\gamma = 0$ for non-conducting regions, including air. The functions F and G are similar to the hypertrigonometric functions of Eq. E.11, and are given by

$$F(R_a, R_b, \gamma, m) = \begin{cases} \dfrac{R_b}{m}\dfrac{\left(\dfrac{R_a}{R_b}\right)^m + \left(\dfrac{R_b}{R_a}\right)^m}{\left(\dfrac{R_a}{R_b}\right)^m - \left(\dfrac{R_b}{R_a}\right)^m} & \gamma = 0 \\ \dfrac{1}{j\gamma}\dfrac{J_m'(j\gamma R_a)H_m(j\gamma R_b) - H_m'(j\gamma R_a)J_m(j\gamma R_b)}{J_m'(j\gamma R_b)H_m'(j\gamma R_a) - J_m'(j\gamma R_a)H_m'(j\gamma R_b)} & \gamma \neq 0 \end{cases} \tag{E.14}$$

$$G(R_a, R_b, \gamma, m) = \begin{cases} \dfrac{2R_b}{m}\dfrac{1}{\left(\dfrac{R_a}{R_b}\right)^m - \left(\dfrac{R_b}{R_a}\right)^m} & \gamma = 0 \\ \dfrac{1}{j\pi\gamma(\gamma R_a)}\dfrac{1}{J_m'(j\gamma R_b)H_m'(j\gamma R_a) - J_m'(j\gamma R_a)H_m'(j\gamma R_b)} & \gamma \neq 0 \end{cases}$$

J_m and H_m are the Bessel function of the first and second kind, respectively. The primes indicate their derivatives, which are given by

$$\begin{aligned} J_m'(\gamma R) &= \frac{d}{d(\gamma R)}J_m(\gamma R) = -J_{m+1}(\gamma R) + \frac{m}{\gamma R}J_m(\gamma R) \\ H_m'(\gamma R) &= \frac{d}{d(\gamma R)}H_m(\gamma R) = -H_{m+1}(\gamma R) + \frac{m}{\gamma R}H_m(\gamma R) \end{aligned} \tag{E.15}$$

E.2 Coupling Equations and Boundary Conditions

Any number of these regions described by the above transfer relations can be coupled together to form a complete electromagnetic system. For a problem with N regions, there will be $2N$ transfer relation equations in $4N$ independent variables. To complete the

system, an additional *2N* equations can be obtained from the coupling between the regions and the boundary conditions.

• **Coupling equations** Tangential H and A_z must be continuous at any boundary, in the absence of surface current. For an N region problem, there will be *N-1* boundaries coupling regions, establishing *2N-2* coupling equations.

• **Boundary conditions** There will be two regions on the "ends" of the problem that will either be bounded by a very high permeability material like steel, or whose boundary will go to zero or infinity. In either case the boundary conditions at these surfaces require that tangential H and A_z go to zero. There will be 2 of these boundary conditions which, combined with the coupling equations, provide the *2N* equations necessary to specify the electromagnetic system.

To complete the model, a method for introducing source currents, like the armature current, must be integrated into this framework.

E.3 Effect of Current on Boundary Fields

As Eq. 2.46 indicates, the armature current will consist of travelling wave harmonics, which expressed in the two coordinate systems as

$$J_{an} = \Re\left\{J_n e^{\left(\frac{np}{R}x + n_t\omega_e t\right)}\right\} \qquad J_{an} = \Re\{J_n e^{(np\theta + n_t\omega_e t)}\} \tag{E.16}$$

This current density must be integrated into the transfer relation framework to characterize the eddy current losses. This can by accomplished by modeling the armature as a surface current at a boundary, or as a current-carrying region.

E.3.1 Boundary Surface Current

One approach to the introduction of source current is to place a surface current at a

boundary. Tangential magnetic fields terminate on surface currents, so this will simply modify the coupling equation describing tangential $\boldsymbol{H}$. If there is a surface current K at a boundary, the appropriate coupling equation are

$$\hat{H}_x^a = \hat{H}_x^b + K \qquad \hat{H}_\theta^a = \hat{H}_\theta^b + K \tag{E.17}$$

For a problem where the source current is specified as a current *density* J, a reasonable approximation is

$$K = J\Delta \tag{E.18}$$

where Δ is the width of the current density. Placing the surface current in the middle of the current density region and accordingly increasing the width of the adjoining regions, is a further approximation to the actual effect of the current density.

When modeling the PMSM eddy current losses, this approximation breaks down when there is a thick armature and a small air gap. In that case the current in placed much farther away from the magnets than the edge of the current density. Hence, the surface current approach tends to *underestimate* eddy current losses. To produce more accurate results and allow for more general machine designs, a second, more accurate, model can be used.

E.3.2 Current Density in a Region

The transfer relations derived in Section E.1 assumed that there was no current density in the region. Now we allow for a current density J_z that is a travelling wave and constant across the armature thickness. To introduce this into the region, start with Ampère's Law

$$\nabla \times \boldsymbol{H} = \boldsymbol{J} \tag{E.19}$$

with can be written in terms of the magnetic vector potential as

$$\nabla^2 \boldsymbol{A} = -\mu \boldsymbol{J} \tag{E.20}$$

Because $\boldsymbol{A}$ and $\boldsymbol{J}$ are only z-directed, this can be expressed

$$\nabla^2 A_z = -\mu J_z \tag{E.21}$$

In rectangular and cylindrical coordinates, respectively, this is

$$\frac{\partial^2}{\partial y^2} A_z(y) - \left(\frac{np}{R}\right)^2 A_z(y) = -\mu J_z \tag{E.22}$$

and

$$\frac{1}{r}\frac{\partial}{\partial r}\left(r\frac{\partial}{\partial r}A_z(r)\right) - \left(\frac{np}{r}\right)^2 A_z(r) = -\mu J_z \tag{E.23}$$

Note that these equations resemble Eqs. E.4 and E.5 for a region with no conductivity and a driving term. Hence, the homogeneous solution will be identical, and there will now be a particular solution.

- **Rectangular coordinates** The particular solution to Eq. E.22 is simply the constant

$$A_z^p = \frac{\mu J_z R^2}{(np)^2} \tag{E.24}$$

This expression is independent of y, so H_x, as given by Eq. E.8, will be unchanged. Consequently the expressions given in Eq. E.10 will still be valid, so the transfer relation, Eq. E.11, will simply have the particular solution A_z^p added to it to give the transfer relation for a region with a current density:

$$\begin{bmatrix} \hat{A}_z^1 \\ \hat{A}_z^2 \end{bmatrix} = \frac{\mu}{\alpha} \begin{bmatrix} \coth(\alpha\Delta) & \dfrac{-1}{\sinh(\alpha\Delta)} \\ \dfrac{1}{\sinh(\alpha\Delta)} & -\coth(\alpha\Delta) \end{bmatrix} \begin{bmatrix} \hat{H}_x^1 \\ \hat{H}_x^2 \end{bmatrix} + \begin{bmatrix} \dfrac{\mu J_z}{\alpha^2} \\ \dfrac{\mu J_z}{\alpha^2} \end{bmatrix} \tag{E.25}$$

where

$$\alpha = \frac{np}{R} \tag{E.26}$$

• **Cylindrical coordinates** The solutions to Eq. E.23, unlike those of Eq. E.5, can be obtained in closed form. The solutions to the diffusion equation will, in general, involve Bessel functions embedded in the functions F and G given by Eq. E.14. However, in the specific case of a region with current density, $\gamma = 0$, and F and G reduce to closed form expressions.

The particular solution to Eq. E.23 is

$$A_z^p = \begin{cases} \dfrac{\mu J}{(np)^2 - 4} r^2 & np \neq 2 \\ \dfrac{1}{4}\mu J r^2 \left(\dfrac{1}{4} - \ln r \right) & np = 2 \end{cases} \tag{E.27}$$

The homogeneous solution will satisfy Laplace's equation and can be combined with the particular solution to give

$$A_z = A_z^h + A_z^p = k_+ r^{np} + k_- r^{-np} + A_z^p \tag{E.28}$$

The tangential magnetic field can be found from

$$H_\theta = \frac{1}{\mu}B_\theta = \frac{1}{\mu}(\nabla\times\boldsymbol{A})_\theta = -\frac{1}{\mu}\frac{\partial}{\partial r}A_z$$

$$= -\frac{1}{\mu}[k_+(np)r^{np} - k_-(np)r^{-np}] + \begin{cases} -\dfrac{2J}{(np)^2-4}r & np \neq 2 \\ \dfrac{1}{2}Jr\left(\dfrac{1}{4}+\ln r\right) & np = 2 \end{cases} \tag{E.29}$$

If we set the boundary conditions

$$H_\theta\big|_{r=R_i} = \hat{H}_\theta^i \qquad\qquad H_\theta\big|_{r=R_o} = \hat{H}_\theta^o \tag{E.30}$$

we can solve for k_+ and k_-. These expressions are extremely complex and will not be reproduced here, but they can be substituted into Eq. E.28 to yield, at the boundaries,

$$\begin{aligned} \hat{A}_z^i &= \left[\mu\frac{R_i}{np}\frac{\left(\frac{R_o}{R_i}\right)^{np}+\left(\frac{R_i}{R_o}\right)^{np}}{\left(\frac{R_o}{R_i}\right)^{np}-\left(\frac{R_i}{R_o}\right)^{np}}\right]\hat{H}_\theta^i + \left[\mu\frac{2R_o}{np}\frac{1}{\left(\frac{R_i}{R_o}\right)^{np}-\left(\frac{R_o}{R_i}\right)^{np}}\right]\hat{H}_\theta^o + A_z^{J,\mathrm{i}} \\ \hat{A}_z^o &= \left[\mu\frac{2R_i}{np}\frac{1}{\left(\frac{R_o}{R_i}\right)^{np}-\left(\frac{R_i}{R_o}\right)^{np}}\right]\hat{H}_\theta^i + \left[\mu\frac{R_o}{np}\frac{\left(\frac{R_i}{R_o}\right)^{np}+\left(\frac{R_o}{R_i}\right)^{np}}{\left(\frac{R_i}{R_o}\right)^{np}-\left(\frac{R_o}{R_i}\right)^{np}}\right]\hat{H}_\theta^o + A_z^{J,\mathrm{o}} \end{aligned} \tag{E.31}$$

where $A_z^{J,\mathrm{i}}$ and $A_z^{J,\mathrm{o}}$ capture the effect of the surface current, and are given by

$$A_z^{J,\mathrm{i}} = \begin{cases} \mu J(R_i)^2 \left[\dfrac{1}{np(np+2)} + \dfrac{4}{np[(np)^2-4]} \dfrac{\left(\dfrac{R_o}{R_i}\right)^{np} - \left(\dfrac{R_o}{R_i}\right)^2}{\left(\dfrac{R_o}{R_i}\right)^{np} - \left(\dfrac{R_i}{R_o}\right)^{np}} \right] & np \neq 2 \\ \dfrac{\mu J(R_i)^2}{8} \left[1 + 4 \dfrac{\left(\dfrac{R_o}{R_i}\right)^2 \ln\left(\dfrac{R_o}{R_i}\right)}{\left(\dfrac{R_o}{R_i}\right)^2 - \left(\dfrac{R_i}{R_o}\right)^2} \right] & np = 2 \end{cases} \tag{E.32}$$

and

$$A_z^{J,\mathrm{o}} = \begin{cases} \mu J(R_o)^2 \left[\dfrac{1}{np(np+2)} + \dfrac{4}{np[(np)^2-4]} \dfrac{\left(\dfrac{R_i}{R_o}\right)^{np} - \left(\dfrac{R_i}{R_o}\right)^2}{\left(\dfrac{R_i}{R_o}\right)^{np} - \left(\dfrac{R_o}{R_i}\right)^{np}} \right] & np \neq 2 \\ \dfrac{\mu J(R_o)^2}{8} \left[1 + 4 \dfrac{\left(\dfrac{R_i}{R_o}\right)^2 \ln\left(\dfrac{R_i}{R_o}\right)}{\left(\dfrac{R_i}{R_o}\right)^2 - \left(\dfrac{R_o}{R_i}\right)^2} \right] & np = 2 \end{cases} \tag{E.33}$$

Comparing Eq. E.31 to the definition of F and G in Eq. E.14 allows the transfer relation to be written

$$\begin{bmatrix} \hat{A}_z^i \\ \hat{A}_z^o \end{bmatrix} = \mu \begin{bmatrix} F(R_o, R_i, 0, np) & G(R_i, R_o, 0, np) \\ G(R_o, R_i, 0, np) & F(R_i, R_o, 0, np) \end{bmatrix} \begin{bmatrix} \hat{H}_\theta^i \\ \hat{H}_\theta^o \end{bmatrix} + \begin{bmatrix} A_z^{J,\mathrm{i}} \\ A_z^{J,\mathrm{o}} \end{bmatrix} \tag{E.34}$$

This completes the transfer relation for a current-carrying region in cylindrical coordinates.

E.4 Summary of Models

This appendix has presented 4 models for determining the tangential $\boldsymbol{H}$ and axial $\boldsymbol{B}$ fields at the material boundaries. These approaches can be classified as follows, in order of increasing complexity:

Model	Coordinate System	Armature Model
I	rectangular	surface current
II	rectangular	current-carrying region
III	cylindrical	surface current
IV	cylindrical	current-carrying region

Table E.1: Classification of boundary field models

To test these models, the total eddy current power loss for two sample machines in Chapter 3 is calculated using each of the four models. The results are presented in Table E.2. As expected, the models that use the surface current approximation predict lower losses than the accompanying current-carrying region models, as discussed in Sec. E.3.1. Model IV is used in the design process because it produces accurate results and does not require excessive computation time.

Machine	Model	Model Loss Prediction (W)	FEA Loss Calculation (W)	Error
A	I	15.83	12.87	23.0%
	II	17.60	12.87	36.8%
	III	10.98	12.87	14.7%
	IV	12.98	12.87	0.9%
B	I	4.62	5.00	7.6%
	II	6.48	5.00	29.6%
	III	3.17	5.00	36.6%
	IV	4.94	5.00	1.2%

Table E.2: Accuracy of eddy current loss models

Appendix F

Effect of Machine Length on Rotor Eddy Current Loss

In this appendix, a model that allows for an axial length of the machine when finding eddy current losses is developed. It builds upon the 2D model developed in Appendix E by introducing an attenuation factor k_l that accounts for the reduction in losses due to the finite machine length.

F.1 Construction of Model

Extension to a full three-dimensional analysis of machine fields would require solving the three-dimensional magnetic diffusion equation. Given the complexity of the two-dimensional solution, this approach was considered overly complicated and was avoided. A simpler approach was constructed using a two-dimensional coordinate system.

In this model the rotor is "unrolled," creating the Cartesian coordinate system illustrated in Fig. F.1. The radius R is the average radius of the magnets

$$R = R_{avg} = \frac{R_m + R_s}{2} \tag{F.1}$$

This is an approximation and as demonstrated in Appendix E it will reduce model accuracy, but it simplifies the problem to the degree that it can be solved in closed form. The entire machine is then considered to be a current-carrying sheet in the x-z plane, which can be characterized by a surface impedance $\hat{Z}_s$ given by

$$\hat{Z}_s = \frac{\hat{E}_z}{\hat{H}_x} \tag{F.2}$$

The driving current in this problem is assumed to be a travelling wave surface current

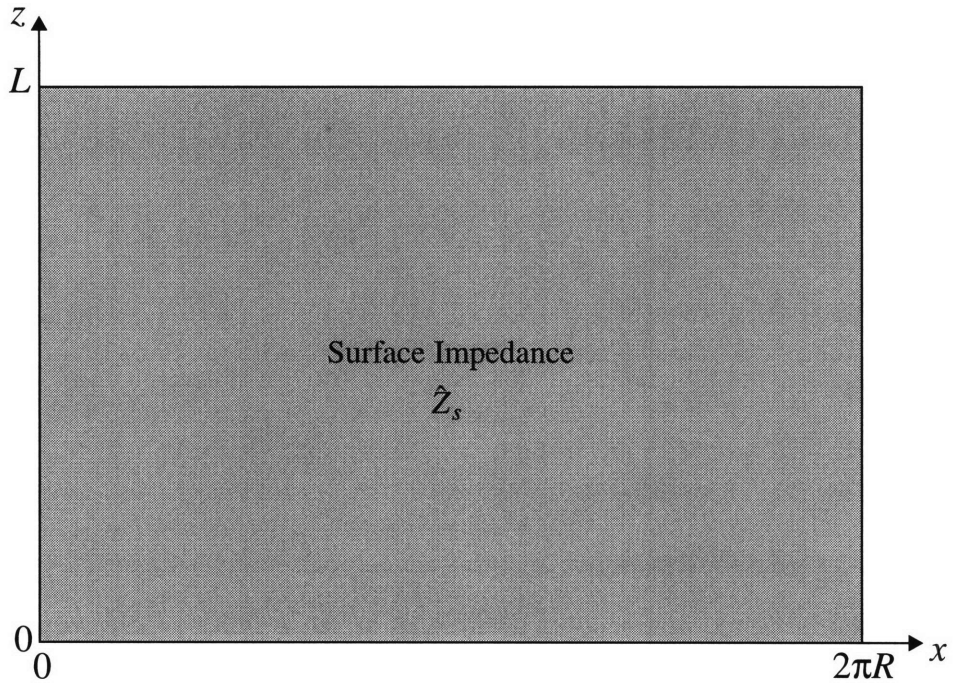

Figure F.1: Axially limited rotor eddy current loss model geometry

adjacent to the sheet, so that

$$\hat{H}_x = \hat{K} \tag{F.3}$$

Note that in the 2D framework the expression for eddy current losses given in Eq. 2.56, the losses will be then given by

$$P_{2D} = \frac{1}{2}\hat{K}^2 \Re\{\hat{Z}_s\} \tag{F.4}$$

F.2 Derivation of Machine Length Coefficient

Now assuming a finite machine length L, we take the radial magnetic flux density to be a constant B_0 over the axial length of the machine ($0 < z < L$), and zero outside of it. It will also be a travelling wave in x, so

$$B_y = \Re\left\{\hat{B}e^{j\left(\frac{np}{R}x - n_t\omega_e t\right)}\right\} \tag{F.5}$$

This ignores effects such as end turn current but again provides a reasonable approximation to machine behavior. This magnetic flux will drive circulating eddy currents in the x-z plane, producing a current distribution

$$\boldsymbol{K} = \hat{K}_x\hat{x} + \hat{K}_z\hat{z} \tag{F.6}$$

Using the fact that $\boldsymbol{K}$ is divergenceless,

$$\nabla \cdot \boldsymbol{K} = 0 \tag{F.7}$$

the surface current can be expressed as the curl of a vector potential

$$\nabla \times \boldsymbol{A} = \boldsymbol{K} \tag{F.8}$$

Now applying Faraday's Law,

$$\nabla \times \boldsymbol{E} = \hat{Z}_s \nabla \times \boldsymbol{K} = -\frac{\partial \boldsymbol{B}}{\partial t} \tag{F.9}$$

with Eqs. F.5 and F.8 gives

$$\nabla^2 A_y = \frac{jn_t\omega_e}{Z_s}B_y \tag{F.10}$$

A_y will also be a travelling wave, so this equation can be written

$$\frac{\partial^2}{\partial z^2}\hat{A}_y - \left(\frac{np}{R}\right)^2 \hat{A}_y = \frac{jn_t\omega_e}{Z_s}B_y \tag{F.11}$$

Because the radial flux density is discontinuous, $\hat{A}_y$ will take the form of a Fourier series

$$\hat{A}_y = \sum_m A_m \sin(\alpha_m z) \tag{F.12}$$

The vector potential must vanish at the ends of the machine ($z = 0$ and $z = L$), establishing

$$\alpha_m = \frac{m\pi}{L} \tag{F.13}$$

Now B_y can be decomposed into a Fourier series with terms given by

$$\hat{B}_y = \sum_{\text{m odd}} \frac{4}{m\pi} B_0 \sin(\alpha_m z) \tag{F.14}$$

Eq. F.11 can now be used to find

$$A_m = \begin{cases} -\dfrac{4B_0 j n_t \omega_e}{\hat{Z}_s m\pi \left[\left(\dfrac{np}{R}\right)^2 + (\alpha_m)^2\right]} & m \text{ odd} \\ 0 & m \text{ even} \end{cases} \tag{F.15}$$

This expression can be simplified by using Faraday's Law

$$\hat{E}_z = j n_t \omega_e \hat{A}_z \tag{F.16}$$

where A_z is the *magnetic* vector potential, along with the definition of magnetic vector potential

$$\hat{A}_z = -\frac{jR}{np}\hat{B}_y = -\frac{jR}{np}B_0 \tag{F.17}$$

and the definition of surface impedance to find

$$\frac{B_0}{\hat{Z}_s} = \frac{np\hat{K}}{Rn_t\omega_e} \tag{F.18}$$

The resulting surface current is then found from Eq. F.8. The instantaneous eddy current loss will be the integral of the surface currents over x and z, which is

$$P_{3D}^{i} = \Re\{\hat{Z}_s\}\int_0^L\int_0^{2\pi R}[\Re\{\hat{K}_x\}^2 + \Re\{\hat{K}_z\}^2]dxdz \tag{F.19}$$

This can be time-averaged to give

$$P_{3D} = \Re\{\hat{Z}_s\}\frac{1}{2}2\pi R\int_0^L[\left|\hat{K}_x\right|^2 + \left|\hat{K}_z\right|^2]dz \tag{F.20}$$

The current magnitudes are given by

$$\left|\hat{K}_x\right| = \sum_{\text{m odd}} \alpha_m \frac{4}{m\pi} \frac{\frac{np}{R}\hat{K}}{\left(\frac{np}{R}\right)^2 + (\alpha_m)^2} \cos(\alpha_m z) \tag{F.21}$$

and

$$\left|\hat{K}_z\right| = \sum_{\text{m odd}} \frac{np}{R}\frac{4}{m\pi} \frac{\frac{np}{R}\hat{K}}{\left(\frac{np}{R}\right)^2 + (\alpha_m)^2} \sin(\alpha_m z) \tag{F.22}$$

The integral in Eq. F.20 can now be carried out to give

$$P_{3D} = \frac{4}{\pi^2}\left(\frac{np}{R}\right)^2 \hat{K}^2 \Re\{\hat{Z}_s\} \sum_{\text{m odd}} \frac{1}{m^2} \frac{1}{\left(\frac{np}{R}\right)^2 + (\alpha_m)^2} \tag{F.23}$$

If we now define the machine length coefficient k_l to be

$$k_l = \frac{8}{\pi^2}\left(\frac{np}{R}\right)^2 \sum_{\text{m odd}} \frac{1}{m^2} \frac{1}{\left(\frac{np}{R}\right)^2 + (\alpha_m)^2} \tag{F.24}$$

the power loss can be written

$$P_{3D} = \frac{1}{2}\hat{K}^2 \Re\{\hat{Z}_s\} k_l \tag{F.25}$$

Comparing this to Eq. F.4 it is evident that

$$P_{3D} = k_l P_{2D} \tag{F.26}$$

so that the coefficient k_l serves as a 3D correction factor for power losses computed with 2D methods. It can be shown that

$$\lim_{L \to \infty} k_l = 1 \tag{F.27}$$

and

$$\lim_{L \to 0} k_l = 0 \tag{F.28}$$

which satisfies the requirement that the 2D and 3D models are equivalent for very long machines, and that the losses go to zero as the machine becomes very short.

This 3D eddy current loss model is by no means the most accurate model that could be developed. Certainly it can be extended to cylindrical coordinates and the effect of machine length on the surface impedance investigated. But it provides a good starting point for the effect of short machines and will be integrated into the machine design.

References

[1] R.F. Post, T.K. Fowler, and S.F. Post, "A High-Efficiency Electromechanical Battery," *Proceedings of the IEEE*, March 1993, pp. 462-474.

[2] SatCon Technology Corporation, Cambridge, Mass.

[3] U. Shaible and B. Szabados, "A Torque Controlled High Speed Flywheel Energy Storage System for Peak Power Transfer in Electric Vehicles," *Proceedings of the 1994 IEEE Industry Applications Society Annual Meeting*, pp. 435-442.

[4] C. Lashley, et. al., "Development of a High-Efficiency Motor/Generator for Flywheel Energy Storage," *Proceedings of the 26th Intersociety Energy Conversion Engineering Conference*, 1991, pp. 221-226.

[5] A.E. Fitzgerald, C. Kingsley, and S.D. Umans, *Electric Machinery*, 5th ed., McGraw-Hill, 1990.

[6] K.J. Binns, F.B. Chaaban, "The Relative Merits of Rare-Earth Permanent Magnet Materials for Use in the Excitation of Permanent Magnet Machines," *ICEM*, 1988, pp. 65-70.

[7] K. Srinivasan, "Integrated Design of High-Speed Permanent Magnet Synchronous Motor Drives," Ph.D Thesis, Massachusetts Institute of Technology, 1995.

[8] J.S. Arora, *Introduction to Optimum Design*, McGraw Hill, New York, 1989.

[9] J.A. Moses, J.L. Kirtley, J.H. Lang, et. al., "A Computer-Based Design Assistant for Induction Motors," *IEEE Industry Applications Society Conference*, 1991, Dearborn, Mich, pp. 1-7.

[10] J.L. Kirtley, "Design and Construction of an Armature for an Alternator with a Superconducting Field Winding," Ph.D Thesis, Massachusetts Institute of Technology, 1971.

[11] U. Sinha, "A Design Assistant for Induction Motors," M.S. Thesis, Massachusetts Institute of Technology, 1993.

[12] D.E. Cameron, J.H. Lang, "The Computer-Aided Design of Variable Reluctance Generators," *Proceedings: APEC '92*.

[13] NeFeB magnet data sheets, Unimag, Inc., Valparaiso, Ind.

[14] K. Halbach, "Design of Permanent Multipole Magnets with Oriented Rare Earth Cobalt Material," *Nuclear Instruments and Methods*, Vol. 169, 1980, pp. 1-10.

[15] J. Ofori-Tenkorang and J.H. Lang, "A Comparative Analysis of Torque Production in Halbach and Conventional Surface-Mounted Permanent-Magnet Synchronous Motors," Draft, M.I.T. Electrical Engineering Dept.

[16] J.R. Melcher, *Continuum Electromechanics*, 1980.

[17] *Maxwell 2D Field Simulator,* Ansoft Corporation, Pittsburgh, Penn.

[18] *Maple V,* University of Waterloo, Canada

[19] *Matlab 4.2*, The Mathworks Inc.

[20] *Maxwell 3D Field Simulator*, Ansoft Corporation, Pittsburgh, Penn.

6111-32